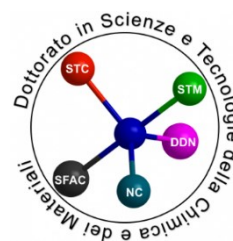**Università degli Studi di Genova**

Doctorate in

Sciences and Technologies of

Chemistry and Materials

XXXV Cycle

Curriculum: Chemical Sciences and Technologies

New Polymer and Composite Structures for Photonic Applications

HEBA MEGAHD

(HEBA ABDELSALAM ABDELWAHAB ABDELSALAM MEGAHD)

Supervisor: Prof. Davide Comoretto

Referees: Prof. Michael Debije, University of Eindhoven

Prof. Jiri Pfleger, The Czech Academy of Sciences

Abstract: All-polymer Photonic Nanostructures: From sensing to Fluorescence Control

The focus of this thesis is the development of materials and architectures for all-polymer functional structures for photonic applications. The first part concerns the improvement and optimization of colorimetric and fluorescent sensing structures for the detection of various analytes in the vapor phase. Optical-readout sensors are portable and can provide an easy interpretation that needs no specialized training and can be visible to the naked eye. This makes them promising for applications in environmental control, health monitoring and food safety. The objective of the work was to investigate analyte diffusion processes into multilayered structures of polymer submicrometric films, and then optimizing the structure design and expanding the materials used in the field. First, sensors based on vapor diffusion in multilayered polymer dielectric mirrors with structural coloring were developed. Given their clear color change, this typology of sensors has been shown to be promising in the literature. However, as their response is limited by the diffusion speed of molecular species, they can suffer from slow detection of vapor-phase analytes. Next, I examine the use of fluorescent polymer films sensitive to microviscosity changes caused by exposure to volatile organic compounds and observing the changes in fluorescence during said exposure. The effect on the overall diffusion of capping layers deposited on top of the fluorescent polymer was investigated to quantify the effect of the barrier polymer on the selectivity of the sensor. Finally, I employed the solution processing protocols developed for novel low refractive index polymer suspensions that were initially utilized for the sensors to engineer structures for fluorescence control.

When two highly reflecting structures encapsulate a luminescent material in a submicrometric space, this changes the photoluminescence properties in structures called optical microcavities. While the highly reflecting structures can be metallic mirrors, these have limited reflectance intensity, high absorbance losses, as well as a lack of tunability. Instead, the use of dielectric mirrors enables very high reflectance at desired wavelengths. In addition, the use of compliant polymer materials allows the future use of these structures to construct more efficient flexible devices. I was able to develop highly reflecting microcavities for emitters in the visible range as well as in the near infrared. Besides achieving high amplification of fluorescence intensity, I was also able to report for the first time a change in the radiative rate of the fluorescence for

polymer structures. As these effects were so far only observed in planar structures of inorganic nature or more complex polymer three-dimensional systems, this presents a breakthrough in the field.

In this introduction I will give a wide but deep overview of the optics of multilayered polymer films, their diffusion peculiarities, and use for sensing. Furthermore, I will address the topic of solid-state organic fluorophores and controlling their photoluminescence through engineering the dielectric environment. This will be followed by a chapter-by-chapter exploration of the results obtained during the doctoral training as adapted from already published or drafted work. Finally, the outlook and possible future implications and developments of this research will be examined.

Acknowledgments

Looking back at the three years preceding this thesis, I am grateful for all the people who made it possible. First and foremost, to my supervisor Prof. Davide Comoretto, thank you for your endless support and constant education. Thank you for believing in me, for pushing me, for teaching me how to be a critical scientist, but also a fun one. Every conversation we had was a source of insight about science, life, culture and of course candy. With a journey ranging from covid hotels to riding bikes, I am gratefully lucky to have you as my mentor.

To Prof. Paola Lova, you have been a grounding force since my master's and during my PhD journey, sharing all your knowledge, tips about instruments, science, time management, growth, and the ins and outs of the academic world among others. Thank you for everything.

I would also like to thank Prof. Michael Debije and Prof. Jiri Pfleger for their valuable input about this work.

I like to express my appreciation to several collaborators who played a key role in this project:

- Prof. Andrea Pucci from the Department of Chemistry and Industrial Chemistry of the University of Pisa for the aggregation induced emission copolymers.
- Prof. Maddalena Patrini of the University of Pavia for her experimental support.
- Prof. Cosimo D'Andrea and Dr. Samim Sardar from the Center for Nano Science and Technology at the Politecnico di Milano for their aid in measurements of fluorescence lifetime.
- Prof. Daniel T. Gryko and Dr. Beata Koszarna from the Institute of Organic Chemistry of the Polish Academy of Sciences for providing the Diketopyrrolopyrrole dye.
- Prof. Josef Breu and Volodymyr Dudko for providing new and exciting fluorescent materials.
- Prof. Davide Peddis and Dr. Sawssen Slimani for providing fantastic magnetic nanoparticles.
- Prof. Albert Schenning, Dr. Yari Foelen and Prof. Dick Broer. Thank you and the entire SFD team for your guidance, teaching and welcoming. I have learned a lot from the time spent in Eindhoven and will look back on it fondly. To all the SFD crew, especially Tom and Marjolijn, thank you for making Helix so friendly. Wishing you all the best.
- Dr. Omar Soda for the SEM measurements.

List of Abbreviations

AQ	Aquivion®
AFM	Atomic force microscope
AIE	Aggregation-induced emission
arb. u.	Arbitrary unit
BL	Bilayer
CA	Cellulose acetate
conc.	Concentration
CP	Copolymer
D_{eff}	Effective diffusion coefficient
DBR	Distributed Bragg reflector
DCM	Dichloromethane
DPP	Diketopyrrolopyrrole
EtOH	Ethanol
FHPS	Flory-Huggins photonic sensor
FMR	Fluorescent molecular rotors
FWHM	Full width at half maximum
HBS	Hyperbranched polyvinyl sulfide
HFB	Hexafluorobenzene
HOMO	Highest occupied molecular orbital
IPA	Isopropyl alcohol
IR	Infrared
IRF	Intrinsic response function
IVP	Inverse vulcanized polymer
JCBF	2-[4-vinyl(1,1$0$-biphenyl)-4$0$-yl]-cyanovinyljulolidine
LED	Light-emitting diode

LPDOS	Local photonic density of states
LUMO	Lowest unoccupied molecular orbital
M	Polymer mass intake
MC	Microcavity
NIR	Near infrared
NR	Non-radiative
OSC	Optical sorption curve
PAA	Poly(acrylic acid)
PBG	Photonic band gap
PhC	Photonic crystals
PL	Photoluminsescne
PMF	Polymer multilayered films
PS	Polystyrene
PVA	Poly(vinyl alcohol)
PVK	Poly(N-vinylcarbazole)
rad	Radiative
rps	Revolutions per second
SEM	Scanning electron microscope
SOL	Solution
t	time
TMM	Transfer matrix method
TRPL	Time-resolved photoluminescence lifetime
UV	Ultraviolet
VIS	Visible

Table of Contents

Chapter 1: Introduction

The use of polymer multilayered films (PMFs) is currently an essential part of everyday life,[1] from packaging[2] and separation membranes[3] to organic LEDs.[4] Since the first reports of layer-by-layer assembly for polymer films,[5] multiple industrial breakthroughs have allowed the technology to mature.[1] Functional composites for barrier applications, including packaging, usually have a thickness in the micrometer range.[6] However, for applications in optics individual layer optical thicknesses (the product of geometric thickness and the refractive index) need to be comparable to the wavelength of visible light in order to interact strongly with it.[7] By stacking optically thin films in an ordered manner, it is possible to construct photonic multilayers called dielectric mirrors, one-dimensional photonic crystals or distributed Bragg Reflectors (DBRs). Fig. 1.1a shows a scanning electron microscope (SEM) scan of the fully solution-processed polymer DBR made of the transparent perfluorinated polymer Aquivion®, and Poly(N-vinylcarbazole) (PVK) clarifying the scale of individual films forming the pictured green-reflecting structure (bottom-left). This structural color is cause by the constructive interference between reflected and refracted rays at each interface, giving rise to wavelengths that are strongly reflected. These structures are ubiquitous in nature and generate the opalescent color of mother-of-pearl and the intense blue of the morpho genus butterflies as seen in Fig. 1.1b and c.[8-10] In these cases, the alternating layers of chitin and air for the butterfly or calcium carbonate and soft biopolymers in nacre form a dielectric mirror. The responsiveness of such photonic structures and their unique optical characteristics lends them to applications in fields ranging from sensing to light emitting devices.

While inorganic multilayer thin film deposition and growth technologies have reached industrial scales earlier in the 20th century due to the boom in the semiconductor industry,[11] large scale production of polymer ones has fallen behind. As inorganic materials have a wide variety in refractive indices as well as high mechanical stability, they were at the forefront of optical materials development. However, in the past decades, the development of thin film fabrication technologies compatible with polymers, from Blodgett-Langmuir deposition to spin coating and dip coating has ushered wide research interest in thin PMFs on the laboratory scale.[12] Essentially, the mechanical flexibility, wide functionalities, solution processability and low-cost fabrication of polymers give them unmatched performance in a diverse range of applications. Ultimately, the invention of coextrusion technology and its application for

polymer DBRs has catapulted the fabrication of PMFs from the lab scale to industrial ones,[13, 14] where today it is possible to cover the exterior of entire buildings with dielectric polymer mirrors. This can be seen, for example, on the *La Defense* building in Almere, in the Netherlands as pictured in Fig. 1.1d, covered by plastic DBRs of polyester and acrylic as manufactured by 3M™.[15]
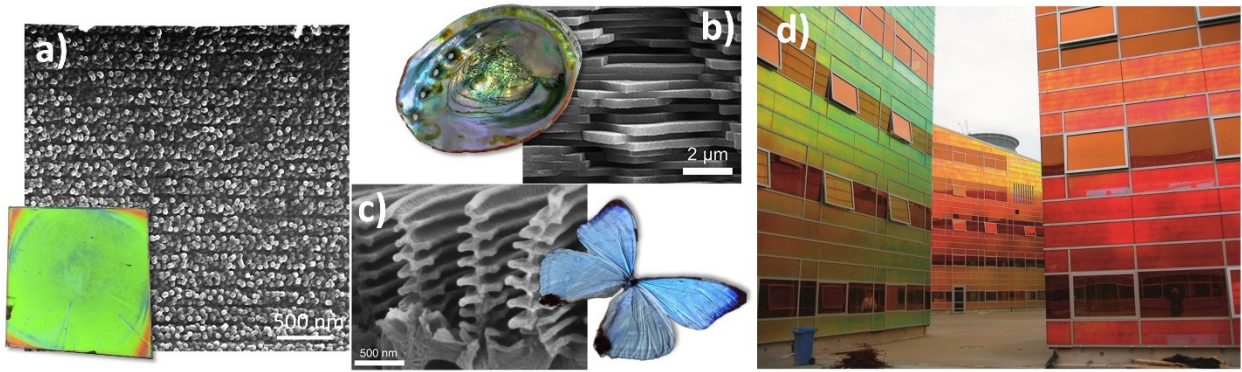
Figure 1.1. a) SEM scan of an all-polymer DBR (pictured bottom-left), b) SEM scan of *Mollusk* shell (pictured, top left) [adapted from 8, 9], c) SEM scan of *Morpho sulkowskyi* scales (pictured, bottom right) [adapted from 10], d) building covered with 3M™ dichroic film.[15]

To understand the phenomena giving rise to the interesting optical effects in photonic multilayered films, it is necessary to examine thin film interference.

Thin Film Interference and Dielectric Mirrors

For an optically thin film on a substrate, light incident on a material at angle θ partially refracts and reflects at the planar interfaces due to the refractive index change between the media, as described by Snell's law and Fresnel equations.[7] When the difference in the optical paths between the beams reflected from the top and from the bottom interfaces equals a multiple of the incident wavelength, then they undergo constructive interference. So, for a film of a specific thickness and refractive index there would be several frequencies that are reflected and unable to transmit through, forming an interference pattern. In the case of multilayered films formed of two alternating materials of high (n_H) and low (n_L) refractive indices of thicknesses d_H and d_L respectively, this effect occurs at each interface as shown in Figure 1.2. Each pair of low and high refractive index layers will henceforth be referred to as a bilayer (BL) with a combined thickness of D.
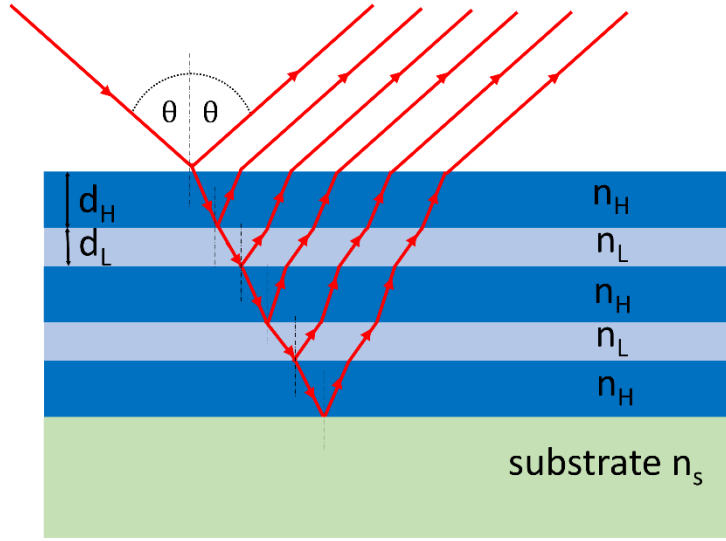
Figure 1.2. Schematization of thin film reflection, refraction and interference for a multilayered thin film structure on a substrate (transmission through the substrate is not reported).

On increasing the number of layers, an intense reflectance peak arises due to the constructive interference of the reflected rays, known as a photonic bandgap (PBG), in analogy to the optical bandgap in crystalline semiconductors, with low-intensity interference fringes in the background. As the number of layers increases, the width and intensity of the PBG approach the values expected for an infinite DBR. The spectral position of these PBGs (λ_{PBG}) can be roughly described by the Bragg-Snell equation (Equation 1.1), with n_{eff} being the effective refractive index (Equation 1.2, i.e. the volume average of refractive index of components[16]) and m being the PBG order, similar to the diffraction orders in crystals.[17]

$$m\lambda_{PBG} = 2D\sqrt{n_{eff}^2 - sin^2(\theta)} \qquad (1.1)$$

$$n_{eff} = \sqrt{\frac{d_H}{d_H + d_L}(n_H)^2 + \frac{d_L}{d_H + d_L}(n_L)^2} \qquad (1.2)$$

The increase of the reflection intensity can be described by Equation 1.3, showing that the reflectance is directly proportional to the dielectric contrast between the DBR components (n_L/n_H) raised to the power of N in the DBR.[18] While Equation 1.3 is a simplification only valid in the case quarter-wave stacks, where the optical length in both materials are equal ($d_H n_H = d_L n_L$), the increase of reflectance with the number of layers generally applies. Therefore, it is

possible to achieve very high reflectance with materials of high index contrast using a relatively low number of bilayers, or vice versa.

$$R_{max} = \left[\frac{1 - n_S \left(\frac{n_L}{n_H} \right)^{2N}}{1 + n_S \left(\frac{n_L}{n_H} \right)^{2N}} \right]^2 \qquad (1.3)$$

Besides affecting the intensity, the bandwidth of the PBG is also controlled by the difference in the refractive index. Equation 1.4 describes the relationship between the bandwidth of the PBG (ΔE_{PBG}), the position of the PBG (E_{PBG}) in energy, and the refractive index contrast between the materials forming the endless DBR also in the quarter-wave condition. [19]

$$\Delta E_{PBG} = \frac{4E_{PBG}}{\pi} \frac{\Delta n}{2n_L + \Delta n} \qquad (1.4)$$

To understand the characteristics of DBRs not in the quarter-wave stack, it is necessary to use a model tailored for the structure. For homogenous and isotropic media extending infinitely in the X and Y directions but with finite thicknesses (in the Z direction), it is possible to construct a matrix describing the transmission and reflectance at each interface of incident monochromatic light that is either p or s polarized. The Transfer Matrix Method (TMM) uses matrices describing the propagation of the electromagnetic fields across a layer and across interfaces. Due to the continuity conditions for the propagation of electromagnetic waves, it is possible to relate the complex amplitudes of the electric field phasor for the reflected and transmitted plane waves through the structure.[20] Using information about the refractive index and thickness of each layer, it is simple to solve the matrix for the electric field values, and then retrieve the reflectance or transmittance coefficients using appropriate algorithms. [19]

Using the TMM, the reflectance of a structure formed of alternating layers of the commodity polymers polystyrene (PS) and cellulose acetate (CA) was calculated as an example.[21] Fig 1.3.a shows the reflectance spectra of PS/CA BLs of increasing number of bilayers (N) with each layer 98 nm thick. For consistency, we only considered unpolarized light hitting the sample at normal incidence as is the case in the experimental setups used substantially in this thesis. For just 2 BLs, a low intensity reflectance peak arises around 600 nm due to constructive interference, which increases to form the highly reflecting PBG as N increases.

Notice that the larger width achieved for a small number of BLs is not intrinsic (with related effects, vide supra) but due to the finite size of the system.
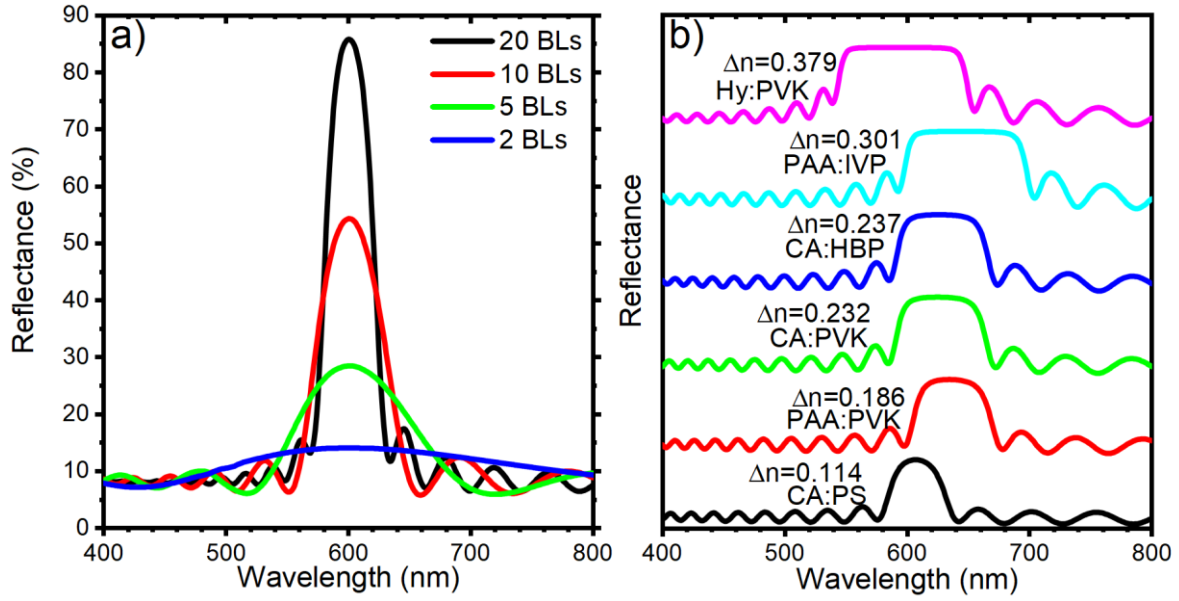
Figure 1.3. Simulation of the optical response for a) stacks of a different number of PS:CA bilayers, and b) reflection of DBRs with 15.5 BLs using polymer pairs of different Δn [adapted from 22].

To visualize the effect of the dielectric contrast on the width of the PBG, Figure 1.3b shows the reflectance spectra calculated for DBRs made of 15.5 BLs of low and high refractive index media with thicknesses d_L=120 nm and d_H=80 nm employing the refractive index of the following couples PS:CA[23], Poly(acrylic acid) (PAA):PVK[24,25], CA:PVK[26], CA: hyperbranched polyvinyl sulfide (HBS),[27] PAA: inverse vulcanized polymer (IVP)[28] and the fluorinated polymer Hyflon with PVK.[29] Regardless of intensity, all the reflectance spectra are characterized by an intense peak positioned in the spectral range between 500 and 700 nm, assigned to the first order PBG of the structure. The backgrounds display instead a Fabry–Pérot interference pattern due to interference from the top and bottom surfaces of the polymer DBR. The spectral width of the stopbands increases with the dielectric contrast, from the bottom spectrum to the top one, as expected from Equation 1.4.

The materials selected for these simulations fulfill a critical condition, which is solubility in orthogonal solvents. In the case of solution-processed photonic structures fabricated through repeated solution coating methods, this allows the stacking of the layers without destroying the structures, which limits the possible materials pairs.[22] Expanding the range of materials used and optimizing the design of DBR structures has attracted extended research interests in the last decade[30] and is an important objective of the presented work.

Polymer Films for Optical-Readout Chemical Vapor Sensors

As the reflectance of DBRs depends strongly on their thickness and refractive index (see Equation 1.1), change in these parameters can lead to observable color change (due to the PBG's spectral shift) that can be used in sensing.[31-33] More generally, continuous transparent polymer films that give an optically distinguishable change on exposure to the chemical vapors are a topic of rising research activity.[34, 35] This is due to their portability, use in the solid state, easy fabrication, and analogue operation without the need for external power supply.

Figure 1.4 shows possible mechanisms relating to the observable optical signal modulation, which can be related to the change in intensity or wavelength of a) absorption, b) fluorescence, or c) reflectance. Two signal changes commonly give the indication of the interaction of the thin film sensor with a target chemical: i) a shift of the maxima at which the optical signal of choice occurs, which is readily observable as a color change, or ii) a decrease in the intensity of the signal which is observed as a color loss. For sensors based solely on the change in the absorption or fluorescence, solvatochromic or chemochromic dyes are blended/immobilized in a polymer matrix or attached to the polymer chains to act as an indicator.[36-41] The preparation of the blend plays an important role in the behavior of the dye.[42] Upon exposure to the target vapors, spectrophotometric measurements of absorption, fluorescence or sometimes solely naked eye observation of the film signal the detection of the analyte. The specificity and selectivity of this typology of sensor depending on molecular dyes can be poor, as multiple analytes with the target functional groups can interact with the solvent, and there can be overlaps in the response signal.[43]

A specific issue regarding fluorescent sensors is quenching phenomena in the solid state,[44, 45] that can affect the films and decrease their quantum yield and the observable fluorescence. However, utilizing fluorophores based on aggregation-induced emission (AIE) bypasses this problem, and even uses it as an asset. These dyes actually increase in fluorescence when their concentration is high or in the solid state.[46] This is due to their specific molecular shapes, as aggregation in the case of AIE restricts fluorophore intramolecular motion, inducing luminescence from aggregates and in the solid state as the preferred relaxation pathway.[47] Thin films demonstrating AIE have been shown to be effective on/off sensors for different chemical vapors.[48]

Finally, photonic crystal based sensors rely on the change in the reflected light upon their interaction with chemical vapors. This circumvents the problem of stability (bleaching) and longevity for some dye-based sensors. As mentioned earlier in the introduction, the wavelength of the photonic bandgap in photonic structures depends on the refractive index and lattice constant of the structure. Hence, their modulation leads to a distinguishable color change that can be exploited for sensing. Photonic polymer films including DBRs,[49] block copolymers,[50, 51] and cholesteric liquid crystals,[52, 53] have been reported to be sensitive to different analytes based on the swelling of the constituting polymers. On the other hand, loss in photonic order or film uniformity can also lead to an observable loss of color that communicates the presence of the target analyte.[54] It is important to note that the angular dependence of the color of commonly observed for photonic crystals dictates a certain angle of observation to insure comparability.[19]
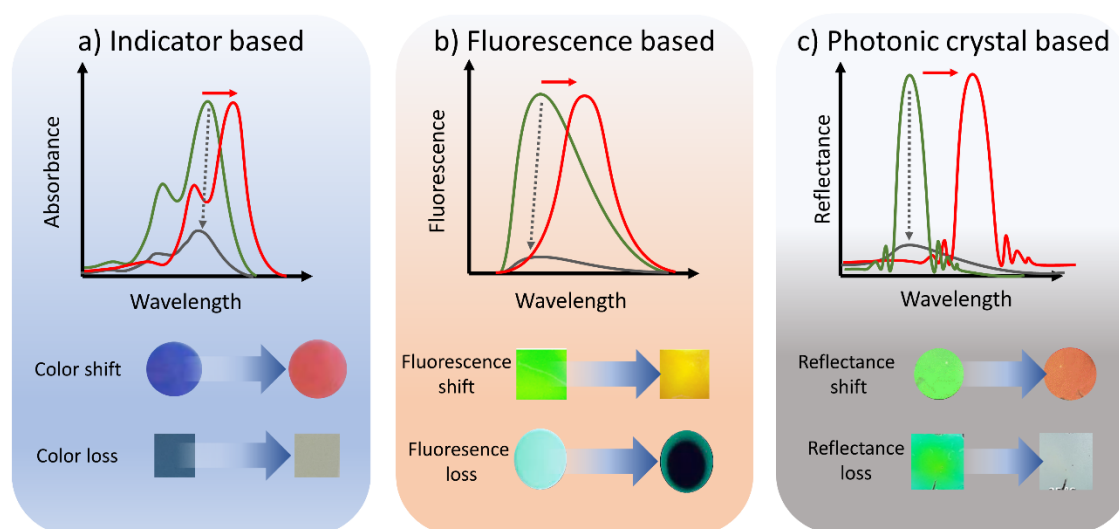
Figure 1.4. Optical read-out sensors mechanism including a) Indicator-based change in absorbance (based on color shift, [55] or loss[43]), b) Fluorescence (wavelength shift, [56] or loss[57]) and c) reflectance change (reflectance shift[58] or loss[54]).

In order to properly design polymer thin films as optically observable sensors, it is essential to understand the different physical phenomena ruling their response. First, it should be noted that the sensing response in these polymer film sensors is ruled by the diffusion of the analyte within the structure, which limits the response time. Vapor diffusion and polymer permeability are complex phenomena that relate to the chemical structure as well as the physical nature of the polymer chains.[59] For faster and stronger response, the analyte should have a strong interaction

with the polymer matrix. This interaction can be quantified by the Flory-Huggins enthalpic parameters (χ), related to the analyte molar volume (V^M) and the solubility as defined by the difference in as the Hildebrand parameters of the polymer and the solvent $\Delta\delta^2 = (\delta_P - \delta_A)^2$ in Equation 1.5.[60]

$$\chi = V^M \frac{\Delta\delta^2}{RT} \tag{1.5}$$

Importantly, stronger interactions between the polymer and analytes can lead to faster swelling of the polymer. As the films are bound to the substrate, the swelling happens only in the direction perpendicular it.[61] This interaction is then the basis of selectivity in most polymer DBRs as sensors.[62] The combined effect of dye sensitivity and polymer-solvent interactions was used to design sensors with more specific response using polymer layers as diffusion barriers. In this case, polymer capping layers prevent selected competitive analytes from reaching the active sensing media,[43] and were reportedly utilized to take advantage of the diffusion kinetics as a selectivity mechanism.[63]

These concepts apply to any polymer film, regardless of its thickness. However, some peculiar effects arise when the film thicknesses go down to the nanometric scale, as the surface to volume ratio increases. For example, the confinement of the polymers in thin films can induce a diffusion enhancement,[64] and in the case of multilayered structures there can be also an acceleration of diffusion at the interfaces due to retention effects.[65]

In conclusion, polymer-analyte interactions, polymer thickness and capping layers are important factors in the design of PMF-based vapor sensors, and indeed must be investigated more thoroughly.

Fluorescence Control in Microcavities

Engineering fluorescence kinetics and quantum yields is usually performed in organic chemistry through molecular design. The radiative rate of fluorescence can depend on the emitter's chemical environment, for example solvent polarity, which is utilized for sensing. [66] A very interesting approach to influence the radiative properties of fluorophores without changing their structure is engineering their dielectric environment through optical microcavities. Such systems play a major role in quantum electrodynamics and are integral for lasers, the development of more efficient LEDs (radiative rate increase) or photovoltaic cells (radiative rate decrease).[67]

Microcavities, also known as microresonators, are sub-micrometric structures capable of confining light in small volumes for a relatively long time. The intrinsic natural resonance modes of the structures can radically modify the local photonic density of states (LPDOS). Again, in analogy to electrons in a crystal, this describes the number of photonic states available to the system per unit of energy, which depends on the structure itself. Thus, it can be designed by manipulating the structure's constituting materials, dimensions, and geometry.[68, 69] As such, when coupled with opportune luminophores or light sources, microcavities have proven themselves valuable in a wide range of optical applications including filters,[70] enhancing device efficiency,[71] lasing,[72] all-optical switching,[73, 74] optical detection,[75] and chemical sensing down to single nanoparticles.[76] In their simplest arrangement, planar microcavities consist of two reflective mirrors sandwiching the cavity layer containing a fluorescent material.

The mirrors can be metallic, dielectric or both, to form hybrid and plasmonic Fabry–Peròt cavities.[77-79] When metallic mirrors are employed, the relatively low reflectance and high absorbance of metals introduce losses limiting their performance and use.[80] Instead, employing one-dimensional planar dielectric DBRs provides ease of fabrication, high tunability, and lower losses, which made them extensively researched.[18, 81] Figure 1.5a shows a schematic of a planar microcavity based on DBRs forming the two mirrors sandwiching the active material and possible spacers to control its position. In these structures, a standing electromagnetic wave is formed due to the interference of travelling waves, leading to an enhanced intensity at the cavity wavelength, which is confined within the defect layer as schematized on the right. The typical reflectance spectra at normal incidence of a DBR is compared to that of a planar microcavity in Fig. 1.5b. Compared to the flat reflectance of the DBR (black), that of the microcavity (red) includes at least one microcavity mode (at λ_C, the microcavity resonance wavelength) where light can propagate within the spectral domain of the PBG, manifesting as a decrease in the reflectance.[82] As a consequence, when the cavity is doped with a fluorophore, its emission can then be enhanced at the antinodes (maxima) or suppressed at the nodes (minima) of the standing wave. Hence, the geometrical placement superimposition between antinodes and emitter in the microcavity is essential to result in emission enhancement, and spacers are often used to control the position of the active material in reference to the electric field in the cavity.[80, 83] To exploit these effects, the emission spectrum of the fluorophore must match the energy of the cavity mode. Consequently, the structure can be engineered to give rise to a high-transmission cavity mode that spectrally matches the fluorescence of a fluorophore embedded inside the cavity

layer.[69, 84, 85] If the emission of the fluorophore instead is at the PBG, it is expected to be suppressed.
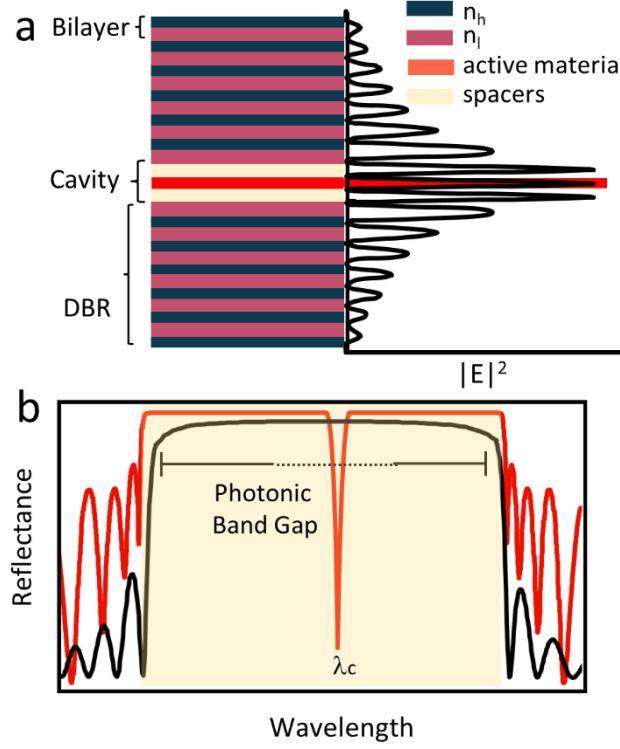
Figure 1.5. a) Schematic representation of planar microcavity and standing electromagnetic wave inside the cavity at λ_C. b) Typical reflectance spectrum of a DBR (black) and a planar microcavity (red).

The spatial and temporal confinement of the electric field within the resonator are quantified by i) the mode volume (V_{eff}), which describes the effective volume where light is confined, related to the peak intensity of the electric field within the cavity (i.e., spatial confinement) and ii) the quality factor (Q), which relates to the rate of power loss inside the cavity, or the lifetime of photons in the cavity (i.e., temporal confinement).[86]

Importantly, the coupling between light and matter in the microcavity can affect the rate of spontaneous emission from the cavity (Γ_c), which is the inverse of the radiative lifetime, in what is termed the Purcell effect. The Purcell factor (P) dictates the coupling strength, and consequently the extent of modification of radiative rate in cavity (Γ_c) for spontaneous emission with respect to emission in free space (Γ_0), depending on the cavity wavelength (λ_C), the refractive index of the cavity layer (n_c), and fundamentally on the ratio Q/V_{eff} (Equation 1.6).

$$P = \frac{\Gamma_c}{\Gamma_0} = \frac{\tau_0^{rad}}{\tau_c^{rad}} = \frac{3}{4\pi^2} \frac{\lambda_c^3}{n_c^3} \frac{Q}{V_{eff}} \qquad (1.6)$$

For a luminescent material of fluorescence with a linewidth smaller than the cavity mode $\Delta\lambda_C$, the emitter can be considered to couple to the cavity mode, altering the lifetime ($\tau = \frac{1}{\Gamma}$) as inferred from Fermi's golden rule.[87] Actually, that rule states that radiative rate is directly proportional to the LPDOS, which as was mentioned earlier, can be manipulated for a photonic structure. It should be noted that other factors influence the radiative rate, including the positioning (r) of the emitter with respect to the antinodes of the cavity standing wave ($\frac{|E(r)|^2}{|E_{max}|^2}$) and the spectral mismatch between the cavity mode and the emission wavelength.[69]

High Purcell factors reflect a higher probability of amplified and spontaneous emission, which are essential for applications like low-threshold lasing[88] and low consumption light-emitting devices.[89] It is also widely exploited to enhance light-matter interaction in single photon sources,[90] and photovoltaic devices to increase device efficiency by reducing energy loss in unwanted radiative or nonradiative pathways.[91] As the Purcell factor is dependent on the ratio Q/V_{eff} (Equation 1.6), it is important to maximize the quality factor and minimize the effective volume in order to maximize the enhancement in the fluorophore radiative rate. Investigating the possibility of observing this effect in polymer planar microcavities and the effect of the polymers used, and the cavity design to enable more efficient flexible devices is one of the objectives of this thesis.

Thesis Structure

This Thesis is organized into 7 Chapters and two appendices as follows:

Chapter 1: Introduction.

Chapter 2: Discusses the optimization of the geometrical structure of DBR polymer photonic vapor sensors for faster response.

Chapter 3: Discusses the development of holistic vapor sensors with wide selectivity and sensitivity to different range of volatile organic compounds.

Chapter 4: Discusses the development of multilayered polymer fluorescence sensors as on-off volatile organic compound sensors by using AIE effects.

Chapter 5: Demonstrates the first observations of the "Purcell effect" in all-polymer planar microcavities.

Chapter 6: Demonstrates the reproducibility of the Purcell effect the near-infrared spectral range.

Chapter 7: Discusses the outlook of the possible development for the results put forward in this thesis.

Appendix A: List of Publications

Appendix B: Conference Contributions and News Coverage

References

(1) Gholami, F.; et al. Morphological, interfacial and rheological properties in multilayer polymers: A review. *Polymer* **2020**, *208*, 122950.

(2) Morris, B. A. *The science and technology of flexible packaging: multilayer films from resin and process to end use*; William Andrew, 2022.

(3) Sedkaoui, Y.; et al. Elaboration and characterization of multilayer polymeric membranes: effect of the chemical nature of polymers. *J. Polym. Eng.* **2021**, *41*, 127-136.

(4) Ho, S.; et al. Review of recent progress in multilayer solution-processed organic light-emitting diodes. *J. Photonics Energy* **2015**, *5*, 057611-057611.

(5) Iler, R. K. Multilayers of colloidal particles. *J. Colloid Interface Sci.* **1966**, *21*, 569-594.

(6) Wagner Jr, J. R. *Multilayer flexible packaging*; William Andrew, 2016.

(7) Stenzel, O. *The physics of thin film optical spectra*; Springer, 2015.

(8) Peng, J.; et al. Inverse Nacre-like Epoxy-Graphene Layered Nanocomposites with Integration of High Toughness and Self-Monitoring. *Matter* **2020**, *2*, 220-232.

(9) DeVol, R. T.; et al. Nanoscale Transforming Mineral Phases in Fresh Nacre. *J. Am. Chem. Soc.* **2015**, *137*, 13325-13333.

(10) Potyrailo, R. A.; et al. Towards outperforming conventional sensor arrays with fabricated individual photonic vapour sensors inspired by Morpho butterflies. *Nat. Commun.* **2015**, *6*, 7959-7959.

(11) Seshan, K. *Handbook of Thin Film Deposition Techniques Principles, Methods, Equipment and Applications*; Noyes Publications, 2002.

(12) Richardson, J. J.; et al. Technology-driven layer-by-layer assembly of nanofilms. *Science* **2015**, *348*, aaa2491.

(13) Baer, E.; Zhu, L. 50th Anniversary Perspective: Dielectric Phenomena in Polymers and Multilayered Dielectric Films. *Macromolecules* **2017**, *50*, 2239-2256.

(14) Ponting, M.; et al. Gradient Multilayer Films by Forced Assembly Coextrusion. *Ind. Eng. Chem. Res.* **2010**, *49*, 12111-12118.

(15) *3M Italia DICROIC FILM, La Defense – Almere, archiproducts*. https://www.archiproducts.com/en/products/3m-italia/dichroic-dicroic-film_106387 (accessed 2022 10-11-2022).

(16) Gher, R. J.; Boyd, R. W. Optical properties of nanostructured optical materials. *Chem. Mater.* **1996**, *8*, 1807.

(17) Berti, L.; et al. Spectroscopic Investigation of Artificial Opals Infiltrated with a Heteroaromatic Quadrupolar Dye. *J. Phys. Chem. C* **2010**, *114*, 2403-2413.

(18) Wilmsen, C. W.; et al. *Vertical-cavity surface-emitting lasers: design, fabrication, characterization, and applications*; Cambridge University Press, 2001.

(19) Lova, P.; et al. Advances in functional solution processed planar one-dimensional photonic crystals. *Adv. Opt. Mater.* **2018**, *6*, 1800730-1800726.

(20) Mackay, T. G.; Lakhtakia, A. The transfer-matrix method in electromagnetics and optics. *Synthesis lectures on electromagnetics* **2020**, *1*, 1-126.

(21) Sultanova, N.; et al. Dispersion Properties of Optical Polymers. *Acta Phys. Pol. A* **2009**, *116*, 585.

(22) Lova, P.; et al. Strategies for dielectric contrast enhancement in 1D planar polymeric photonic crystals. *Appl. Sci.* **2020**, *10*, 4122.

(23) Frezza, L.; et al. Directional enhancement of spontaneous emission in polymer flexible microcavities. *J. Phys. Chem. C* **2011**, *115*, 19939 – 19946.

(24) Lova, P.; et al. All-Polymer Photonic Microcavities Doped with Perylene Bisimide J-Aggregates. *Adv. Opt. Mater.* **2017**, *5*, 1700523.

(25) Álvarez, A. L.; et al. Polymeric multilayers for integration into photonic devices. *Thin Solid Films* **2003**, *433*, 277-280.

(26) Manfredi, G.; et al. Directional Fluorescence Spectral Narrowing in All-Polymer Microcavities Doped with CdSe/CdS Dot-in-rod Nanocrystals. *ACS Photonics* **2017**, *4*, 1761–1769.

(27) Gazzo, S.; et al. High Refractive Index Hyperbranched Polyvinylsulfides for Planar One-Dimensional All-Polymer Photonic Crystals. *J. Polym. Sci., Part B: Polym. Phys.* **2016**, *54*, 73-80.

(28) Tavella, C.; et al. High Refractive Index Inverse Vulcanized Polymers for Organic Photonic Crystals. *Crystals* **2020**, *10*, 154.

(29) Giusto, P.; et al. Colorimetric Detection of Perfluorinated Compounds by All-Polymer Photonic Transducers *ACS Omega* **2018**, *3*, 7517-7522.

(30) Shen, H.; et al. One-dimensional photonic crystals: fabrication, responsiveness and emerging applications in 3D construction. *RSC Adv.* **2016**, *6*, 4505-4520.

(31) Fenzl, C.; et al. Photonic Crystals for Chemical Sensing and Biosensing. *Angew. Chem. Int. Ed.* **2014**, *53*, 3318-3335.

(32) Foelen, Y.; Schenning, A. P. H. J. Optical Indicators based on Structural Colored Polymers. *Adv. Sci.* **2022**, *9*, 2200399.

(33) Chiappini, A.; et al. Photonic Crystal Stimuli-Responsive Chromatic Sensors: A Short Review. *Micromachines* **2020**, *11*, 290.

(34) Harsányi, G. Polymer films in sensor applications: a review of present uses and future possibilities. *Sens. Rev.* **2000**, *20*, 98-105.

(35) Cho, S. H.; et al. Colorimetric Sensors for Toxic and Hazardous Gas Detection: A Review. *Electron. Mater. Lett.* **2021**, *17*, 1-17.

(36) Trovato, V.; et al. A Review of Stimuli-Responsive Smart Materials for Wearable Technology in Healthcare: Retrospective, Perspective, and Prospective. *Molecules* **2022**, *27*, 5709.

(37) Breul, A. M.; et al. Fluorescent monomers as building blocks for dye labeled polymers: synthesis and application in energy conversion, biolabeling and sensors. *Chem. Soc. Rev.* **2013**, *42*, 5366-5407.

(38) Demirel, G. B.; et al. Extremely fast and highly selective detection of nitroaromatic explosive vapours using fluorescent polymer thin films. *Chem. Commun.* **2013**, *49*, 6140-6142.

(39) Yang, J.-S.; Swager, T. M. Porous shape persistent fluorescent polymer films: an approach to TNT sensory materials. *J. Am. Chem. Soc.* **1998**, *120*, 5321-5322.

(40) Rochat, S.; Swager, T. M. Fluorescence sensing of amine vapors using a cationic conjugated polymer combined with various anions. *Angew. Chem. Int. Ed.* **2014**, *53*, 9792-9796.

(41) Liu, Y.; et al. Fluorescent polyacetylene thin film sensor for nitroaromatics. *Langmuir* **2001**, *17*, 7452-7455.

(42) Plouzeau, M.; et al. Polymer/dye blends: Preparation and optical performance: A short review. *J. Appl. Polym. Sci.* **2022**, *139*, e52861.

(43) Lee, J.; et al. A protective layer approach to solvatochromic sensors. *Nat. Commun.* **2013**, *4*, 2461.

(44) Winnik, F. M. Photophysics of preassociated pyrenes in aqueous polymer solutions and in other organized media. *Chem. Rev.* **1993**, *93*, 587-614.

(45) Jenekhe, S. A.; Osaheni, J. A. Excimers and exciplexes of conjugated polymers. *Science* **1994**, *265*, 765-768.

(46) Mei, J.; et al. Aggregation-induced emission: together we shine, united we soar! *Chem.*

Rev. **2015**, *115*, 11718-11940.

(47) Korostynska, O.; et al. Review on state-of-the-art in polymer based pH sensors. *Sensors* **2007**, *7*, 3027.

(48) G. R, S.; et al. Review on new horizons of aggregation induced emission: from design to development. *Mater. Chem. Front.* **2021**, *5*, 1541-1584.

(49) Lova, P. Selective polymer distributed bragg reflector vapor sensors. *Polymers* **2018**, *10*, 1161.

(50) Kim, E.; et al. Colorimetric and Resistive Polymer Electrolyte Thin Films for Real-time Humidity Sensors. *ACS Appl. Mater. Interfaces* **2012**, *4*, 5179-5187.

(51) Lin, E.-L.; et al. Trapping Structural Coloration by a Bioinspired Gyroid Microstructure in Solid State. *ACS Nano* **2018**, *12*, 485-493.

(52) Wang, T.-H.; et al. Optical sensing of organic vapour based on polymer cholesteric liquid crystal film. *Liq. Cryst.* **2020**, *47*, 1390-1397.

(53) Foelen, Y.; et al. Photonic Liquid Crystal Polymer Absorbent for Immobilization and Detection of Gaseous Nerve Agent Simulants. *ACS Appl. Opt. Mater.* **2022**.

(54) Foelen, Y.; et al. An Optical Steam Sterilization Sensor Based On a Dual-Responsive Supramolecular Cross-Linked Photonic Polymer. *ACS Appl. Mater. Interfaces* **2020**, *12*, 16896-16902.

(55) Noh, H. L.; et al. Colorimetric chemosensor for detection of a volatile organic compound, ethylamine, under versatile conditions: Solution, thin-film, and dyed fabric. *Sens. Actuators, B* **2019**, *301*, 127079.

(56) Ahmad, M.; et al. Highly selective vapochromic fluorescence of polycarbonate films Doped with an ICT-Based solvatochromic probe. *J. Polym. Sci., Part B: Polym. Phys.* **2017**, *55*, 1171-1180.

(57) Majeed, S.; et al. Receptor free fluorescent and colorimetric sensors for solution and vapor phase detection of hazardous pollutant nitrobenzene; a new structural approach to design AIEE active and piezofluorochromic sensors. *J. Photochem. Photobiol., A* **2022**, *431*, 114022.

(58) Lova, P.; et al. Label-free vapor selectivity in poly(p-phenylene oxide) photonic crystal sensors. *ACS Appl. Mater. Interfaces* **2016**, *8*, 31941-31950.

(59) Blumstein, A.; Kumar, J. Barrier Properties of Ordered Multilayer Polymer Nanocomposites IB. *Dekker encyclopedia of nanoscience and nanotechnology* **2004**, *1*, 213.

(60) Hansen, C. M. *Hansen solubility parameters: a user's handbook*; CRC press, 2002.

(61) Mönch, W.; et al. Flory-Huggins swelling of polymer Bragg mirrors. *Appl. Phys. Lett.* **2006**, *89*, 164104.

(62) Lova, P.; et al. Flory–Huggins photonic sensors for the optical assessment of molecular diffusion coefficients in polymers. *ACS Appl. Mater. Interfaces* **2019**, *11*, 16872-16880.

(63) Ullman, A. M.; et al. Hybrid Polymer/Metal–Organic Framework Films for Colorimetric Water Sensing over a Wide Concentration Range. *ACS Appl. Mater. Interfaces* **2018**, *10*, 24201-24208.

(64) Pressly, J. F.; et al. Increased Polymer Diffusivity in Thin-Film Confinement. *Macromolecules* **2019**, *52*, 6116-6125.

(65) Thompson, R. L.; et al. Solvent accelerated polymer diffusion in thin films. *Macromolecules* **2005**, *38*, 4339-4344.

(66) Birks, J. B. *Organic molecular photophysics*; Wiley-Interscience, 1973.

(67) Tress, W. Perovskite Solar Cells on the Way to Their Radiative Efficiency Limit – Insights Into a Success Story of High Open-Circuit Voltage and Low Recombination. *Adv. Energy Mater.* **2017**, *7*, 1602358.

(68) Vahala, K. J. Optical microcavities. *Nature* **2003**, *424*, 839-846.

(69) Kavokin, A.; et al. *Microcavities*; Oxford University Press, 2017.

(70) Monifi, F.; et al. Tunable add-drop filter using an active whispering gallery mode microcavity. *Appl. Phys. Lett.* **2013**, *103*, 181103.

(71) Jordan, R. H.; et al. Efficiency enhancement of microcavity organic light emitting diodes. *Appl. Phys. Lett.* **1996**, *69*, 1997-1999.

(72) Michalzik, R. VCSEL Fundamentals. In *VCSELs: Fundamentals, Technology and Applications of Vertical-Cavity Surface-Emitting Lasers*, Michalzik, R. Ed.; Springer Berlin Heidelberg, 2013; pp 19-75.

(73) Nakamura, H.; et al. Ultra-fast photonic crystal/quantum dot all-optical switch for future photonic networks. *Opt. Express* **2004**, *12*, 6606-6614.

(74) Ma, G.; et al. Ultrafast all-optical switching in one-dimensional photonic crystal with two defects. *Opt. Express* **2006**, *14*, 858-865.

(75) Furchi, M.; et al. Microcavity-Integrated Graphene Photodetector. *Nano Letters* **2012**, *12*, 2773-2777.

(76) Zhi, Y.; et al. Single Nanoparticle Detection Using Optical Microcavities. *Adv. Mater.* **2017**, *29*, 1604920.

(77) Morozov, K. M.; et al. Efficient UV Luminescence from Organic-Based Tamm Plasmon Structures Emitting in the Strong-Coupling Regime. *J. Phys. Chem. C* **2020**, *124*, 21656-21663.

(78) Lidzey, D. G.; et al. Photon-Mediated Hybridization of Frenkel Excitons in Organic Semiconductor Microcavities. *Science* **2000**, *288*, 1620-1623.

(79) Esteso, V.; et al. Light-Harvesting Properties of a Subphthalocyanine Solar Absorber Coupled to an Optical Cavity. *Solar RRL* **2021**, *5*, 2100308.

(80) Benisty, H.; et al. Impact of planar microcavity effects on light extraction-Part I: basic concepts and analytical trends. *IEEE J. Quantum Electron.* **1998**, *34*, 1612-1631.

(81) Ribeiro, R. F.; et al. Polariton chemistry: controlling molecular dynamics with optical cavities. *Chem. Sci.* **2018**, *9*, 6325-6339.

(82) Joannopoulos, J. D.; et al. *Photonic crystals : molding the flow of light*; Princeton University Press, 2008.

(83) Khitrova, G.; et al. Nonlinear optics of normal-mode-coupling semiconductor microcavities. *Rev. Mod. Phys.* **1999**, *71*, 1591-1639.

(84) Vahala, K. *Optical Microcavities*; World Scientific Publishing Company, 2004.

(85) Choi, A. H. *Handbook of optical microcavities*; CRC Press, 2014.

(86) Canazza, G.; et al. Lasing from all-polymer microcavities. *Laser Phys. Lett.* **2014**, *11*, 035804.

(87) Gevaux, D. G.; et al. Enhancement and suppression of spontaneous emission by temperature tuning InAs quantum dots to photonic crystal cavities. *Appl. Phys. Lett.* **2006**, *88*, 131101.

(88) Romeira, B.; Fiore, A. Purcell Effect in the Stimulated and Spontaneous Emission Rates of Nanoscale Semiconductor Lasers. *IEEE J. Quantum Electron.* **2018**, *54*, 1-12.

(89) Cho, H.; et al. Importance of Purcell factor for optimizing structure of organic light-emitting diodes. *Opt. Express* **2019**, *27*, 11057-11068.

(90) Wang, J.; et al. Spontaneously coherent orbital coupling of counterrotating exciton polaritons in annular perovskite microcavities. *Light Sci. Appl.* **2021**, *10*, 45.

(91) Zheng, X.; Zhang, L. Photonic nanostructures for solar energy conversion. *Energy Environ. Sci.* **2016**, *9*, 2511-2532.

Chapter 2: Optimization of DBR Polymer Photonic Vapor Sensors
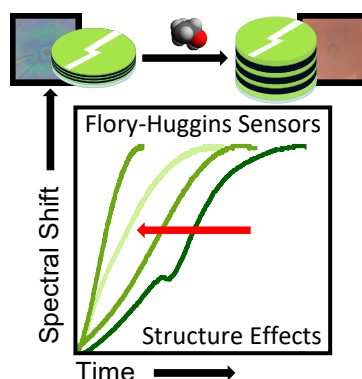
Abstract

Multilayered photonic sensors that rely on polymer-solvent Flory-Huggins interactions are drawing increasing interest owing to their broad-band selectivity, even among mixtures, without the need for chemical targeting. Moreover, these sensors provide simple colorimetric responses, and easy, quick fabrication both on laboratory and industrial scales. However, complex optical responses and slow response times are limiting their development. In this work, the behavior of different photonic sensor architectures is analyzed to speed-up response time and define a strategy to simplify their spectral behavior. To this end, the effect of interfaces, materials order, and thickness on the diffusion kinetics of a single reference analyte in the multilayered sensors is studied to design the optimal structure.

This chapter is partially reproduced from:

1. Introduction

Fast and low-cost detection of vapor analytes is important for monitoring food degradation,[1, 2] breath analyses,[3] industrial processes control,[4] and air pollution surveillance.[5] For instance, continuous and extensive monitoring of vapor pollutants[6] is critical to preserve the well-being of communities in urban and industrial environments due to the large toxicity,[7-10] reported carcinogenicity,[11] and extensive industrial and urban sources of these compounds.[7, 12, 13] Likewise, monitoring the quality of sealed environments, such as food packaging, could increase shelf-life and guarantee quality both to consumers and to producers within the food supply chain.[14, 15] To reach these targets, the detection system must circumvent complicated laboratory analysis and provide fast, low-cost, and easily interpretable readings through simple procedures. Polymer Flory-Huggins photonic sensors (FHPSs) are promising candidates for this task. FHPSs consist in multilayers made of alternated polymers with different refractive indices forming dielectric lattices called Distributed Bragg Reflectors (DBRs), that are well-known in different fields of photonics.[16, 17] The interaction between light and these structures generates reflection and refraction processes at any interface of the multilayer that result in the formation of a diffraction pattern, characterized by spectral regions where light cannot propagate within the crystal and is back-reflected.[18] These regions, called photonic band gaps (PBGs), are detectable in the reflectance spectrum of the FHPS as maxima.[19-21] The spectral position of these features (λ_{PBG}) can be roughly described as a function of the layers' refractive indices, n_H and n_L, and their thickness, d_H and d_L, for media having high (H) and low (L) indices using the Bragg-Snell equation (Equation 2.1): [22, 23]

$$\lambda_{PBG} = 2\sqrt{d_L + d_H}\sqrt{d_L n_L^2 + d_H n_H^2} \qquad (2.1)$$

Then, modifying the refractive index, the thickness or both affects the FHPS diffraction pattern and optical response. These effects are exploited in sensing, in a manner similar to more complicated photonic structures.[24, 25] Spectral variations detectable in FHPSs, at times even as color changes, can be correlated to the stimuli that induced the variation.[18] In the detection of molecular pollutants, exposing a FHPS to the analyte, the intercalation of the latter within the polymer structure causes one or both polymer media to swell, modifying the sensor optical spectrum and providing the typical colorimetric response.[6, 22, 26, 27] The capability of polymer thin films to undergo large swelling[28] leads to a notable spectral response of these sensors that can be seen even with the naked eye as color variation when the PBG is tuned in the visible

spectral range. Furthermore, the typically narrow spectral width of the PBG allows the detection of very small variations and consequently high sensitivity and lower detection limits in FHPSs.[18] The aforementioned characteristics are making these polymer photonic sensors increasingly researched.[18, 29-34] The first polymer multilayered sensors were made of cross-linked or sputtering-deposited polymers, and showed sensitivity to a few vapor-phase analytes.[35, 36] Only recently, the working principle of these systems has been elucidated and extended to commodity and commercial polymers processed by spin-coating deposition, opening new opportunities also for multilayered structures fabricated by melt-processing on very large area.[37-39] For example, polystyrene (PS):cellulose acetate (CA) FHPSs where PS was loaded with ZnO nanoparticles demonstrated sensitivity below 1 ppm and lower detection limit of 20 ppm to toluene.[40] Similar systems have been demonstrated as selective sensors to short-chain alcohols,[22] halogenated and aryl hydrocarbons,[6, 41] and even perfluorinated species.[27] In these cases, selectivity was achieved by exploiting the different chemico-physical interactions between polymer and analyte, that are described by the Hildebrand, Hansen and more generally, the Flory-Huggins interaction parameters after which these sensors are named. In turn, the different interactions allow for different diffusion behavior and kinetics, that lead to distinct spectral responses and, accordingly, to selectivity. The fact that a thermodynamic parameter can be employed to describe diffusive processes in polymers should not be surprising. Indeed, diffusion depends on both difference of potential and accumulation, that can be defined by the polymer-solvent interaction.[42] A similar approach is in fact used in chromatographic processes.[43] More recently, a similar working principle was also applied to unstructured commercial packaging films, where the interaction between polymer and analytes allows modification in the film interference pattern, and in turn the identification of the intercalating species.[26]

Aside from this selectivity, high sensitivity even among mixtures,[44] and optimal lower detection limit, all these sensors provide relatively slow responses that make their exploitation difficult in real polluted environments. Indeed, while analyte quantification and identification can be achieved in few minutes,[41, 44, 45] the full characterization of the system to gather properties such as the molecular diffusion constant of the analytes within the polymers commonly require the collection of the response for a longer time. Previous works reported faster responses for structures having low number of layers or very thin films.[44, 46, 47] On the other hand, the role of film thickness and interfaces in FHPSs where macromolecules are highly

confined and stressed has never been properly explained.[22, 41, 47] This work aims to define all the structural parameters affecting the diffusion process of the molecular species into the multilayer, and then the response time of the sensors. To this end, I investigated the effect of the number of layers, individual layer thickness and stacking order on the diffusion kinetics and response time of the FHPS. Isopropyl alcohol (IPA), a compound widely used in sanitation and the electronics industry was used as a prototype analyte. To detect this compound, I employed CA and PS as active sensing media within the FHPSs. The two polymers are soluble in IPA to different extents, where the solubility of PS is lower as deduced from their Hildebrand solubility parameters; $\Delta\delta^2_{IPA/PS}$= 24.01 while $\Delta\delta^2_{IPA/CA}$= 12.96 MPa.[22] As such, PS is expected to experience higher equilibrium swelling than CA.

2. Results and Discussion

The FHPSs chosen in this investigation constitute of stacked layers of PS and CA thin films (each pair of layers will henceforth be referred to as a bilayer and the capping layer of PS as half a bilayer). I analyzed three classes of FHPS. First, samples made of one bilayer of similar overall thickness (ℓ), but different polymer order (i.e. substrate-PS-CA and substrate-CA-PS) were fabricated to test the influence of the nature of the first interface contacting the analyte. Second, to investigate the effect of the layer thickness (i.e. FHPS period), three samples made of two bilayers capped with PS (2.5 bilayers) and increasing average layer thicknesses (80, 110 and 220 nm) were cast on a glass substrate (i.e. substrate-(PS-CA)×2-PS). Third, 13 samples with average layer thickness (80 nm) and increasing number of bilayers from 1.5 to 15.5, and correspondingly overall thickness, were tested to determine the influence of the number of internal FHPSs interfaces. Since samples made of 1.5 bilayers or less exhibit only thin-film interference, and thus low reflectivity, they were cast on silicon substrates to increase the reflection intensity, while all the other samples were cast on glass substrates. All the tested samples and their fabrication parameters are reported in the experimental section (Table 2.2).

Spectral Response of FHPS

The optical response of all the samples to air saturated with IPA was monitored through collecting the FHPS reflectance spectrum every set time interval. Figure 2.1a schematizes the process of IPA intercalation and the consequent FHPS layer swelling. As mentioned in the

introduction of this chapter, when the FHPS is exposed to the IPA both polymers swell and the FHPS color, that corresponds to the PBG spectral position, red-shifts due to the increase of layer thicknesses.
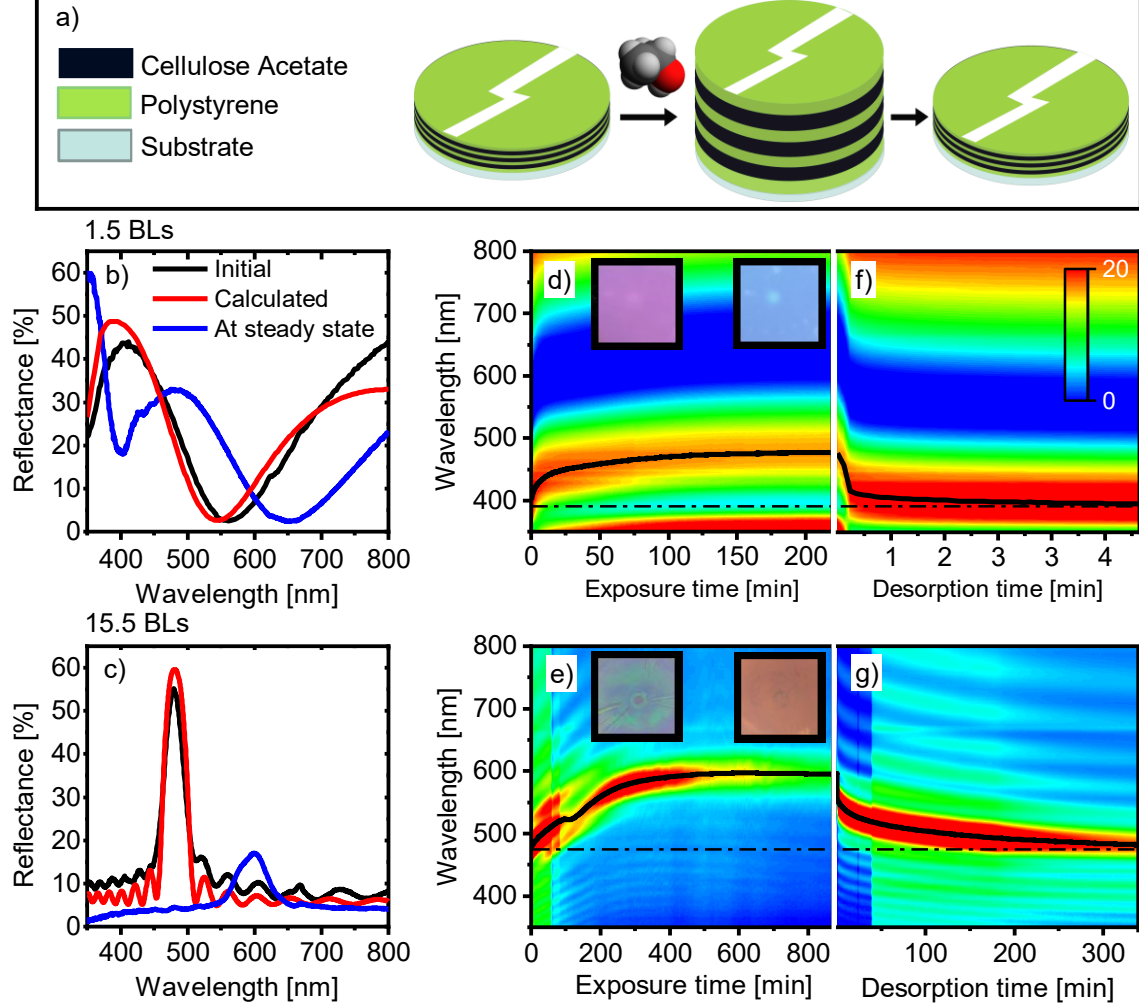
Figure 2.1. a) Schematic representation of multi-layered samples and their response to IPA vapor. b,c) Experimental (black) and calculated (red) reflectance spectra before the exposure and experimental spectra collected at the steady state (blue) for samples with b) 1.5 bilayers and c) 15.5 bilayers. d,g) Reflectance spectra contour plots as a function of exposure time for d)1.5 bilayers sample, e)15.5 bilayers. The intensity is represented as a color scale, the insets show photographs of the samples before (left) and after the exposure (right). Panels f) and g) show the desorption process for 1.5 and 15.5 bilayers, respectively.

Removing the IPA atmosphere, the specimen layers return to their original thickness, and the PBG blue-shifts to the initial position. Figure 2.1b and 1c report the typical spectral response of two of the structures reported in this work. The first is one of the simplest architectures and

is made by 1.5 bilayer (PS-CA-PS, panels b and d in Figure 2.1). The second example is a sample made of 15.5 bilayers (panels c and e in Figure 2.1).

Observing the reflectance spectra of the pristine structures (black lines in panels b and c), one notices that their optical response is very different. As mentioned above, the spectrum of the samples with the smaller number of layers consists in a Fabry–Pérot interference pattern arising from constructive and destructive interference between light beams partially reflected at the top and bottom sample surfaces (panel b). In fact, the spectrum consists of intensity oscillations with a maximum at about 410 nm (constructive interference) and a minimum at 560 nm (destructive interference). In this case, the low number of layers does not allow the formation of a dielectric lattice, and accordingly does not display a PBG. Concerning the spectrum of the thicker sample (15.5 bilayers, panel c), a sharp and intense reflectance maximum positioned at 480 nm is noticed. Such a feature is the signature of the PBG. The background of the spectrum is dominated by an interference pattern, similar but denser than the one described for the thinner sample. Indeed, as demonstrated in previous works, the thickness of a polymer thin film can be linked to its interference pattern by simple geometrical consideration.[22, 26] Both the spectra were modelled via transfer matrix method (TMM, see experimental section) to retrieve the geometrical thicknesses of any layer (d) and in turn the global sample thickness (ℓ). The simulated data are reported as red lines in panels b and c of Figure 2.1 and are in good agreement with the experimental ones. This procedure was repeated for all the samples and the thicknesses retrieved are reported in Tables 2.1 and 2.2 which will be discussed later. As described before, the exposure to IPA of the two samples induces a swelling of the polymer layers, and in turn an increase of the optical path within the structures. This produces a bathochromic shift of the spectral features observed for both structures (blue line). For the 1.5 bilayer sample, the maximum initially positioned at 410 nm moves to 485 nm (Figure 2.1b), while the PBG position for the sample made of 15.5 bilayers moves from 480 nm to 600 nm (Figure 2.1c).

Figure 2.1d and e show the overall temporal response of the two samples as contour plots. There, the wavelength is reported on the y-scale, while the exposure time is on the x-scale and the color scale represents the reflectance intensity. In this way, reflectance minima are in blue shades while maxima are in red (compare with Figure 2.1b and c), with solid black lines highlighting the spectral position of chosen maxima along the entire process. Concerning the sample with the lower number of layers (Figure 2.1d), at time t=0 the minimum (blue) and the

maximum (red) reflectance values are detectable at 410 nm and 560 nm, in agreement with the spectra of Figure 2.1b. Proceeding with the exposure to IPA, these two features shift monotonically to the long wavelength side of the spectrum. The shift velocity is initially faster and then decreases until the spectral position of both features reaches the steady state (equilibrium) after about 180 minutes of exposure. The same qualitative behavior is also visible for the exposure of the sample with the highest number of bilayers as well in the exposure contour plot in Fig. 2.1e. The PBG for the 15.5 bilayer sample (see Fig. 2.1c) is clearly identifiable in red tones, and its spectral position moves to longer wavelengths during the exposure with similar behavior but much slower kinetics than the sample previously discussed. The fringes of the aforementioned sample shift in a similar manner, but also decrease in intensity with time, probably due to a loss of planarity of the one or both outermost interfaces of the structure. Notably, the intensity of the PBG decreases significantly after approximately 100 minutes and increases again due to sequential distortion and restoration of the periodicity in the FHPS upon the uneven swelling of the polymers. Indeed, as the vapor migrates from the sample surface into deeper layers, the more superficial layers are more swollen than those closer to the substrate, interrupting the periodicity as previously demonstrated for similar systems.[18, 22] The exposure was repeated for all samples and a comparison of their behavior will be discussed further on.

The FHPS color change seen by naked-eye detection can be seen in the insets of Fig. 2.1d and e. The digital images show the color of the corresponding samples before exposure (left) and after reaching the equilibrium (right). The sample with 1.5 bilayers appears purple before exposure, owing to the high intensity of reflections at 410 nm and the fringe at around 800 nm, while the other appears bluish-green due to the PBG at 480 nm. The strong coloration of the sample made of 1.5 bilayers is mainly assigned to the reflectance of the silicon substrate, which enhances the coloration. After exposure, the purple color of the 1.5 bilayers sample shown in Figure 2.1d matches the expected color in the spectrum as the reflection fringe with largest intensity moves to around 480 nm, while the orange color of the 15.5 bilayers sample in Fig. 2.1e reflects the final position of the PBG at around 600 nm. Because the refractive index of liquid IPA is $n_{IPA} = 1.37$[48], while $n_{PS} = 1.59$ and $n_{CA} = 1.48$, the effective refractive index change due to the intercalation of IPA within the structure would not be significant compared to the thickness variation.[22, 26] In fact, assuming the hypothetical extreme case where CA (the more soluble of the two polymers) is completely replaced with IPA without changing its volume, the

modification of the optical thickness of the structure would be less than 4%. Thus, the variation in optical thickness, and consequently in color and spectral response, are assumed to arise solely from change in volume during sorption.[41, 49]

As reversibility is desirable for reusable sensors, even though the low cost of FHPSs would make them cost-efficient disposable devices, the desorption process was also investigated. Panels f and g of Fig. 2.1 show the contour plots for the 1.5 and 15.5 samples respectively upon removal of IPA vapors. In these plots the features for both the samples move to shorter wavelengths as the polymers shrink as a result of analyte desorption until the process reaches a steady state. In both cases, the initial stages of desorption are faster, similar to the characteristics of diffusion behavior in the case of sorption. At the end of the desorption process, the spectral position of the fringes as well as the PBG is identical to the initial ones, as highlighted with a dash-dot line indicating the starting and final positions of the maxima indicated in black before exposure and after desorption.

The contour plots for samples of increasing number of BL from 3.5 to 13.5 during exposure and desorption are reported in Fig. 2.2. For all the samples, the exposure follows the same behavior as described for the 1.5 and 15.5 bilayer samples in Fig. 2.1, demonstrating a red shift of the reflectance maxims on exposure until reaching a steady state. The demonstrated spectral reversibility is evident in all samples that were given a chance to completely desorb the analyte in room condition, returning to their initial position with negligible variation (see dashed black lines). When comparing the dynamics of desorption of the systems, it is significantly slower in the thicker samples than for their thinner counterparts as can be seen from the time scale.
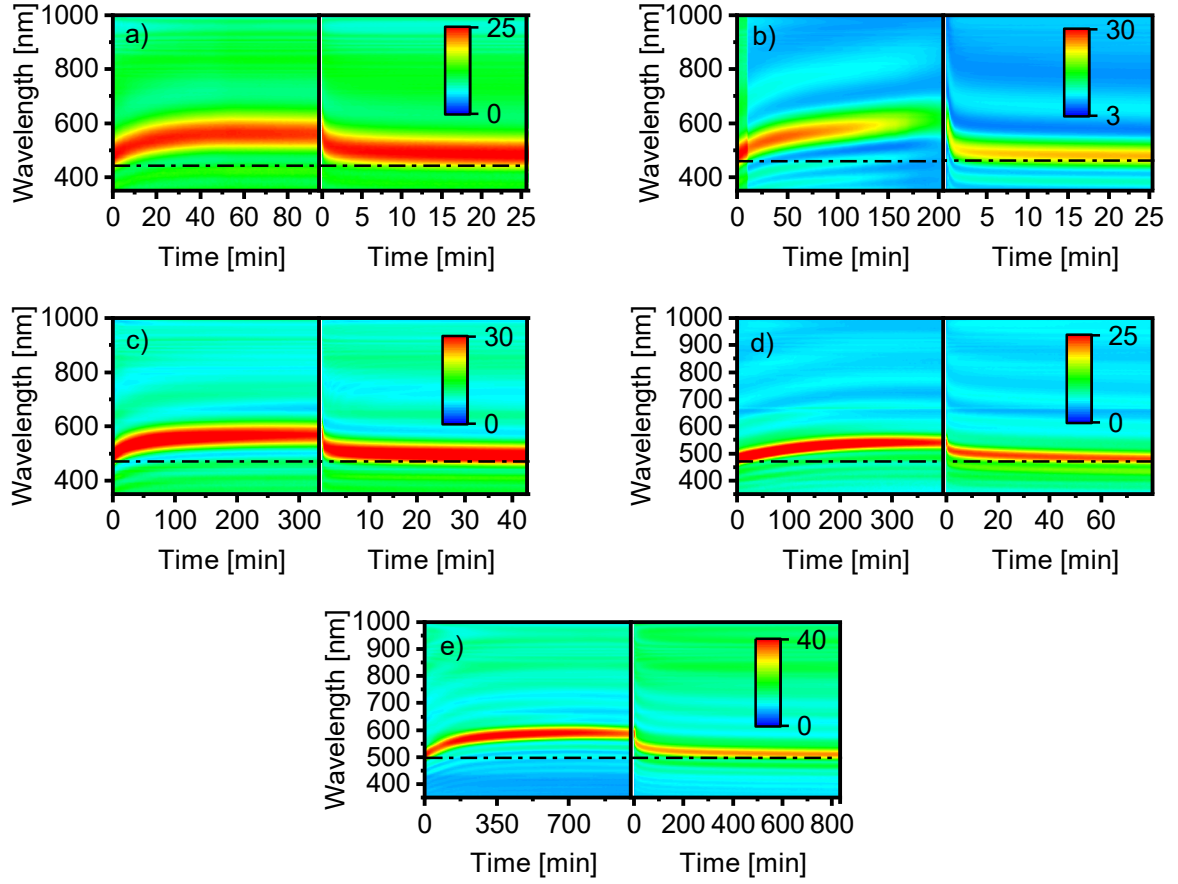
Figure 2.2. Contour plots for exposure (left) and desorption (right) for a) 3.5, b) 4.5, c) 5.5, d) 10.5, e) 13.5 bilayer samples with intensity represented as a color scale.

Sorption Kinetics

To investigate the sorption dynamics, the spectral position of all the relative maxima (fringes and PBGs) was tracked along the exposures for all the samples. For additive volumes the polymer mass intake (M) can actually be related to the change in the film thickness and, in the case of fringes and DBRs, the change in the reflectance peak wavelength. It has also been demonstrated that the spectral shift normalized to that at the steady state is equal to the normalized mass intake of the polymer film in the same manner, $\frac{\Delta M(t)}{\Delta M(t_{ss})} = \frac{\Delta \lambda(t)}{\Delta \lambda(t_{ss})}$.[22] Thus, Crank's well-established solution to Fickian diffusion[42] can be expresses as in Equation 2.2. When considering short exposure times (i.e. when there is no accumulation and the mass intake is less than 20% of that at steady state $\frac{\Delta \lambda(t)}{\Delta \lambda(t_{ss})} < 0.2$), the normalized spectral shift is expressed as a function of ℓ, the exposure time t, and the effective diffusion coefficient D_{eff}:

This analysis allowed the retrieval of the optical sorption curves (OSCs) for all the samples by plotting the normalized spectral shift ($\Delta\lambda/\Delta\lambda_{ss}$) over the square root of the exposure time, which allows determining the effective diffusion coefficient of IPA within the multilayered structures.

$$\frac{\Delta M(t)}{\Delta M(t_{ss})} = \frac{\Delta\lambda(t)}{\Delta\lambda(t_{ss})} = \frac{2}{\ell}\sqrt{\frac{D_{eff}}{\pi}}\sqrt{t} \qquad (2.2)$$

Table 2.1 lists all the samples characterized and reports ℓ, time to a shift of 10 nm ($t_{10\,nm}$), time to reach the steady state (t_{ss}), the effective diffusion coefficient for intercalation (D_{eff}) and desorption (D_{desrop}). Data in Table 2.1 confirm the disparity in the kinetics between the samples of Fig. 2.1. A better understanding of this difference can be reached by further examining the behavior of the sensors as it relates to their structure.

Table 2.1. Properties and response metrics for all tested samples.

Sample (bilayers)	ℓ (nm)	t_{ss} (h)	$t_{10\,nm}$ (s)	D_{eff} (cm^2 s^{-1} .10^{-13})	D_{desorp} (cm^2 s^{-1} .10^{-13})
1.5	245	3.08	120	2	46
2.5	395	3.55	330	1	210
3.5	554	0.851	244	4	143
4.5	731	4.37	493	3	543
5.5	890	4.36	486	4	927
8.5	1398	10.6	720	6	-
10.5	1622	5.11	1210	7	794
13.5	2233	11.70	1687	10	5963
15.5	2401	9.68	2430	8	3667
2.5	535	6.45	360	3	-
2.5	1215	19.9	1500	4	-
CA-PS	950	1.24	420	2	-
PS-CA	890	1.57	4	538	-

Influence of Structure on Response Time and Diffusion Kinetics

Figure 2.3 reports the effective diffusion coefficient for all measured samples. In detail, Fig. 2.3a shows the data for the multilayers against the number of layers (top x-axis) and ℓ (bottom x-axis). The average thickness of the component layers, that is half of the FHPS periodicity, is approximately 80 nm (see Table 2.1). The values of the effective diffusion coefficient range from 2×10^{-13} cm^2 s^{-1} for the 1.5 bilayer sample, to 8×10^{-13} cm^{2}s^{-1} for the 15.5 bilayers one, showing a clear increase of D_{eff} with the number of layers and with the overall thickness of the system. This approach makes it difficult to disentangle the effects of these two parameters on the diffusivity. To separate these effects, I repeated the measurement on samples having the same number of layers, but different total thickness, obtained by increasing the thickness of the single layer composing samples with the same architecture. Figure 2.3b reports the data collected for 3 samples made of 2.5 bilayers with global thickness ranging from 395 to 1215 nm. For these samples, the value of D_{eff} ranges from 1×10^{-13} cm^2 s^{-1} to 4×10^{-13} cm^{2}s^{-1}. Hence, increasing ℓ leads to an increase in the effective diffusion coefficient, albeit to a slower extent than for multilayers of higher number of layers. If the value of $\Delta D_{\text{eff}}/\Delta \ell$ are considered through the best-fit line obtained from these two sets of data, for samples where both thickness and number of layers are modified (Fig. 2.2a) it is 17% larger than in the case where only the thickness increases. This means that both the parameters (number of interfaces and thickness) affect the molecular diffusivity within the multilayers, and that the increase in the number of interfaces accounts for roughly 20% of the diffusivity increase. These findings are in agreement with literature data showing that the effective diffusion coefficient for thin polymer films increases with their thickness[50] in the range from nanometers[51-53] to micrometers.[54-56] Conversely, the diffusion coefficient of thicker samples approaches the value of the bulk materials.[51, 57] Since the individual layers in our multilayered samples have a thickness of less than 200 nm but the overall thickness is between 250 nm and 2500 nm, the increase in the diffusion coefficient can be assigned mainly to the increase of ℓ for the polymer structure. Nonetheless, the existence of more interfaces is shown to enhance the diffusion. One possible explanation might be the accumulation of the analyte at the interfaces[58] as a step in the diffusion process, increasing the concentration and the diffusion coefficient.[59] In fact, it has been reported that the concentration of the sorbed species is higher at the interface of a layer than at its core, increasing diffusivity;[60] a typical behavior in some amorphous polymers related to their mechanical relaxation.[59]
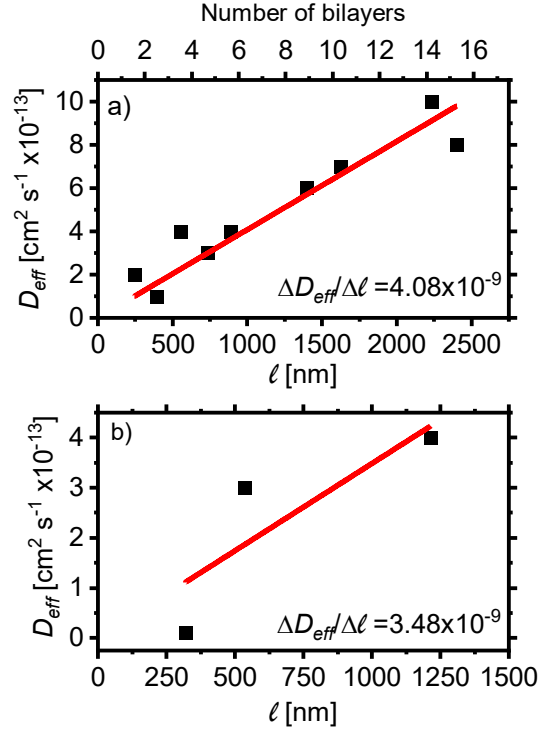
Figure 2.3. Effective diffusion coefficient retrieved from OSCs for a) samples with different number of bilayers and b) 2.5 bilayers of different thicknesses.

I also investigate the effect of the top FHPS interface (environment-capping layer) in contact with the vapor environment. This interface indeed rules the analyte solubilization within the structure. For this reason, two samples consisting of 1 single bilayer of reversed layer ordering were exposed to IPA under the same conditions. The optical sorption curves retrieved for these samples are reported in Fig. 2.4. The sample labeled PS-CA (blue) has PS cast first on the substrate and CA as the capping layer, the first interface with the vapor, and vice versa for the sample labeled CA-PS (red). The sample capped with PS shows an IPA effective diffusion coefficient of 2×10^{-13} cm^2 s^{-1}, while for the sample capped with CA the value is increased more than 260-fold, suggesting that the larger solubility of the capping layer[61] strongly enhances the diffusivity in the entire system. In agreement, mathematical models of heat transfer and diffusion in multilayered slabs indicate that the first interface is indeed important in ruling the kinetics, specially at low stacking.[62, 63] However, the time necessary to reach the steady state is limited by the layers of higher diffusion resistance.[64, 65] Indeed, the OSCs for the single bilayer samples as reported in Fig. 2.4 show that the normalized spectral shifts reach the steady state at similar exposure times. Nonetheless, the sample with CA as the first interface

(blue line) shows faster swelling than the one capped with PS at shorter exposure times. These findings demonstrate the existence of different diffusion regimes for the two systems, but also that they do not affect the global time needed to reach equilibrium. These results are important when multilayers are designed for sensing applications. Previous works demonstrated that in this case the first part of the curve can be used to disentangle analytes and define their concentration.[22, 26] Then, to this end, capping the FHPSs with a polymer showing high solubility in the analyte can strongly speed-up the detection. On the other hand, for determining the diffusion regimes the entire OSC is needed, making the effect of the capping layer negligible over the overall measurement time domain.
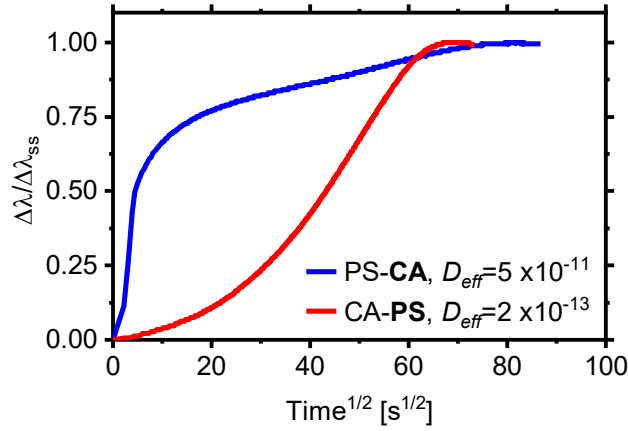
Figure 2.4. Optical sorption curves for single-bilayer samples of different order. Capping layer highlighted in bold; CA for the blue line and PS for the red.

To better explain this point, panels a and b of Fig. 2.5 report t_{10nm}, which is a conservative shift that can be effectively used in sensing when simple portable spectrometers are used. Fig. 2.5a shows that this number increases from 2 min to 40 min with the number of bilayers and sample thickness and, counterintuitively, with the effective diffusion coefficient. Figure 2.5b, which reports $t_{10\,nm}$ for samples with the same number of interfaces but increasing thickness, confirms an increase of this characteristic time with thickness. However, according to the lines of best fit, a 10 nm increase in the overall thickness in samples with the same number of layers would extend t_{10nm} by around 10 seconds as opposed to only 3.6 s for the other set. This again is another indication of an accelerating effect arising from the presence of interfaces. Concerning instead the effect of the capping layer (see Table 2.1), the sample capped with CA shows a 100-fold shorter time, and then faster response, with respect to the one capped with PS. Summarizing, faster response is obtained for thinner films capped with the polymer with the

larger solubility in the analyte, and with larger number of interfaces.

Regarding the equilibrium response, Fig. 2.5c and 2.5d reports t_{ss}. As observed for t_{10nm}, there is a linear correlation between the sample thickness and t_{ss}. Again, it is possible to provide a rough quantification of the effects observed by analyzing the step increases of the characteristic times over the increase in ℓ, analyzing the fitting line of the data retrieved. For the 2.5 system, $\Delta t_{ss}/\Delta\ell$ is about three times larger compared to the multilayers. Moreover, $\Delta t_{ss}/\Delta\ell$ $\sim 50(\Delta t_{10nm}/\Delta\ell)$. This means that increasing the overall thickness of the system has a negative effect on the response time. On the other hand, a large number of interfaces speeds up the process. Then, to engineer the sensor response to be fast enough, the following should be done: i) Increase the number of interfaces; ii) Reduce the individual layer thickness; ii) Select as capping layer a polymer more soluble within the analytes.
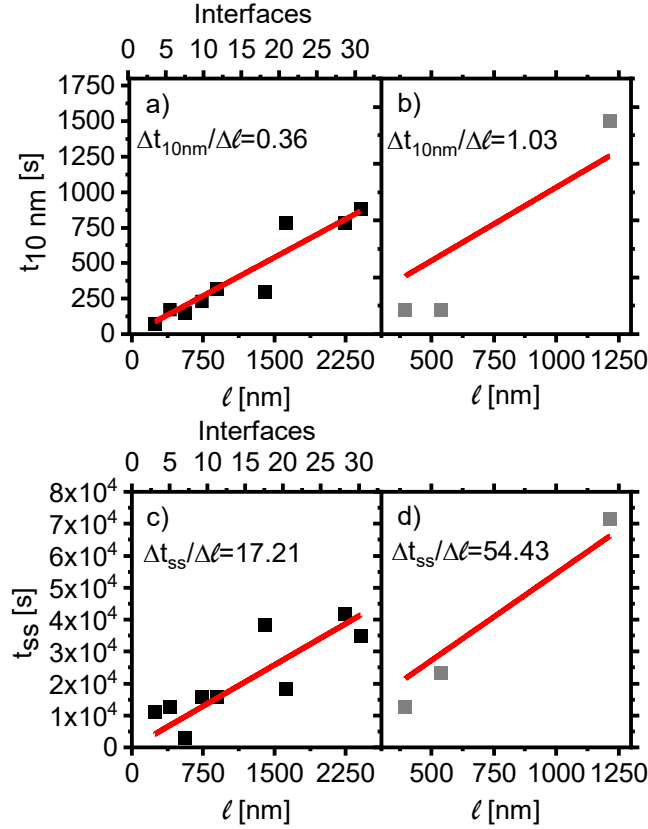
Figure 2.5. Time for a spectral shift of 10 nm for a) samples with increasing number of bilayers and b) samples of 2.5 bilayers and increasing average layer thickness. Time to steady state of c) samples with increasing number of bilayers and d) samples with increasing average layer thickness.

Considering that the sensing can be performed on either PBGs or interference fringes, one could think to design a sensor having affinity with several analyte families, stacking films of polymers with suitable affinity even without creating a photonic structure. On the other hand, the presence of a PBG favors a simple colorimetric detection.

The optimization of the number of layers and their thickness is evidently important in achieving faster sensing. On the other hand, the large response time of the proof-of-concept sensors is by far inadequate for real applications. However, the design principles here reported can be applied to FHPSs with intrinsically faster response to further accelerate the kinetics. For instance, introducing a hybrid inorganic-polymer nanocomposite film as a component in the FHPSs has been already shown to decrease their response time.[47]

Desorption Kinetics

As mentioned before, analyte desorption is critical for reversibility. Indeed, achieving full desorption on a short timescale can allow these sensors to be reused. Figure 2.6a reports the time required for the sample to fully restore the initial spectral response at room conditions (t_d) for the samples with increasing number of interfaces (from 1.5 to 15.5 bilayers) plotted against the global sample thicknesses, ℓ. The desorption time increases non-linearly with thickness, with the thinnest sample taking less than 5 minutes to fully desorb IPA while the sample with 15.5 bilayers takes more than five hours. In Fig. 2.6b, we notice that also the effective diffusion coefficient for the IPA desorption process increases in a similar manner with the sample thickness. It is easy to notice that the desorption occurs on a substantially faster timescale than the sorption. Such difference arises partly from the different boundary conditions. During analyte intercalation the driving force decreases with the exposure time. Indeed, while IPA is in unitary and constant activity in the surrounding environment, the concentration within the sample increases from zero to the equilibrium value. Instead, during desorption the environmental concentration of IPA can be approximated to zero along the entire process (desorption in air), thus enhancing the driving force of the diffusion.

Another possible contributing effect is that the breaking and formation of weak bonding among the solvent molecules, and between solvent and polymers may present different activation energy.[66] In previous papers, the interactions were inferred by analyzing the Hildebrand solubility parameters. A step forward in understanding the interactions occurring within the sensor can be achieved by using the Hansen solubility parameters accounting for the role of

dispersion, polar and Hydrogen bonding forces. For our data the square difference in the Hansen solubility parameters (in MPa) for dispersion, polar and hydrogen bonding is respectively $\Delta\delta^2_d=6.25$, $\Delta\delta^2_p=108.16$ and $\Delta\delta^2_h=20.25$ for CA-IPA, $\Delta\delta^2_d=30.25$, $\Delta\delta^2_p=0.09$ and $\Delta\delta^2_h=146.41$ for PS-IPA.[61] Smaller values indicate stronger interactions and so, one can deduce that there is non-negligible hydrogen bonding between CA and IPA and a strong polar interaction between PS and IPA, as previously demonstrated.[67] The combination of all these phenomena modifies the kinetics.
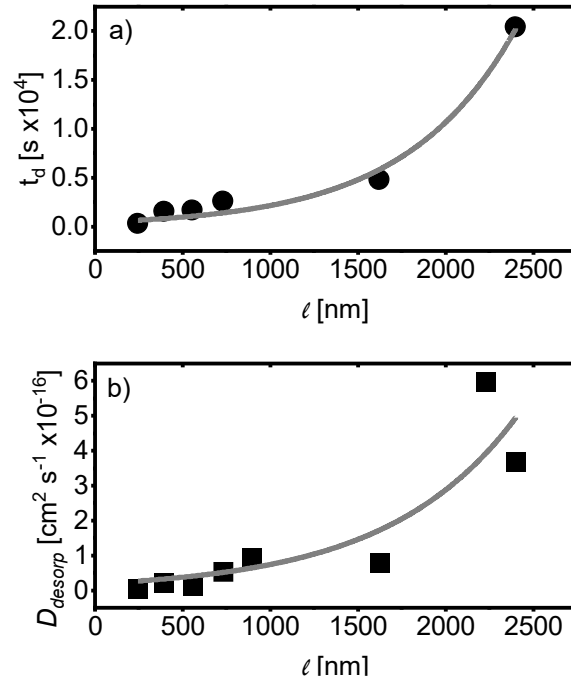
Figure 2.6. a) Time to complete the desorption process, t_d, b) effective diffusion coefficient for samples with increasing ℓ.

3. Conclusion

This chapter provided a systematic investigation of the role of thickness, number of interfaces and different architectures in FHPSs including thin films and distributed Bragg reflectors. For this task, PS:CA multilayered structures were employed as proof-of-principle systems to detect IPA vapors. The analysis was performed through modifying layer thicknesses, number of interfaces in the samples as well as the capping layer and optically evaluating the sensor response times and the analyte effective diffusion coefficients. The results obtained allow the perfect design of FHPSs for both sensing and determining diffusion properties. In all cases, the

increase of the overall thickness was seen to have a negative effect on the response time. On the other hand, increasing the number of interfaces speeds up the response more significantly. Then I can conclude that when the pure colorimetric response typical of photonic systems is not required, thinner systems of sufficient thickness to detect the film interference pattern are preferable. Stacking of different polymers can be used to enhance selectivity without strongly affecting the response time negatively. Finally, spectral reversibility has been demonstrated for multilayered samples, which also show sorption-desorption hysteresis. Hence, this shows that the response time can be tailored as desired, depending on the strength of the polymer-solvent interaction using an appropriate configuration of the structure. In conclusion, the investigated system and structures are promising as a basis for designing fast all-polymer vapor sensors, circumventing the need of using inorganic or hybrid structures.

4. Materials and Methods

Sample Preparation. All the samples were cast either on glass substrates or on silicon by alternating spin-coating of PS (Sigma-Aldrich, M_w=192000) and CA (Sigma-Aldrich, M_n=50000) dissolved in toluene (Sigma-Aldrich, 99.8%) and diacetone alcohol (4-Hydroxy-4-methyl-2-pentanone, Sigma-Aldrich, 99%) respectively. Subsequently, samples were annealed for two minutes at 80 °C. The concentration of each solution and the rotation speed employed for each sample are reported in Table 2.2.

Characterization. Reflectance data was collected through an optical fiber-based setup, utilizing a deuterium-halogen lamp (Micropak DH2000BAL). The light was sent to the sample surface using a y-bundle fiber (Avantes FDP-7UVIR2002-2 VAR) that also collects the reflected signal and relays it to an Avantes 2048 spectrometer (resolution 1.4 nm, spectral range 200 nm – 1100 nm).[41, 47] To assess the evolution of the optical response, (9 mm^2) square samples were placed at the tip of an immersion probe (Avantes FDP-7UVIR200-2-yy). The fiber bundle was then aligned at normal incidence with respect to the sample surface and connected to the same light source and spectrometer used for reflectance measurements. The probe was then immersed in an air environment saturated with IPA by placing solvent (0.5 mL) in a sealed tube. Next, the time-dependent reflectance spectra were recorded at set intervals until the sample response reaches the steady state. All the measurements were made at room temperature, pressure, and humidity.

Table 2.2. Solution concentration, substrate and average layer thickness for all investigated samples.

Sample	Rotation speed (rps)	$\bar{d}_i$	Substrate	PS conc. (mg/mL)	CA conc. (mg/mL)
PS-CA	80	445	Silicon	60	60
CA-PS		475	Silicon		
2.5 bilayer	200	110	Glass	30	30
	140	220	Glass	60	60
1.5 bilayer			Silicon		
2.5, 3.5, 4.5, 5.5, 8.5, 10.5, 13.5, and 15.5 bilayers	175	80	Glass	30	27

Spectra Modeling. The thicknesses of the samples were retrieved by fitting the experimental reflectance spectra through a TMM MATLAB® code developed in-lab as previously described.[18] The refractive index of substrates and polymers previously characterized and reported in literature were used as inputs.[68-70]

5. References

(1) Karpas, Z.; et al. Determination of volatile biogenic amines in muscle food products by ion mobility spectrometry. *Anal. Chim. Acta* **2002**, *463*, 155-163.

(2) Pacquit, A.; et al. Development of a volatile amine sensor for the monitoring of fish spoilage. *Talanta* **2006**, *69*, 515-520.

(3) Fleischer, M.; et al. Detection of volatile compounds correlated to human diseases through breath analysis with chemical sensors. *Sens. Actuators, B* **2002**, *83*, 245-249.

(4) Lindinger, W.; et al. On-line monitoring of volatile organic compounds at pptv levels by means of proton-transfer-reaction mass spectrometry (PTR-MS) medical applications, food control and environmental research. *Int. J. Mass Spectrom. Ion Processes* **1998**, *173*, 191-241.

(5) Marć, M.; et al. Current air quality analytics and monitoring: A review. *Anal. Chim. Acta* **2015**, *853*, 116-126.

(6) Lova, P. Selective polymer distributed bragg reflector vapor sensors. *Polymers* **2018**, *10*, 1161.

(7) Wang, S.; et al. Volatile organic compounds in indoor environment and photocatalytic oxidation: State of the art. *Environ. Int.* **2007**, *33*, 694-705.

(8) Duan, J.; et al. Concentration, sources and ozone formation potential of volatile organic compounds (VOCs) during ozone episode in Beijing. *Atmos. Res.* **2008**, *88*, 25-35.

(9) Lippmann, M. Health effects of ozone a critical review. *Japca* **1989**, *39*, 672-695.

(10) Seinfeld, J. H.; Pandis, S. N. *Atmospheric Chemistry and Physics: From Air Pollution to Climate Change*; John Wiley & Sons, 2012.

(11) Phillips, M.; et al. Volatile organic compounds in breath as markers of lung cancer: a cross-sectional study. *Lancet* **1999**, *353*, 1930-1933.

(12) Guo, H.; et al. Risk assessment of exposure to volatile organic compounds in different indoor environments. *Environ. Res.* **2004**, *94*, 57-66.

(13) Vlaanderen, J.; et al. Tetrachloroethylene exposure and bladder cancer risk: A meta-analysis of dry-cleaning-worker studies. *Environ. Health Perspect.* **2014**, *122*, 661-666.

(14) Comyn, J. *Polymer Permeability*; Springer Science & Business Media, 2012.

(15) Siracusa, V. Food packaging permeability behaviour: A report. *Int. J. Polym. Sci.* **2012**, *2012*, 1-11.

(16) Lova, P.; et al. All-polymer methylammonium lead iodide perovskite microcavities. *Nanoscale* **2019**, *11*, 8978-8983.

(17) Antonioli, D.; et al. PTFE-PMMA core-shell colloidal particles as building blocks for self-assembled opals: synthesis, properties and optical response. *Polym. Int.* **2012**, *61*, 1294.

(18) Lova, P.; et al. Advances in functional solution processed planar 1d photonic crystals. *Adv. Opt. Mater.* **2018**, *6*, 1800730.

(19) Saleh, B. E.; Teich, M. C. *Fundamentals of Photonics*; John Wiley & Sons, 2019.

(20) Comoretto, D. *Organic and Hybrid Photonic Crystals*; Springer International Publishing, 2015.

(21) Cheng, S.-C.; et al. Effect of atomic position on the spontaneous emission of a three-level atom in a coherent photonic-band-gap reservoir. *Phys. Rev. A* **2009**, *79*, 013801.

(22) Lova, P.; et al. Flory–Huggins photonic sensors for the optical assessment of molecular diffusion coefficients in polymers. *ACS Appl. Mater. Interfaces* **2019**, *11*, 16872-16880.

(23) Manfredi, G.; et al. Cellulose ternary photonic crystal created by solution processing. *Cellulose* **2016**, *23*, 2853-2862.

(24) Zhang, Y.; et al. Photonic sensing of organic solvents through geometric study of dynamic reflection spectrum. *Nat. Commun.* **2015**, *6*, 7510.

(25) Wang, L.; Li, Q. Stimuli-Directing Self-Organized 3D Liquid-Crystalline Nanostructures:

From Materials Design to Photonic Applications. *Adv. Funct. Mater.* **2016**, *26*, 10-28.

(26) Lova, P.; et al. Thin polymer films: simple optical determination of molecular diffusion coefficients. *ACS Appl. Polym. Mater.* **2020**, *2*, 563-568.

(27) Giusto, P.; et al. Colorimetric detection of perfluorinated compounds by all-polymer photonic transducers. *ACS Omega* **2018**, *3*, 7517-7522.

(28) Flory, P. J. *Principles of Polymer Chemistry*; Cornell University Press, 1953.

(29) Resende, P. M.; et al. Cost-effective, flexible, hydrophobic, and tunable structural color polymeric bragg reflector metastructures. *Adv. Opt. Mater.* **2018**, *6*, 1800408.

(30) Kou, D.; et al. BTEX vapor detection with a flexible mof and functional polymer by means of a composite photonic crystal. *ACS Appl. Mater. Interfaces* **2020**, *12*, 11955-11964.

(31) Kou, D.; et al. Copolymer-based photonic crystal sensor for discriminative detection of liquid benzene, toluene, ethylbenzene, and xylene. *ACS Appl. Polym. Mater.* **2020**, *2*, 2-11.

(32) Bol'shakov, E. S.; et al. Photonic crystal sensors for detecting vapors of benzene, toluene, and o-xylene. *Russ. J. Phys. Chem. A* **2018**, *92*, 1530-1534.

(33) Gao, S.; et al. Time-resolved analysis of dielectric mirrors for vapor sensing. *ACS Appl. Mater. Interfaces* **2018**, *10*, 36398-36406.

(34) van Heeswijk, E. P. A.; et al. Humidity-gated, temperature-responsive photonic infrared reflective broadband coatings. *J. Mater. Chem. A* **2019**, *7*, 6113-6119.

(35) Convertino, A.; et al. A new approach to organic solvent detection: High-reflectivity bragg reflectors based on a gold nanoparticle/teflon-like composite material. *Adv. Mater.* **2003**, *15*, 1103-1105.

(36) Mönch, W.; et al. Tunable Bragg filters based on polymer swelling. *Appl. Opt.* **2006**, *45*, 4284-4290.

(37) Andrews, J. H.; et al. Folding flexible co-extruded all-polymer multilayer distributed feedback films to control lasing. *Opt. Express* **2012**, *20*, 15580-15588.

(38) *3M™ Dichroic Films for Architectural Laminated Glass*. https://www.3m.com/3M/en_US/company-us/all-3m-products/~/3M-Dichroic-Films-for-Architectural-Laminated-Glass/?N=5002385+3291680356&rt=rud (accessed June 2019).

(39) *TORAY*. https://www.toray.com/ (accessed June 2019).

(40) Lova, P.; et al. Hybrid ZnO:polystyrene nanocomposite for all-polymer photonic crystals. *Phys. Status Solidi I* **2015**, *12*, 158-162.

(41) Lova, P.; et al. Label-free vapor selectivity in poly(p-phenylene oxide) photonic crystal

sensors. *ACS Appl. Mater. Interfaces* **2016**, *8*, 31941-31950.

(42) Crank, J. *The Mathematics of Diffusion*; Clarendon Press, 1975.

(43) Olabisi, O. Polymer compatibility by gas-liquid chromatography. *Macromolecules* **1975**, *8*, 316-322.

(44) Lova, P.; et al. Flory-Huggins Photonic Sensors for the Optical Assessment of Molecular Diffusion Coefficients in Polymers. *ACS Appl. Mater. Interfaces* **2019**, *11*, 16872-16880.

(45) Lova, P.; et al. Advances in functional solution processed planar one-dimensional photonic crystals. *Adv. Opt. Mater.* **2018**, *6*, 1800730-1800726.

(46) Reddy, K.; et al. On-chip Fabry–Pérot interferometric sensors for micro-gas chromatography detection. *Sens. Actuators, B* **2011**, *159*, 60-65.

(47) Lova, P.; et al. Polymer distributed bragg reflectors for vapor sensing. *ACS Photonics* **2015**, *2*, 537-543.

(48) Chu, K.-Y.; Thompson, A. R. Densities and refractive indices of alcohol-water solutions of n-propyl, isopropyl, and methyl alcohols. *J. Chem. Eng. Data* **1962**, *7*, 358-360.

(49) Bolton, B. A.; et al. Ethanol sorption and partial molar volume in cellulose acetate films. *J. Phys. Chem.* **1986**, *90*, 1207-1211.

(50) Buss, F.; et al. From micro to nano thin polymer layers: thickness and concentration dependence of sorption and the solvent diffusion coefficient. *Macromolecules* **2015**, *48*, 8285-8293.

(51) Eastman, S. A.; et al. Effect of confinement on structure, water solubility, and water transport in Nafion thin films. *Macromolecules* **2012**, *45*, 7920-7930.

(52) Thompson, R. L.; et al. Solvent accelerated polymer diffusion in thin films. *Macromolecules* **2005**, *38*, 4339-4344.

(53) Vogt, B. D.; et al. Moisture absorption into ultrathin hydrophilic polymer films on different substrate surfaces. *Polymer* **2005**, *46*, 1635-1642.

(54) Mensitieri, G.; et al. The effect of film thickness on oxygen sorption and transport in dry and water-saturated Kapton® polyimide. *J. Membr. Sci.* **1994**, *89*, 131-141.

(55) Shishatskii, A. M.; et al. Effects of film thickness on density and gas permeation parameters of glassy polymers. *J. Membr. Sci.* **1996**, *112*, 275-285.

(56) Petrak, K.; Pitts, E. Permeability of oxygen through polymers. II. The effect of humidity and film thickness on the permeation and diffusion coefficients. *J. Appl. Polym. Sci.* **1980**, *25*, 879-886.

(57) Frank, B.; et al. Polymer mobility in thin films. *Macromolecules* **1996**, *29*, 6531-6534.

(58) Carr, E. J.; March, N. G. Semi-analytical solution of multilayer diffusion problems with time-varying boundary conditions and general interface conditions. *Appl. Math. Comput.* **2018**, *333*, 286-303.

(59) Thomas, N. L.; Windle, A. H. A deformation model for Case II diffusion. *Polymer* **1980**, *21*, 613-619.

(60) Musto, P.; et al. Benzene-induced crystallization of ppo: a combined thermodynamic and vibrational spectroscopy study. *Ind. Eng. Chem. Res.* **2020**, *59*, 5402-5411.

(61) Hansen, C. M. *Hansen Solubility Parameters: A U'er's Handbook*; CRC press, 2002.

(62) Hickson, R. I.; et al. Critical times in multilayer diffusion. Part 1: Exact solutions. *Int. J. Heat Mass Transfer* **2009**, *52*, 5776-5783.

(63) Carr, E. J.; Turner, I. W. A semi-analytical solution for multilayer diffusion in a composite medium consisting of a large number of layers. *Appl. Math. Model.* **2016**, *40*, 7034-7050.

(64) Flynn, G. L.; et al. Mass transport phenomena and models: Theoretical concepts. *J. Pharm. Sci.* **1974**, *63*, 479-510.

(65) Manfredi, G.; et al. Lasing from dot-in-rod nanocrystals in planar polymer microcavities. *RSC Adv.* **2018**, *8*, 13026-13033.

(66) Vrentas, J. S.; Vrentas, C. M. Hysteresis effects for sorption in glassy polymers. *Macromolecules* **1996**, *29*, 4391-4396.

(67) Caze, C.; Pak, S. H. Inherent polarity of polystyrene upon miscibility in incompatible blends with low-density polyethylene. *J. Mater. Sci. Lett.* **1997**, *16*, 53-55.

(68) Frezza, L.; et al. Directional enhancement of spontaneous emission in polymer flexible microcavities. *J. Phys. Chem. C* **2011**, *115*, 199–9 - 19946.

(69) Fornasari, L.; et al. Fluorescence excitation enhancement by Bloch surface wave in all-polymer one-dimensional photonic structure. *Appl. Phys. Lett.* **2014**, *105*, 053303.

(70) Lova, P.; et al. All-polymer photonic microcavities doped with perylene bisimide j-aggregates. *Adv. Opt. Mater.* **2017**, *5*, 1700523.

Chapter 3: Holistic Vapor Sensors with Wide Selectivity
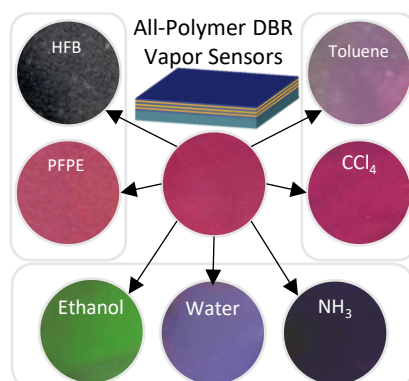
Abstract

A holistic detection system, in principle sensitive to any molecular species in the vapor phase is proposed. The sensor consists of a polymeric multilayered distributed Bragg reflector made of a perfluorinated polar polymer, Aquivion®, and a non-polar polymer, poly(N-vinylcarbazole). Alternated layers of the two polymers provide a characteristic optical response that depends on the chemical species intercalating within the structure. Such differences arise from Flory-Huggins polymer-solvent interactions. Then, the presence of polar, non-polar and perfluorinated moieties in the structures potentially allows sensitivity to any molecular species, providing a detection system with no need for any additional chemical receptors. As a proof of concept, the study demonstrates the sensitivity of the sensor to very diverse classes of molecules in the vapor phase including perfluorinated, non-polar hydrophobic, and hydrophilic species and the capability to distinguish them, even in binary mixtures. Additionally, a connection between the dynamic temporal response of the sensors and the chemical-physical properties of the analytes, their concentration, and effective diffusion coefficient within the polymer structure is revealed.

1. Introduction

Vapors of volatile organic compounds are ubiquitous in modern-day life, as they are an integral part of the manufacturing of several chemicals and goods and are widely released during fossil fuel combustion.[1] Not to mention, their release from biological sources including food degradation[2], composting[3] and metabolic processes.[4,5] and other sources.[6,7] Hence, their detection is of increasing significance in industrial processes,[8] air quality and goods degradation control,[9] as well as in medical diagnosis, where the presence of specific compounds in human breath is a well-known marker of certain diseases.[10, 11] Therefore, detection of organic vapors is critical to guarantee human well-being and health in strongly anthropized environments.[12] Currently, qualitative sensing is carried out using costly and time-consuming analyses which need complex sampling procedures[13, 14] which is why simple and low-cost on-site monitoring methods are of crucial necessity. In this regard, optical sensors based on polymer photonic crystals (PhCs) have been largely investigated owing to their low fabrication costs and ease of integration in lab-on-a-chip devices.[15-17]

PhC sensing is based on the variation of the lattice spectral response generated by changes in its effective refractive index (n_{eff}) and/or periodicity. Such variations can be provided, for instance, by the interaction between the chemical analyte and the lattice itself. These lattices show typical reflectance spectra displaying maxima at specific —and designed — frequencies where photons cannot propagate into the crystalline structure. Such frequency intervals are named photonic band gaps (PBGs) or stopbands, and their spectral features depend indeed on the lattice periodicity and dielectric contrast. Among several photonic structures reported for sensing, synthetic opal-like structures, liquid crystals[18-23] as well as one-dimensional mesoporous distributed Bragg reflectors (DBRs),[24-27] have been widely demonstrated as colorimetric sensors for gas and vapor analytes. As an example, mesoporous DBRs fabricated

by spin-coating of metal oxide nanoparticles showed selectivity by chemical labelling with alkoxysiloxanes,[28] and by molecular sieving employing zeolites in the DBR structure.[29] However, these systems have two main limitations. First, the high dielectric contrast between the components favors the formation of broad stopbands, which limit the detection of small spectral variations. Second, the mechanical rigidity of the structure only allows refractive index modifications without swelling, further limiting the sensitivity and the limit of detection. Then, the responses of these sensors usually consist in small spectral variations, which often require complex chemometric analyses.[30, 31] Furthermore, the fabrication process often requires time-demanding nanoparticle sintering, which is essential to grant mechanical stability to the structure but slows down the process, thus making their industrial scalability difficult.[32]

Polymer DBRs have the potential to overcome these issues. These structures can be grown by co-polymer self-assembly,[33] spin-coating,[34] or even by co-extrusion on an industrial scale.[35, 36] Moreover, their relatively low dielectric contrast allows spectrally narrow stopbands which are deleterious in light management applications, but allow the detection of very small analyte concentration variations in sensing.[37] Moreover, sensitivity is enhanced by the large analyte uptake typical of polymer media,[38] which can swell greatly favoring a much larger periodicity variation with respect to refractive index changes.[39, 40] The intercalation of an analyte into these polymer DBRs results in an easily detectable spectral (color) change even upon exposure to small environmental concentrations of analyte, which is often visible by the naked eye.[41, 42] Polymeric DBRs also show selectivity based on the different chemical-physical interaction parameters between the analytes permeating the structure and the polymers. Such process does not need any specific chemical labelling. Indeed, these parameters describe the solubility and diffusivity of the analytes within the polymer matrices and, therefore, their diffusion kinetics.[43] The dynamic spectral response of these sensors allows broad-band and label-free selectivity.

To gain an insight into this process, the polymeric thin films constituting these structures are considered as dense membranes in which molecular diffusion is ruled by the analyte solubility in the polymers themselves and not only by mass transport.[39, 44] Therefore, polymer and analyte pairs must have a certain chemical-physical affinity, that can be described, as a first approximation, through the Flory-Huggins parameter ($\chi = V^M \frac{\Delta\delta^2}{RT}$, neglecting entropic contribution), which is a function of the analyte molar volume (V^M) and of the squared difference in the Hildebrand solubility parameter for the pairs ($\Delta\delta^2$).[43] The latter expresses the difference of cohesive energy between analytes and polymers, so that the smaller the $\Delta\delta^2$, the larger the solubility.[43, 45] Sensors based on this principle are called Flory-Huggins photonic sensors (FHPSs)[39, 46] as the polymeric DBRs are the transduction devices. This method has been demonstrated for the detection of certain classes of chemicals in the liquid[42, 47, 48] and vapor phase,[49-52] showing label-free selectivity among several classes of compounds. For instance, the literature reports FHPS systems that are able to distinguish between different alcohols,[39] aromatic and aliphatic derivatives,[41, 46] and even systems sensitive to perfluorinated molecules.[51] On the other hand, the capability to detect all these classes of materials with a single sensor is still challenging. Combined with the need for disposable, fast and easy-to-use sensors,[53,54] the technological relevance of the FHPSs from both environmental monitoring and packaging point of view is evident.

Due to the binary nature of DBRs, so far FHPSs have only shown sensitivity to limited class of compounds.[39, 41, 50, 52, 55, 56] For instance, PS/CA structures show sensitivity to polar and non-polar species but not to fluorinated compounds.[39, 55] Conversely, when made of perfluorinated systems coupled to non-polar polymers, these FHPS are sensitive to similar species but not to polar molecules.[51] In this chapter I propose new all-polymer FHPSs containing three different moieties that lead to the detection of any class of compounds. The sensors are based on

alternated layers of Aquivion® and Poly(*N*-vinylcarbazole) (AQ/PVK). The AQ polymer is a perfluorinated system bearing polar –SO$_3$H functional groups and is promising for interaction with both perfluorinated and polar analytes (see inset in Fig. 3.1b). Importantly, AQ is used in the form of water/ethanol-suspensions which renders them easy to process from solution with good wettability and with no need to use fluorinated solvents. As such, it provides the low refractive index of fluorinated polymers, but with much easier processability and lower environmental impact. Conversely, PVK interacts with molecular species with low polarity. When in contact with polar or perfluorinated analytes, AQ acts as the active sensing medium undergoing swelling, while PVK, which shows low solubility in these analytes, rules the diffusion kinetics and provides label-free selectivity. On the other hand, when exposed to non-polar species, PVK acts as the active sensing medium, while AQ rules the analyte diffusion within the polymers. This duality promises to provide a holistic capability to detect analytes of different species, while a careful analysis of the sensor response also allows selectivity. To demonstrate this mechanism, we fabricated a multilayered sensor with the two polymers and exposed it to perfluorinated, polar, and non-polar compounds, including hexafluorobenzene (HFB), Galden® HT 55 perfluoropolyether, water, ammonia solution (NH$_3$-SOL), ethanol (EtOH), carbon tetrachloride (CCl$_4$) and toluene. I also investigate the response to binary mixtures as a starting point for the development of sensors for real-life applications, where analytes are present in complex mixtures.

2. Results

Design, Materials and Optical Response of Sensors

As a proof-of-principle sensors, I employed a DBR consisting of only 3 bilayers of PVK and AQ capped with a single layer of PVK (Fig. 3.1a). Figure 3.1b shows the refractive index of

AQ as well as its structure in the inset, showing a very low refractive index with negligible absorption in the 400-2500 nm spectral range. The spectral dispersion of n is also extremely low, with a large Abbe number of (V_D =91), which makes this polymer particularly suitable for achromatic photonic application requiring dispersionless materials. The low index of AQ provides a relatively high dielectric contrast with PVK (n_{PVK}=1.68). Thus, the normal incidence reflectance spectrum of the pristine FHPS in Fig. 3.1c (red line) clearly showing spectral features assigned to the stopbands even with a small number of periods.[57] As mentioned in the introduction, such high dielectric contrast favors the formation of spectrally broad stopbands, that could decrease the FHPS sensitivity. To overcome this limit, I exploited the second order stopband of the FHPSs, which is commonly spectrally sharper than the first stopband[37, 46] and was opportunely tuned in the visible spectral range for the sensing. As previously reported, this is possible, because the normalized optical responses of the different diffraction orders to the analyte exposure are superimposable.[39, 58] Notice that to be able to detect even diffraction orders, the structure needs to be far from the λ/4 condition[37] that emerges in DBRs having low and high refractive index media with identical optical thickness ($n_H d_H = n_L d_L$). In this condition the even diffraction orders of the lattice do not exist and the reflectance values of the odd order stopbands is maximized.[46, 59] Then, when the two materials have different optical thicknesses, it is possible to detect several sharp reflectance peaks and maximize the FHPS sensitivity. The spectrum shows three reflectance maxima, at 1200, 600 nm and 405 nm, corresponding to the first, second and third order stopbands of the lattice respectively. This assignment is confirmed by the agreement between the experimental data and those calculated with the refractive index of AQ in reported in Fig. 3.1c and that of PVK from literature[57] and the actual thickness of each layer: d_{AQ}=343 nm and d_{PVK}= 79 nm (see Experimental section for details). The background of the reflectance spectrum shows a Fabry–Pérot pattern arising from

the interference of beams reflected at the external interfaces of the FHPS. The pattern agrees

with a total sensor thickness of about 1345 nm. Figure 3.1 also schematizes the sample behavior

when exposed to different vapors. When non-polar compounds intercalate into the structure,

the PVK layers absorb the analyte and swell (Fig. 3.1a1). On the other hand, the intercalation

of perfluorinated or polar compounds will selectively swell the AQ layers (Fig. 3.1a2). In both

cases, the swelling of the polymer layers results in the variation of the FHPS optical response.
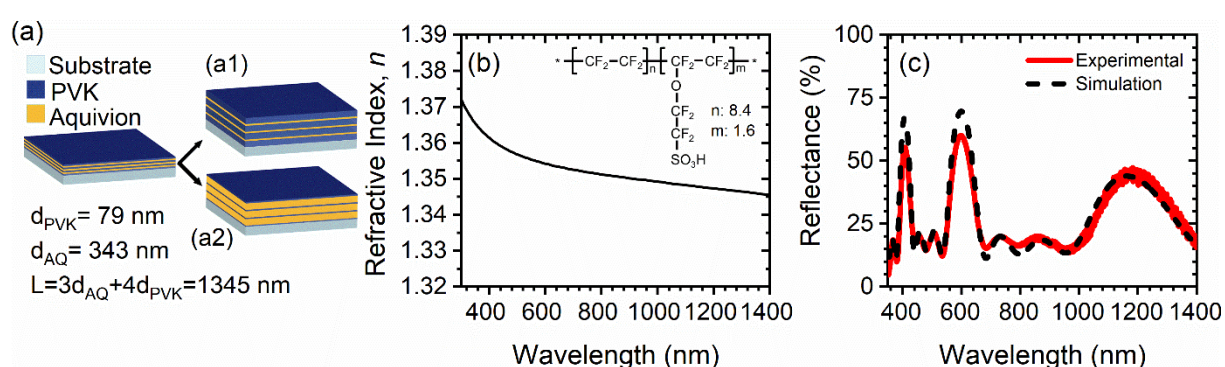
Figure 3.1. a) Schematic of structure and working principle of the FHPS during exposure to a1) non-polar compounds and a2) polar or perfluorinated compounds. b) Refractive index dispersion for Aquivion®, with its structure in the inset. c) Experimental and calculated reflectance spectra of the FHPS.

The spectral behavior of the FHPS when exposed to saturated water vapor is reported in Fig.

3.2 and is discussed further in the next section. The figure shows the reflectance spectrum of

the structure before (black line) and after (red) exposure. The dotted cyan line shows instead

the spectrum of the sample collected after sample exposure and drying in room conditions. The

pristine sample response was discussed in Fig. 3.1. When it is placed in a humid environment,

all the spectral features (stopbands and interference fringes) significantly red shift, confirming

the swelling of the polymer layers. In addition, these features undergo a considerable decrease

in the intensity, accompanied by their spectral broadening. This can be attributed to the

decrease in the optical quality of the structure.[58] Notice that the red shift is so pronounced that,

in addition to the second (953 nm) and third diffraction orders (641 nm) it is possible to detect up to the fourth FHPS stopband at 481 nm for the swollen structure. Upon removal of the analyte and allowing water desorption in room conditions, the FHPS reflectance superimposes that of the pristine structure (see grey dashed line), indicating full spectral reversibility. Remarkably, this exposure does not seem to change the optical quality of the film.

Diffusion Kinetics, Colorimetric Response and Selectivity of Sensors

As mentioned in the introduction, the kinetics of the spectral response provides selectivity to the FHPS. It is then worthwhile to describe its temporal evolution of the spectrum of the sensor in more detail. Throughout the process, the FHPS reflectance changes continuously. In the contour plot of Fig. 3.2b, colors indicate the intensity of the reflectance signal, where warmer colors represent higher values, with peaks in red, and the cooler ones lower signals, with troughs in blue. In the temporal (y-scale) evolution of the reflectance signal, the peaks are initially positioned at 405 and 600 nm (x-scale, third and second diffraction order, respectively). With exposure, the peaks shift quickly and monotonically to the long wavelength side of the spectrum. In the very first stages of the exposure the shift velocity is very large but decreases with time until the two features reach 643 and 950 nm respectively at steady state. Moreover, a third peak arises below 400 nm at the beginning of the process. This peak also moves towards the long wavelength side and, as mentioned, is assigned to the fourth-order stopband of the FHPS. The overall behaviors of the FHPSs give information about the kinetics of the diffusion and swelling processes. Tracking the spectral shift of individual peaks as a function of time allows retrieving a characteristic fingerprint of the analyte-FHPS interaction (Fig. 3.2c). In fact, on plotting the normalized shift of the second order stopbands against the square root of exposure time, one can construct OSCs analogous to those used in gravimetric methods.[60] In this case, it is possible to calculate the effective diffusion coefficient of the

analyte in the structure from the gradient of the initial (linear) portion of the curve (Fig. 3.2c) as previously reported (see Chapter 2).[39, 58]
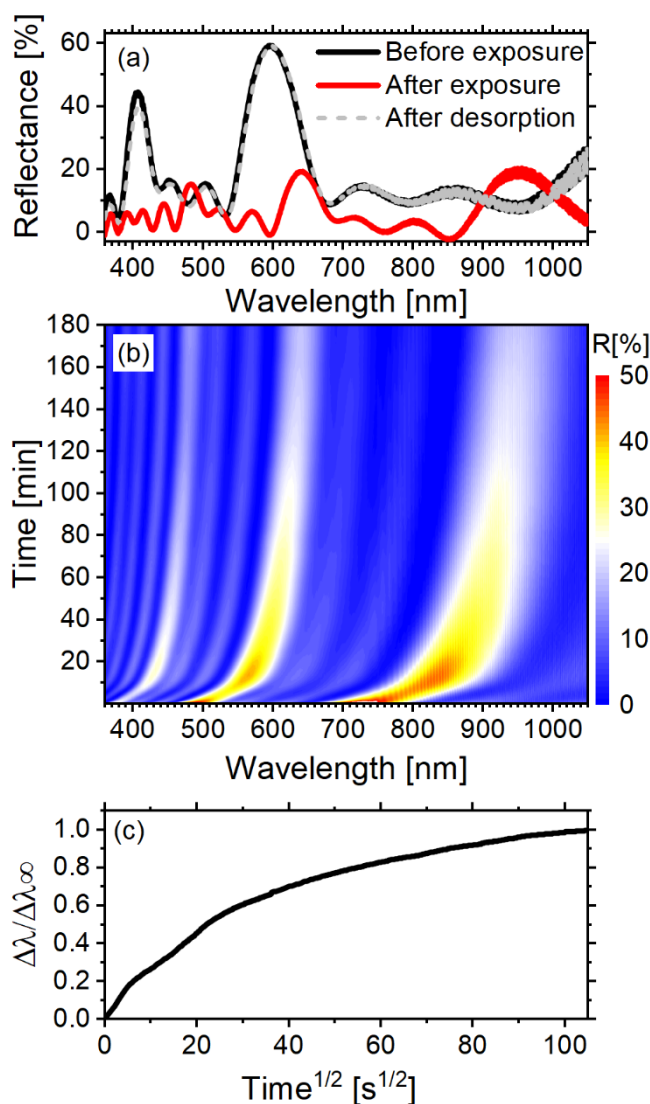
Figure 3.2. a) Reflectance spectrum of FHPS before and after exposure to water vapor and after complete desorption b) Temporal evolution of the spectral response of the sensor during water vapor exposure. c) Normalized spectral shift of the reflectance maximum peak -initially positioned at 405 nm- during the exposure.

The same procedure was repeated for exposure to the other analytes considered: CCl_4, EtOH, Galden® HT 55, HFB, NH_3-SOL, and toluene. The contour plots of the reflectance intensity during exposure of the FHPSs to the other analytes considered in this work (HFB, Galden® HT 55, NH_3-SOL, EtOH, CCl_4 and toluene) are reported in Fig. 3.3. Like water, the vapor of the

ammonia solution produces a large shift of the stopbands. Toluene also induces a smaller but significant spectral shift while, in contrast, exposure to Galden® HT 55 and CCl₄ shows limited effects. Not only do the plots show that the spectral shifts are distinct for different analytes, but that they also have different kinetics. Importantly, they show that the strong interactions with the NH₃ solution, EtOH, and HFB cause a destruction of the stopband, resulting ultimately in the decrease in the reflection intensity. On the other hand, toluene causes a significant shift reaching an equilibrium with no significant decrease in intensity. Finally, exposure to CCl₄ and Galden® caused a very small shift and no decrease in intensity.
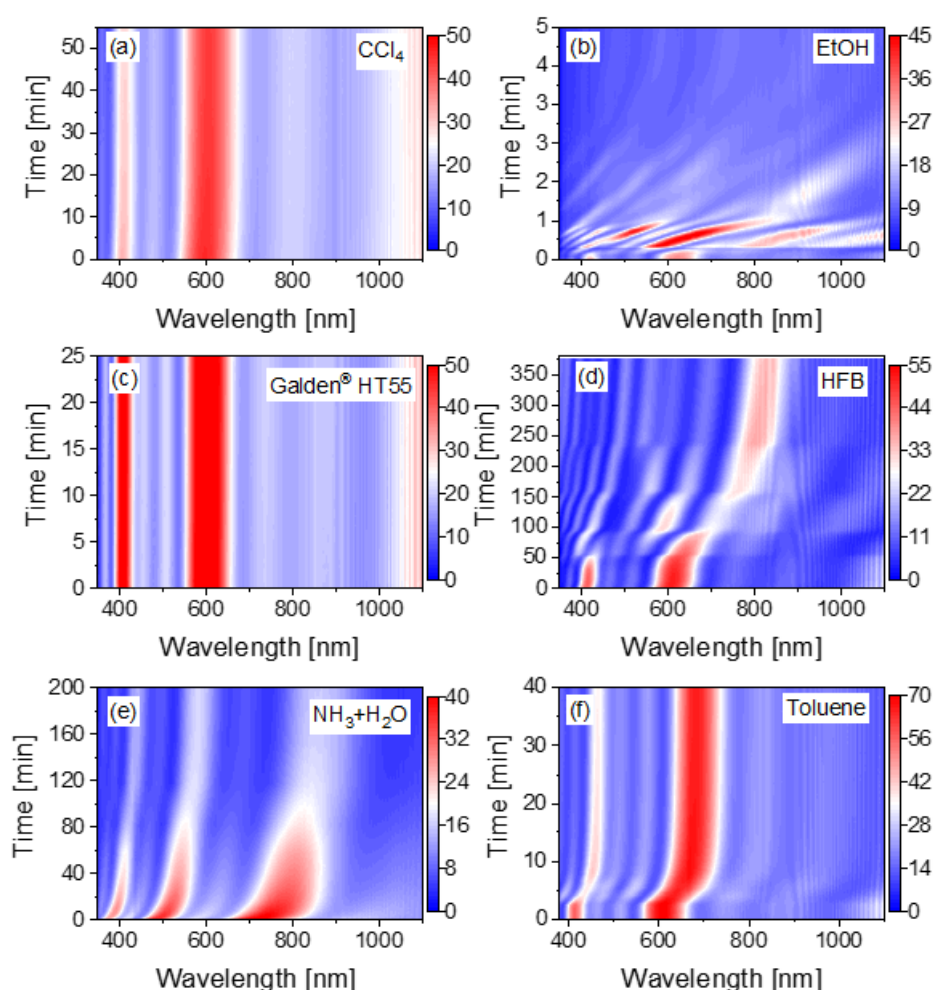
Figure 3.3. Contour plots for time evolution of the reflectance spectra upon FHPS exposure to vapors of a) carbon tetrachloride, b) ethanol, c) Galden® HT 55, d) hexaflourobenzene, e) ammonia solution and f) toluene.

The OSCs were retrieved for the FHPS on exposure to all the analytes (Fig. 3.4a) from the entire spectral response reported in Fig. 3.3. Additionally, those of binary mixtures of toluene HFB of different component ratios were retrieved from the entire spectral response (Fig. 3.4b). The OSCs of the sensor to different analytes, is reported in Fig. 3.4a, which confirms that the sensor undergoes strong spectral changes in response to all reported ones. Concerning perfluorinated compounds (HFB and Galden$^®$ HT 55), which are supposed to interact with the perfluorinated part of AQ, the sensor undergoes a spectral shift larger than 200 nm (see Table 3.1), with a rather slow response. Indeed, the system is not yet at equilibrium after 5 hours of exposure to HFB. Conversely, when exposed to Galden$^®$ HT 55 the system reaches equilibrium in less than one hour with a shift of about 4 nm. The different behaviors can be related to several properties that govern the diffusion process including solubility, concentration, and molar volume of the analyte. Concerning the polar compounds, which are supposed to interact with the polar moieties of AQ, the sensor shows very fast responses and strong swelling to EtOH, water and ammonia solution. All these compounds induce spectral shifts larger than 200 nm. The shift for EtOH is the largest while the smallest is for NH$_3$-SOL where the reaction with the -SO$_3$H groups gives rise to the corresponding ammonia salt. Notice that Fig. 3.4b shows that the large spectral shift and simultaneous decrease in signal intensity generated by EtOH exposure makes it impossible to evaluate the equilibrium shift for this analyte, then the effective diffusion coefficient value is probably underestimated. Concerning the kinetics, EtOH shows the fastest response, followed by water and ammonia solution. Last, the sensor was exposed to non-polar compounds including toluene and CCl$_4$, both of which reach equilibrium in less than 50 minutes. However, they exhibit very different diffusion kinetics; the FHPS response to the CCl$_4$ starts very quickly, reaching more than 35% within the first 5 seconds. After that, the diffusion kinetics slows significantly. On the other hand, toluene requires several

minutes to display any measurable change. Nonetheless, once the response begins, the kinetics is quite fast and on par with the initial one to CCl_4. The different spectral responses are easily detectable by the naked eye. Figure 3.4c shows digital photographs of the FHPS (cut from the same sample) collected before and after exposure to different vapors (at the steady state). Initially, the structure appears dark pink, owing to the high reflections in the violet (405 nm) and orange (600 nm) spectral regions coupled with the dark background. The unique appearance of the FHPSs after being exposed to different vapors is a result of both the shift of multiple reflection bands and interference fringes as well as the change in their intensity. For example, on exposure to HFB the band of highest intensity (at 600 nm) shifts to around 830 nm, in the NIR region, while the intensity of the other fringes drops below 15%, making the sample appear almost completely transparent in the visible range (note that the sample is cast on a transparent glass substrate and placed on a dark surface). Similarly, with NH_3-SOL the second order peak shifts to 890 nm, while the higher orders move to 600 and approximately 460 nm but decrease significantly in intensity, giving a slight purple tint to the otherwise transparent sample. Similarly, exposure to toluene vapors decreases the quality of the films, and in turn the intensity of the structural color. However, the purple color from the combination of the peaks present after exposure in the blue and red regions instead of the violet and orange is still noticeable. On the other hand, the 4 nm spectral shift (×3 the spectral resolution of the detector) induced by Galden$^®$ detected through the reflectance measurements shows only a slight color variation in the photograph. Similarly, no clear color variation is visible for CCl_4 by the naked eye. When it comes to the most striking color change, it is induced by exposure to H_2O and EtOH. While the spectral shift produced is accompanied by a decrease in intensity like the other vapors, the shift is fast enough that the color change is clearly visible when reaching the detectable steady state before the occurrence of any decrease in the film quality.

Similar OSC analyses to that discussed previously can be carried out for vapor mixtures to correlate the response with the proportion of the constituents (Fig. 3.4b).
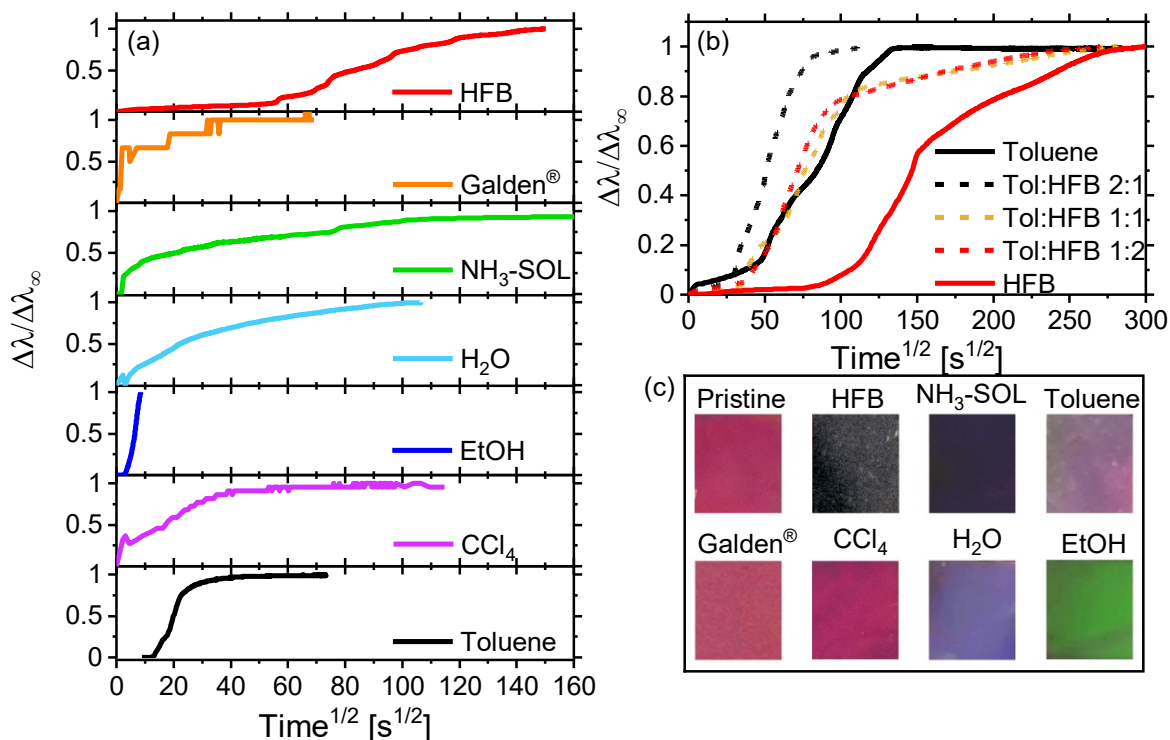
Figure 3.4. Optical Sorption Curves for a) all different chemical species and b) pure and binary mixtures of Toluene and HFB. c) Digital photographs of sensors before and after exposure to the labeled analytes.

In this case, the sensor's environment has been saturated using binary mixture of toluene and HFB with different volume ratios (2:1, 1:1 and 1:2 of Toluene: HFB) as well as the pure chemicals. The response to the mixtures is not as straightforward as expected, as they do not seem to follow an average behavior of the pure analytes. Both Toluene and HFB induce an initially slow response followed by a sharp increase in the swelling velocity ($\Delta\lambda/\Delta t$) until the systems reached the steady state. The mixtures display similar trends, but the curves are not in between those of the pure analytes, suggesting a more complex behavior. This can probably be ascribed to the fact that the two components of the mixture interact with both polymers composing the DBR.

Correlation Between Sensor Response and Analyte Properties

Table 3.1 compares the data retrieved from the OSC in Fig. 3.4a with physical and chemical parameters available in the literature that are expected to influence the spectral response of the FHPSs. The maximum spectral shift for the most intense peak as well as the retrieved effective diffusion coefficients are tabulated in the same table (see experimental section and the studies by Lova et al.[39, 58]). In addition, the table reports the vapor pressure (P_v), the molar volume (V_M) and Hildebrand solubility parameter δ_{tot} for all the analytes.[43] The effective Flory-Huggins parameter χ_{eff}, is the volume-weighted average of the interaction parameters for the concerned species with AQ and PVK. P_v directly correlates to the concentration of the analyte in closed environment above the liquid in which the samples are immersed, and therefore should be closely related to the dynamics of the response.[61, 62] On the other hand, molecular volume has been linked to the equilibrium swelling in similar FHPS systems,[39, 58] as well as its well-known influence in polymer-solvent interactions.[43, 63]

Regarding the spectral shifts at equilibrium, they can be divided into high (for EtOH, H_2O and NH₃-SOL) medium (for HFB), and low (for Toluene, CCl_4 and Galden® HT 55). The largest is provided by EtOH, which destroys the FHPS periodicity making the quantification impossible. Then, the provided value (312 nm) is an underestimation of the actual one. Likewise, both pure water and the ammonia solution provide large spectral shifts, between 265 and 280 nm, which are reversible upon desorption. It is interesting to note that the species providing the largest spectral shifts are all polar. HFB, a non-polar aromatic compound, causes a moderate shift of 229 nm. On the lower end, we find the non-polar solvents CCl_4 and Toluene, causing shifts of 12 and 76 nm, respectively. Finally, Galden® HT 55, a perfluorinated low polarity fluid, results in a comparably small but measurable shift (4 nm, ×3 the spectral resolution).

The calculated effective diffusion coefficients reflect the wide range of different response kinetics evident in the OSCs, with the largest (Galden® HT 55 at 4.05×10^{-8} cm^2 min^{-1}) and slowest (HFB at 3.08×10^{-12} cm^2 min^{-1}) responses varying by four orders of magnitude. The initial diffusion of NH$_3$-SOL, CCl$_4$ and water is relatively fast, with effective coefficients of 3.76×10^{-9}, 2.47×10^{-9} and 3.76×10^{-9} cm^2 min^{-1} respectively. On the slower end, I extracted effective diffusion coefficients of 6.23×10^{-10} for EtOH and 7.42×10^{-11} for toluene.

Table 3.1. Analyte physical properties, Hildebrand parameter and respective response metrics of FHPS

	P_v (kPa) [64, 65]	v (Å^3) [43]	δ_{tot} (MPa$^{1/2}$) [43, 66]	χ_{eff}^H	$\Delta\lambda_\infty$(nm)	D_{eff} (cm^2 min^{-1})
H$_2$O	3.2	29.9	47.8	4.28	268	2.07×10^{-9}
aq. NH$_3$ (28%)	NH$_3$: 59.0 H$_2$O: 2.2	34.6	27.4	0.133	270	3.76×10^{-9}
EtOH	5.7	97.2	26.5	0.23	312	6.23×10^{-10}
Galden® HT 55	30.0	335.2	13.0	8.79	4	4.05×10^{-8}
Toluene	2.9	177.4	18.2	1.89	76	7.42×10^{-11}
CCl$_4$	15.1	161.3	17.8	1.23	12	2.47×10^{-9}
HFB	11.4	192.4	16.9	1.98	229	3.08×10^{-12}

Inspecting the relationship between the chemical-physical properties of the analytes can help us to interpret the kinetics. Figure 3.5a compares the product of P_v and χ_{eff}^H (left axis, black dots) and the effective diffusion coefficient retrieved from the OSCs (right axis, red squares) for the analytes. We can see that there is close correlation between the trends in the two quantities, which none of these properties individually achieves. This implies that the response is affected by both the intercalating species and its initial concentration in the environment.

Regarding the spectral shift of binary mixtures, Fig. 3.5b shows that the shift measure for the second-order stopband as a function of the molar fraction of HFB (x_{HFB}) and of toluene (x_{Tol})

in the liquid (red triangles). In this case, each species is assumed to contribute to the spectral shift proportionally to its molar fraction in solution. To confirm this, the same figure also reports the spectral shift calculated through the weighted average those of pure analytes (respecting their molar fraction in the mixture), which are in full agreement with the experimental data. The spectral shift for mixtures follows a pattern akin to an optical Raoult's law, where the total shift is the sum of the individual partial shifts of components depending on their concentration. This is most probably allowed by the low interaction between the non-polar toluene and the perfluorinated HFB and indicates that the swelling effect of the two chemicals is cumulative.
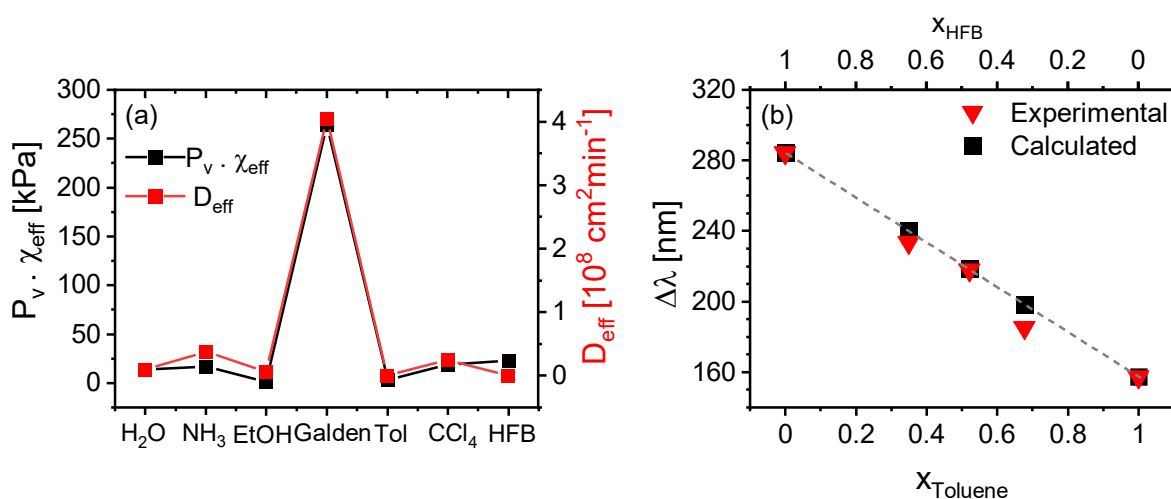
Figure 3.5. a) Comparison between the retrieved value of D_{eff} (red) and the product of effective Flory-Huggins parameter and P_v (black) retrieved from literature for investigated species. b) Measured and calculated stopband spectral shifts at the steady state for binary mixtures of toluene and HFB.

Considering the response of the system, with respect to both the intercalation kinetics and the spectral shift, I demonstrate the capability of these hybrid sensors to identify different chemicals in the gas phase, whether pure or in mixtures. These results strongly support the chances for novel disposable colorimetric sensors employable in different applications ranging from the detection of specific molecules in the environment to the quality control of food.

3. Conclusion

This chapter demonstrates a powerful colorimetric volatile organic compound sensing platform based on a simple two-component polymer DBR system with strong structural color. Alternating layers of Aquivion® and Poly(*N*-vinylcarbazole) interact with a wide range of analytes in a unique manner, providing the FHPSs with both sensitivity and selectivity. The combination of diffusion kinetics and spectral variations gives rise to a characteristic response to different chemical species that can be correlated to the Flory-Huggins parameter and vapor pressure, providing a fingerprint of the chemical analyte. This allows a broad sensitivity of the system with no need for dedicated labelling. The system is also promising in detecting mixtures of different volatile organic compounds and in determining their relative concentrations. As the sensing system is based on commercially available polymers, and its response can be measured through common spectrometers, it provides a refined single-use approach to chemical analysis and sensing that is convenient, accessible, portable, and adaptable to a wide range of applications. In order for this system to be more utilizable, further understanding of its kinetics, detection limits and cross sensitivity must be sought.

4. Materials and methods

Sample Preparation. The FHPS were cast by spin-coating using PVK (Carlo Erba, $M_w=$ 135000) as a high refractive index material and Aquivion® D79-25BS water dispersion (Solvay Specialty Polymers, $M_n = 130000$, $M_w = 250000$, acid loading = 1.26 $mmol_{SO_3H}/g_{polymer}$) as a low refractive index material. PVK was dissolved in toluene (30 mg/ml), and AQ dispersions (25% in water) in ethanol (AQ: EtOH 2:1 volume ratio). Next, 100 μL of the polymer solutions were cast at 190 rps sequentially. Afterwards, all samples were aged at 70 ̊C for 15 days to stabilize the optical response before being used as sensors. As the samples were prepared under the same conditions, they have identical structures as confirmed by the position of the PBGs.

Characterization. A custom setup based on optical fibers was used to measure the reflectance data of the FHPSs. Square samples of 3 × 3 mm sides were placed on scatterers in a reflectance dip probe (Avantes), 200-2500 nm (UV/vis/NIR) range, with core diameter 200 mm, (6 fibers for illumination, 1 fiber for collection). The incident light beam was impinged on the sample surface from DH-2000-BAL (Ocean Optics), deuterium and tungsten-halogen sources (spectral range 230-2500 nm). The probe was then immersed in a glass tube saturated with the indicated volume of target analyte. The reflected signal was relayed to AvaSpec-ULS4096CL-EVO detector (CMOS) (spectral range 200-1100 nm, resolution 1.3 nm) for collection and an Arcoptix FT-interferometer (900−2600 nm, resolution 8 cm^{-1}).[41, 55]

The FHPS optical response to vapor exposure was measured at 20 °C and 1 atm in a closed container where a 0.5 mL of liquid analytes (from Sigma-Aldrich and used without any further purification) was previously placed to saturate the environment. The partial pressure for the vapors in the given condition was calculated according to the literature.[64,65] Tracking the position of the photonic stop bands throughout the exposure process was done using a custom MATLAB code and used to construct optical sorption curves. The curves were used to calculate the initial diffusion coefficient according to a modification on Crank's solution to Fickian diffusion.[39, 58]

Spectral Modeling. The modeling of the FHPS reflectance spectrum was performed using a MATLAB homemade code based on the transfer matrix method as reported in previous works,[46] using the refractive index dispersion and actual thicknesses of the constituting polymer layers as inputs.

Refractive Index Measurement. Spectroscopic ellipsometry measurements were performed using a VASE instrument (J. A. Woollam Co, Lincoln, NE, USA) in the range 250–2500 nm at different incidence angles from 55° to 75° on films that were deposited on both quartz and

silicon standard substrates. A Varian Cary 6000i spectrometer in the spectral range of 200–1800 nm was used to measure both reflectance and transmittance at normal incidence. Subsequently, the complex refractive index was evaluated by the WVASE32® software (J. A. Woollam Co., Version 3.774) while adopting oscillator models that that guaranteed a Kramers–Kronig consistency.

5. References

(1) Watson, J. G.; et al. Review of volatile organic compound source apportionment by chemical mass balance. *Atmos. Environ.* **2001**, *35*, 1567-1584.

(2) Wang, Y.; et al. Microbial volatile organic compounds and their application in microorganism identification in foodstuff. *TrAC, Trends Anal. Chem.* **2016**, *78*, 1-16.

(3) Komilis, D. P.; et al. Emission of volatile organic compounds during composting of municipal solid wastes. *Water Res.* **2004**, *38*, 1707-1714.

(4) Phillips, M.; et al. Variation in volatile organic compounds in the breath of normal humans. *J. Chromatogr. B* **1999**, *729*, 75-88.

(5) Dudareva, N.; et al. Biosynthesis, function and metabolic engineering of plant volatile organic compounds. *New Phytol.* **2013**, *198*, 16-32.

(6) Khare, P.; et al. Asphalt-related emissions are a major missing nontraditional source of secondary organic aerosol precursors. *Sci. Adv.* **2020**, *6*, eabb9785.

(7) Sheu, R.; et al. Human transport of thirdhand tobacco smoke: A prominent source of hazardous air pollutants into indoor nonsmoking environments. *Sci. Adv.* **2020**, *6*, eaay4109.

(8) Stetter, J. R.; et al. Sensors, chemical sensors, electrochemical sensors, and ECS. *J. Electrochem. Soc.* **2003**, *150*, S11.

(9) Shankar, P.; Rayappan, J. B. B. Monomer: Design of ZnO nanostructures (nanobush and nanowire) and their room-temperature ethanol vapor sensing signatures. *ACS Appl. Mater. Interfaces* **2017**, *9*, 38135-38145.

(10) Hill, D.; Binions, R. Breath analysis for medical diagnosis. *Int. J. Smart Sens. Intell. Syst.* **2012**, *5*, 401–440.

(11) Lourenço, C.; Turner, C. Breath analysis in disease diagnosis: Methodological considerations and applications. *Metabolites* **2014**, *4*, 465-498.

(12) Sarigiannis, D. A.; et al. Exposure to major volatile organic compounds and carbonyls in

European indoor environments and associated health risk. *Environ. Int.* **2011**, *37*, 743-765.

(13) Lane, R. A.; Buckton, G. The novel combination of dynamic vapour sorption gravimetric analysis and near infra-red spectroscopy as a hyphenated technique. *Int. J. Pharm.* **2000**, *207*, 49-56.

(14) Santos, F. J.; Galceran, M. T. Modern developments in gas chromatography–mass spectrometry-based environmental analysis. *J. Chromatogr. A* **2003**, *1000*, 125-151.

(15) Han, J.-H.; et al. Photonic crystal lab-on-a-chip for detecting Staphylococcal Enterotoxin B at low attomolar concentration. *Anal. Chem.* **2013**, *85*, 3104-3109.

(16) Mortensen, N. A.; et al. Liquid-infiltrated photonic crystals: enhanced light-matter interactions for lab-on-a-chip applications. *Microfluid. Nanofluid.* **2008**, *4*, 117-127.

(17) Choi, C.-G.; et al. Fabrication of polymer photonic crystal slabs using nanoimprint lithography. *Curr. Appl Phys.* **2006**, *6, Supplement 1*, e8-e11.

(18) Scott, R. W. J.; et al. Tin dioxide opals and inverted opals: Near-ideal microstructures for gas sensors. *Adv. Mater.* **2001**, *13*, 1468-1472.

(19) Kuo, C.-Y.; et al. Stop band shift based chemical sensing with three-dimensional opal and inverse opal structures. *Sensor Actuat. B-Chem.* **2007**, *124*, 452-458.

(20) Lova, P.; et al. Core–shell silica–rhodamine B nanosphere for synthetic opals: from fluorescence spectral redistribution to sensing. *RSC Adv.* **2020**, *10*, 14958-14964.

(21) Yang, H.; et al. A visual water vapor photonic crystal sensor with PVA/SiO2 opal structure. *Appl. Surf. Sci.* **2017**, *423*, 421-425.

(22) Zhang, Y.; et al. Polymer-infiltrated SiO2 inverse opal photonic crystals for colorimetrically selective detection of xylene vapors. *Sens. Actuators, B* **2019**, *291*, 67-73.

(23) Zhang, Y.; et al. Photonic sensing of organic solvents through geometric study of dynamic reflection spectrum. *Nat. Commun.* **2015**, *6*, 7510.

(24) Szendrei, K.; et al. Fluorescent humidity sensors based on photonic resonators. *Adv. Opt. Mater.* **2017**, *5*, 1700663.

(25) Calvo, M. E.; et al. Porous one dimensional photonic crystals: novel multifunctional materials for environmental and energy applications. *Energy Environ. Sci.* **2011**, *4*, 4800-4812.

(26) Ruminski, A. M.; et al. Internally referenced remote sensors for HF and Cl2 using reactive porous silicon photonic crystals. *Adv. Funct. Mater.* **2011**, *21*, 1511-1525.

(27) Georgiev, R.; et al. All niobia Bragg stacks for optical sensing of vapors. *Opt. Quantum Electron.* **2020**, *52*, 114.

(28) Bonifacio, L. D.; et al. Stacking the nanochemistry deck: Structural and compositional diversity in one-dimensional photonic crystals. *Adv. Mater.* **2009**, *21*, 1641-1646.

(29) Hinterholzinger, F. M.; et al. One-dimensional metal-organic framework photonic crystals used as platforms for vapor sorption. *J. Mater. Chem.* **2012**, *22*, 10356-10362.

(30) Lotsch, B. V.; Ozin, G. A. Clay Bragg stack optical sensors. *Adv. Mater.* **2008**, *20*, 4079-4084.

(31) Bonifacio, L. D.; et al. Photonic nose–sensor platform for water and food quality control. *Small* **2011**, *7*, 3153-3157.

(32) Zhang, W.; et al. Highly efficient perovskite solar cells with tunable structural color. *Nano Letters* **2015**, *15*, 1698-1702.

(33) Qiao, Y.; et al. One-dimensional photonic crystals prepared by self-assembly of brush block copolymers with broad PDI. *J. Mater. Sci.* **2018**, *53*, 16160-16168.

(34) Kimura, M.; et al. Tunable multilayer-film distributed-Bragg-reflector filter. *J. Appl. Phys.* **1979**, *50*, 1222-1225.

(35) Hou, L.; et al. All-organic flexible polymer microcavity light-emitting diodes using 3M reflective multilayer polymer mirrors. *Appl. Phys. Lett.* **2005**, *87*, 243504.

(36) Herrnsdorf, J.; et al. Flexible blue-emitting encapsulated organic semiconductor DFB laser. *Opt. Express* **2010**, *18*, 25535-25545.

(37) Lova, P.; et al. Strategies for dielectric contrast enhancement in 1D planar polymeric photonic crystals. *Appl. Sci.* **2020**, *10*, 4122.

(38) Flory, P. J. *Principles of polymer chemistry*; Cornell University Press, 1953.

(39) Lova, P.; et al. Flory–Huggins photonic sensors for the optical assessment of molecular diffusion coefficients in polymers. *ACS Appl. Mater. Interfaces* **2019**, *11*, 16872-16880.

(40) Manfredi, G.; et al. Cellulose ternary photonic crystal created by solution processing. *Cellulose* **2016**, *23*, 2853-2862.

(41) Lova, P.; et al. Label-free vapor selectivity in poly(p-phenylene oxide) photonic crystal sensors. *ACS Appl. Mater. Interfaces* **2016**, *8*, 31941-31950.

(42) Noro, A.; et al. Photonic block copolymer films swollen with an ionic liquid. *Macromolecules* **2014**, *47*, 4103-4109.

(43) Hansen, C. M. *Hansen Solubility Parameters: A User's Handbook*; CRC press, 2002.

(44) Andreoli, S.; et al. Superacid Aquivion® PFSA as an efficient catalyst for the gas phase dehydration of ethanol to ethylene in mild conditions. *Appl. Catal., A* **2020**, *597*, 117544.

(45) Cowie, J. M. G. *Polymers: Chemistry and Physics of Modern Materials.*; Chapman&Hall, 1991.

(46) Lova, P.; et al. Advances in functional solution processed planar one-dimensional photonic crystals. *Adv. Opt. Mater.* **2018**, *6*, 1800730-1800726.

(47) Fan, Y.; et al. Defects, solvent quality, and photonic response in lamellar block copolymer gels. *Macromolecules* **2014**, *47*, 1130-1136.

(48) Lim, H. S.; et al. Dynamic swelling of tunable full-color block copolymer photonic gels via counterion exchange. *ACS Nano* **2012**, *6*, 8933-8939.

(49) Bao, X. Y.; et al. Heteroepitaxial growth of vertical GaAs nanowires on Si (111) substrates by metal-organic chemical vapor deposition. *Nano Letters* **2008**, *8*, 3755-3760.

(50) Gao, S.; et al. Time-resolved analysis of dielectric mirrors for vapor sensing. *ACS Appl. Mater. Interfaces* **2018**, *10*, 36398-36406.

(51) Giusto, P.; et al. Colorimetric detection of perfluorinated compounds by all-polymer photonic transducers. *ACS Omega* **2018**, *3*, 7517-7522.

(52) Convertino, A.; et al. A new approach to organic solvent detection: High-reflectivity bragg reflectors based on a gold nanoparticle/teflon-like composite material. *Adv. Mater.* **2003**, *15*, 1103-1105.

(53) Dincer, C.; et al. Disposable sensors in diagnostics, food, and environmental monitoring. *Adv. Mater.* **2019**, *31*, 1806739.

(54) Wang, Y.; et al. Electrode-free nanopore sensing by DiffusiOptoPhysiology. *Sci. Adv.* **2019**, *5*, eaar3309.

(55) Lova, P.; et al. Polymer distributed bragg reflectors for vapor sensing. *ACS Photonics* **2015**, *2*, 537-543.

(56) Mönch, W.; et al. Tunable Bragg filters based on polymer swelling. *Appl. Opt.* **2006**, *45*, 4284-4290.

(57) Lova, P.; et al. All-polymer photonic microcavities doped with perylene bisimide j-aggregates. *Adv. Opt. Mater.* **2017**, *5*, 1700523.

(58) Lova, P.; et al. Thin polymer films: simple optical determination of molecular diffusion coefficients. *ACS Appl. Polym. Mater.* **2020**, *2*, 563-568.

(59) Saleh, B. E.; Teich, M. C. *Fundamentals of Photonics*; John Wiley & Sons, 2019.

(60) Fieldson, G.; Barbari, T. The use of FTi. r.-atr spectroscopy to characterize penetrant diffusion in polymers. *Polymer* **1993**, *34*, 1146-1153.

(61) Colodrero, S.; et al. Response of nanoparticle-based one-dimensional photonic crystals to ambient vapor pressure. *Langmuir* **2008** *24*, 9135–9139.

(62) Chen, S. G.; et al. Effects of temperature and vapor pressure on the gas sensing behavior of carbon black filled polyurethane composites. *Sens. Actuators, B* **2005**, *105*, 187-193.

(63) Miller-Chou, B. A.; Koenig, J. L. A review of polymer dissolution. *Prog. Polym. Sci.* **2003**, *28*, 1223-1270.

(64) Yaws, C. L. *The Yaws Handbook of Vapor Pressure: Antoine Coefficients*; Gulf Professional Publishing, 2015.

(65) Perman, E. P. CXV.—Vapour pressure of aqueous ammonia solution. Part II. *J. Chem. Soc., Trans.* **1903**, *83*, 1168-1184.

(66) Nakamura, D.; et al. Nontoxic organic solvents identified using an a priori approach with Hansen solubility parameters. *Chem. Commun.* **2017**, *53*, 4096-4099.

Chapter 4: Fluorescent Multi-layered Films for Detecting Volatile Organic Compounds
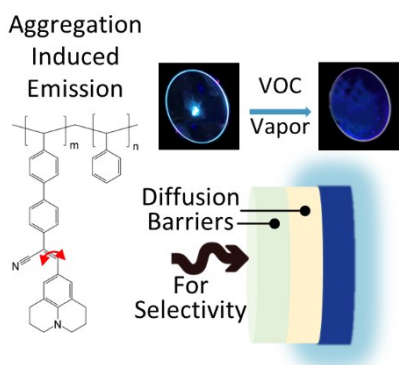
Abstract

Fluorescent sensors that provide an optically readable response have been an extensive topic of research due to their wide range of applications. Molecules demonstrating fluorescence driven by aggregation-induced emission have eliminated the common problem of fluorescence quenching in the solid state. Their portability, ease of interpretation, and independence from external power sources, therefore, make them excellent candidates for vapor sensing applications. When cast in thin films and exposed to vapors, their fluorescence changes in intensity or spectral shape as the microviscosity of their environment decreases. This is due to the change in the radiative and non-radiative relaxation pathways available for the electronic excited states of the molecule. However, variation in fluorescence can be similar for different analytes, making them hardly suitable as selective transducers. I report on the modification of analytes diffusivity based on the Flory-Huggins solution theory previously described, employing cellulose acetate and poly(vinyl alcohol) polymers as capping layers for the sensitive yet unselective fluorescent sensor. This approach allows distinguishing different polar and non-polar analytes without modifying the sensor molecular design.

This chapter is partially reproduced from:

1. Introduction

Human exposure to volatile organic compounds is a known cause of health complications,[1] that makes their detection essential, whether in industrial or urban settings.[2] Unfortunately, current widely employed quantitative analysis is cumbersome, complicated, and cannot be used by untrained personnel.[3-5] As such, simple and fast sensors are needed for environmental and industrial monitoring. In this context, fluorescent molecules have long been a reliable means of chemical sensing,[6] also widely used in the fields of biology and tissue imaging.[7] However, their utility has been often limited to use in solution because of fluorescence quenching in the solid state driven by several mechanisms.[8, 9] The discovery of fluorophores exhibiting an enhanced quantum yield in the solid state or in aggregates[10] has presented a paradigm shift for applications including light emitting devices,[11] smart responsive materials, and sensing.[12] These fluorophores exhibit an aggregation-induced emission (AIE) where the luminogens are referred to as AIEgens, as a direct opposite to the aforementioned aggregation induced quenching phenomenon.[13] Multiple mechanisms of fluorescence enhancement exist for AIEgens, including J-aggregate formation, twisted intramolecular charge transfer, excited-state intramolecular proton transfer, and restriction of intramolecular motion.[12] For the latter, the immobilization of the AIEgens in the solid state or in aggregates blocks the non-radiative vibrational and rotational relaxation pathways, which are well-known competitors for radiative relaxation.[14] Fluorescent molecular rotors (FMRs) are a common example of AIEgens, which found use as viscosity probes.[15] This typology of AIEgens are molecules with chromophore units linked with flexible bonds, which are free to rotate in solution, and whose rotation is restricted in aggregates, in the solid state and even in viscous media, causing radiative relaxation and high fluorescence quantum yield, as schematized in Fig. 4.1a. Thin films of polymers employing AIE have seen an increasing interest as vapor sensors.[16, 17] In fact, the integration of such AIEgens in polymers has been demonstrated as a viable way to make fluorescent thin film vapor sensors, where the change in the microviscosity due the solvent-induced plasticization of the polymer modulates the fluorescence intensity.[18] Equation 4.1 describes the relationship between the fluorescence quantum yield (ϕ) and the viscosity (η), where c is an experimental constant and y is the viscosity sensitivity of the FMR,[19] in typical Förster-Hoffmann behavior.[20] Since quantum yield variations are perceived as intensity variations, this provides a straightforward transduction signal where the fluorescence is expected to increase with increasing viscosity.

$$\log \phi = c + y \log \eta \tag{4.1}$$

Previously a copolymer of polystyrene and the AIEgen 2-[4-vinyl(1,1$0$-biphenyl)-4$0$-yl]-cyanovinyljulolidine (JCBF) showed fast quenching with different kinetics upon exposure to different volatile organic compounds.[21] JCBF should indeed act as a viscosity-sensitive AIEgen in the glassy polystyrene (PS) matrix, owing to the presence of the cyanovinyljulolidine moiety and the rotation around the julolidine–vinyl bond, as shown in the chemical structure of the copolymer P(STY-*co*-JCBF) in Fig. 4.1b, henceforth referred to simply as copolymer (CP). The copolymerization was proven to lead to faster quenching as compared to only dispersing JCBF in a PS matrix.[21] However, without chemical labelling, some analytes cause a similar response, which is a common limitation of dye-based systems.[22] This is especially relevant as the principal mechanism of sensing for the AIEgen in question is not chemical reaction, but rather the physical resistance to molecular rotation.
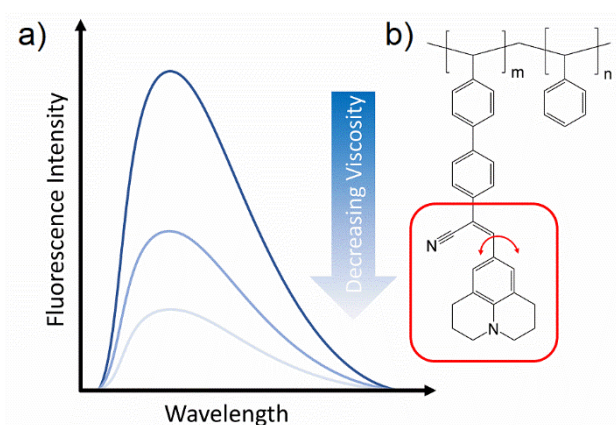
Figure 4.1. a) Fluorescence quenching of AIEgens in an environment of decreasing viscosity, b) structure of P(STY-*co*-JCBF) CP.

Multiple approaches have been implemented to increase the selectivity of optical readout sensors, including utilizing arrays of responsive films, and using multivariate analysis to identify the analytes.[23] Another is adding a capping layer that selectively influences the diffusion of possible vapors to the active medium. This approach has been demonstrated as a means of selectivity in sensors based on semiconducting polymers[24] as well as colorimetric solvent sensors.[22] Importantly, for sensors based on thin polymer films the interactions between the polymer and the analyte have been shown to rule the diffusion, and hence the response. I have previously shown that capping layers can have a significant influence on controlling the diffusion behavior in multilayered sensor films (see Chapter 2).[25] In this chapter, I report on

the absorption and fluorescence of thin CP films incorporating AIEgens as well as using polymer barrier layers to control the selectivity of AIE-based vapor sensors.

2. Materials and methods

Synthesis of P(STY-*co*-JCBF). P(STY-*co*-JCBF) was prepared and purified following a previously reported procedure.[21] After its synthesis and purification, the JCBF monomer was copolymerized with styrene through radical polymerization with azobisisobutyronitrile for one week to yield the random P(STY-*co*-JCBF) CP, with JCBF mole percent of 0.34%. For the copolymer provided by the group of Prof. Andrea Pucci at the University of Pisa, the JCBF feed weight percent for the copolymer is 0.98 the number average molecular weight of the CP is M_n =11,000 g/mol with a polydispersity of M_w/M_n=1.6, glass transition temperature T_g =102 °C and degradation temperature of T_d=420 °C.[21]

Thin Film Fabrication. The CP P(STY-*co*-JCBF) was dissolved in chloroform to obtain 5, 8, 10 and 20 mg/mL solutions. The solutions were spin-cast at 20 rps for 20 seconds on glass or fused silica substrates. Solutions of cellulose acetate (CA) and poly(vinyl alcohol) (PVA) of concentration 30 mg/mL in diacetone alcohol (4-Hydroxy-4-methylpentan-2-one) and water/ethanol respectively were cast through dynamic spin coating at 175 rps. All films were left to dry at room temperature for at least 24 hours before use. Films cast from CP solution with a concentration 8 mg/mL were used to fabricate samples, used as is, or capped with a layer of CA, PVA or both polymers. CA was treated with air-plasma before PVA deposition to improve the coverage and the homogeneity of the subsequent PVA film.

Absorbance Measurements. Absorbance measurements were performed using UV-1800 Spectrophotometer (Shimadzu, Kyoto, Japan) for both solutions and thin films.

Reflectance Measurements. Reflectance was recorded through a customized optical fiber-based setup consisting of deuterium and tungsten-halogen sources (Micropak, DH2000BAL, spectral range 230-2500 nm) employing reflectance from a UV-enhanced aluminum mirror (Thorlabs, PF10-03-F01) as a reference. The light was transmitted to and from the sample through an optical fiber (Avantes, FCR-7UVIR200-2-ME), and was detected through an AvaSpec-ULS4096CL-EVO spectrometer (CMOS, spectral range 200-1100 nm, resolution 1.4 nm).

Analytes. The tested analytes are chloroform (anhydrous, >99%, Sigma-Aldrich), dichloromethane (DCM, anhydrous, ethanol stabilized, SupraSolv, Supelco), toluene (ACS reagent, >99,5% Sigma-Aldrich), *m*-xylene (ReagentPlus, 99%, Sigma-Aldrich).

Photoluminescence Intensity Measurements. Glass-supported films were cut into approximately 1×0.7 cm^2 rectangles. Measurements of photoluminescence (PL) during vapor exposure were performed in a custom-built setup schematized in Fig. 4.2. The sample was placed inside a fused silica (Hellma QS macrocells) cuvette at 45° to avoid collecting edge-guided fluorescence signals. The optical fiber-based setup allowed the facile collection of the fluorescence signal during exposure to analyte vapors. Steady-state fluorescence variations were collected upon CW excitation with a 100 mW Oxxius 405 nm laser focused on a 1 mm^2 spot (as schematized in Fig. 4.2). The steady-state fluorescence signal was collected using the same spectrometer used for reflectance measurements. Long-pass optical filters (RazorEdge LP 442 RE and EdgeBasic LP 205 R, Semrock) were used for the collected fluorescence to eliminate the excitation laser signal. Vapor exposure was achieved through adding approximately 0.5 mL of the desired analyte to a glass pouch and allowing the closed pouch to be saturated with the vapor at room temperature. Afterwards, the bulb was fitted to the cuvette as shown in Fig. 4.2 and the fluorescence was recorded each second for 20 minutes.
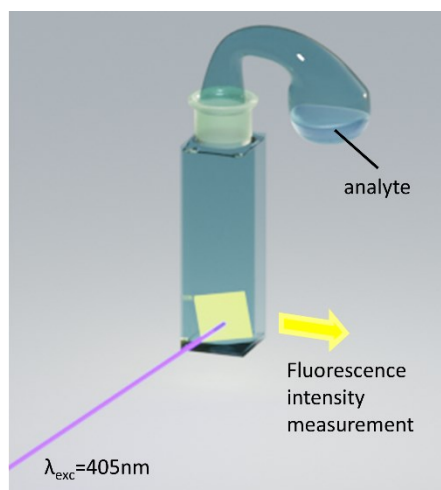

Figure 4.2. Schematic representation of experimental setup for fluorescence measurements during vapor exposure.

Thickness Measurements. Film thicknesses were determined through AFM measurements through the scratch method. The films were first scratched, and the profile was measured to determine the height of the polymer film. Measurements were performed in tapping mode using

Nanosurf CoreAFM microscope. Analyses of the scans were performed using the open-source software Gwyddion.[26]

3. Results and Discussion

Copolymer Absorbance and Fluorescence

Figure 4.3 compares the absorbance (black) and fluorescence (red) of the CP in solution (a) and as a thin film (b). The absorbance in chloroform solution in Fig. 4.3a shows a high absorbance in the UV for the CP with structured absorption band from approximately 250 to 320 nm, 335-377 nm and high absorbance peak at ~390 nm. On the other hand, the absorbance in the solid spin-cast films from solution (8 mg/ml) shows different features. Indeed, the absorbance peaks at around 260 nm but is otherwise broad and extends deeply to the visible spectral range. Furthermore, the fluorescence of the solution (Fig. 4.3a) has two distinct peaks at 507 and 528 nm, and two shoulders at around 592 and 622 nm. The fluorescence of the thin film (Fig. 4.3b) under the same 405 nm laser is blue-shifted and sharper, peaking approximately at 482 nm with a shoulder at around 559 nm.
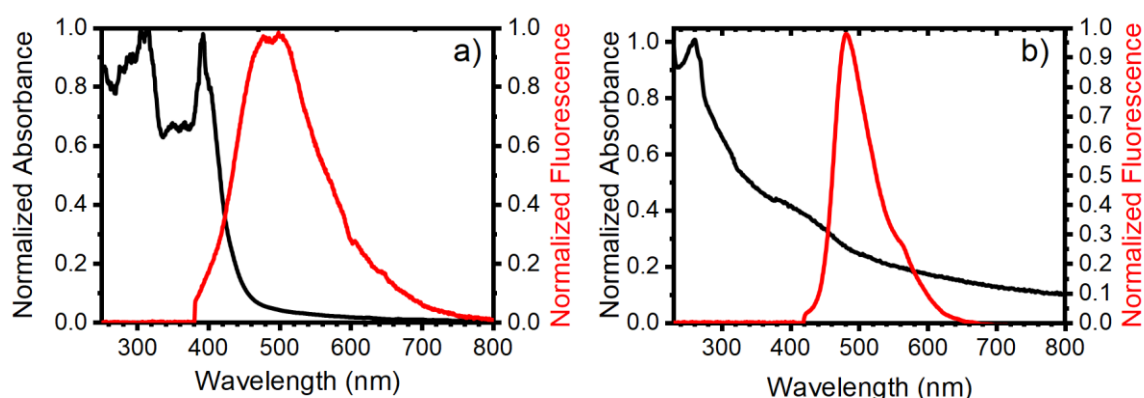
Figure 4.3. Normalized absorbance (black) and fluorescence (red) of P(STY-*co*-JCBF) a) in chloroform solution and b) in thin film on a fused-silica substrate.

Figure 4.4 shows the fluorescence intensity for films cast from solutions of different concentrations (panel a) and the fluorescence for a film cast from an 8 mg/mL CP/chloroform solution before and after drying for 24 hours (panel b). The fluorescence spectra for samples of different thickness have the same spectral features indicating a negligeable self-absorption. As expected, the intensity of fluorescence increases as the sample is left to dry under room conditions. Indeed, as chloroform is a good solvent for the CP, its slow evaporation locally

increases the local viscosity thus restricting intramolecular rotation of the FMR and the increasing the PL signal due to AIE.
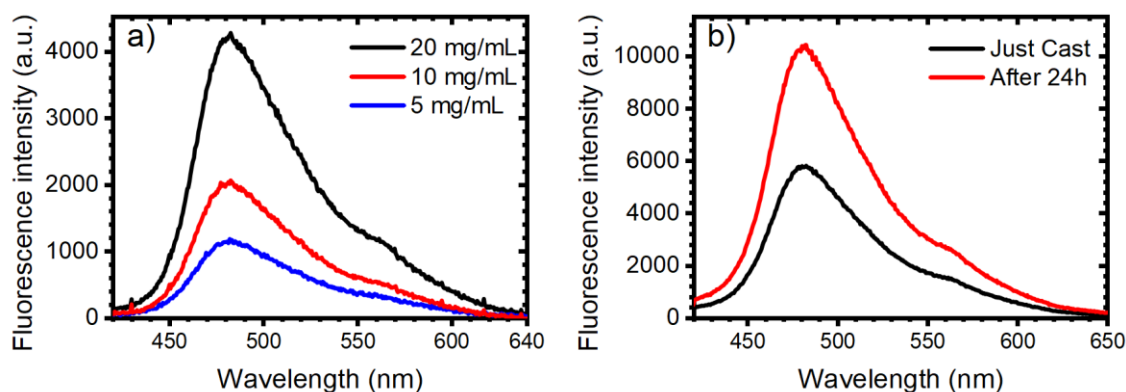
Figure 4.4. Fluorescence intensity of P(STY-*co*-JCBF) CP films of cast from different solution concentrations.

Fluorescence Quenching

The same principle applies when exposing thin films of the CP to different analytes. Figure 4.5 shows the fluorescence spectrum of the CP thin film on glass before exposure to any analytes (black line) and after one minute of exposure to vapors of *m*-xylene (red), toluene (blue), chloroform (green) and dichloromethane (DCM, orange) normalized to the initial intensity for a clear comparison. The spectra show that after one minute the florescence is already noticeably quenched for all the analytes, with quenching extent highest for exposure to DCM followed by chloroform, toluene and finally *m*-xylene. Also, minor variations in the peak PL wavelength are observed for all analytes. From Equation 4.1, the intensity is expected to decrease with decreasing viscosity, and thus with increasing concentration of vapor in the polymer film. As the vapor pressure of a liquid (P_v) is correlated to its concentration in a closed space, I examine the relationship between P_v (see Table 4.1) and the fluorescence quenching after one minute for our system. Indeed, the fastest quenching takes place on exposure to DCM (P_v=57.8 kPa), followed by chloroform (P_v=25 kPa), toluene (P_v=3.9) and the slowest being *m*-xylene (P_v=1.1 kPa).
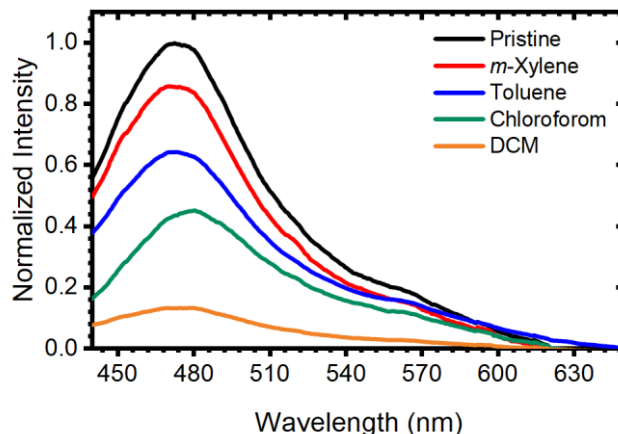
Figure 4.5. Fluorescence quenching: spectra collected for the unexposed film (black) and after exposure to vapors of chloroform, *m*-xylene, toluene and DCM for one minute.

Polymer-vapor Interactions

The specific polymer-solvent interactions, represented by the Flory-Huggins interaction parameter, χ of a polymer-solvent pair are also expected to influence the quenching kinetics. The parameter can be calculated as in Equation 4.2 (see Introduction and Chapter 3) using the molar volume of the analytes (V_M) and the squared difference between the Hildebrand solubility parameters for the components considered ($\Delta\delta^2$) (neglecting entropic contributions).[27] The latter represents the difference of density of cohesive energy between polymers and solvents such that higher solubility is represented by a smaller $\Delta\delta^2$. The values of the Hildebrand solubility parameters for both polymers and analytes as well as the molar volume of the latter have been retrieved from literature[27] and used to calculate χ for all the analyte-polymer pairs investigated.

$$\chi = V_M \frac{\Delta\delta^2}{RT} \qquad (4.2)$$

Table 4.1 reports the Flory-Huggins interaction parameter for all the analytes with PS, which is used as an approximate equivalent for the CP (due to the high mole percent of PS in the CP), and for two other polymers: PVA and CA used in the study. These polymers were chosen as their solvents do not interact strongly with the CP, allowing sequential spin-coating without damaging the fluorescent film (see materials and methods).

The quenching for CP (Fig. 4.5) indeed seems to be correlated to χ as it also follows a similar trend with higher quenching occurring for solvents with low χ. This means that the interaction

with DCM is the strongest and hence is expected to be the fastest, and the trend continues for the other analytes, with the slowest being *m*-xylene.

On the other hand, lower and more diverse solubilities were retrieved for the three molecules with respect to PVA and CA.[27] As such, the two polymers are anticipated to slow the diffusion speed of the non-polar toluene and *m*-xylene with respect to chloroform and dichloromethane. Therefore, simply employing one or both these materials as capping layers can in principle rule the diffusion kinetics of the analytes to the sensitive CP film, thus making the response to the different analytes more distinguishable, achieving higher selectivity. Layers of the CP of approximately 0.5 μm thickness were thus capped with PVA and CA films of roughly 0.5 and 1 μm, respectively. Three sets of samples were made, one of CP covered by a single layer of CA, one of CP covered by a layer of PVA and another of CP covered by CA then PVA in that order.

Table 4.1 Vapor pressure for all tested analytes, and Flory-Huggins interaction parameters for the used analyte-polymer pairs.

Solvent	P_v[28]	χ_{PS}	χ_{PVA}	χ_{CA}
m-xylene	1.1	1.14	3.71	4.64
Toluene	3.9	0.82	2.88	3.65
Chloroform	25.5	0.41	1.78	2.31
DCM	57.8	0.14	0.98	1.33

Quenching Dynamics

To get a more comprehensive view of the quenching during exposure, Fig. 4.6 shows the intensity of fluorescence at the peak emission wavelength of the tested films as a function of the exposure time. While the CP films are surely sensitive to all the analytes, it is rather complex to distinguish them one from the other by analyzing PL quenching. Indeed, after reaching equilibrium, the quenching values are rather similar for all the analytes (Fig. 4.6a), which is not suitable for specific warning systems.
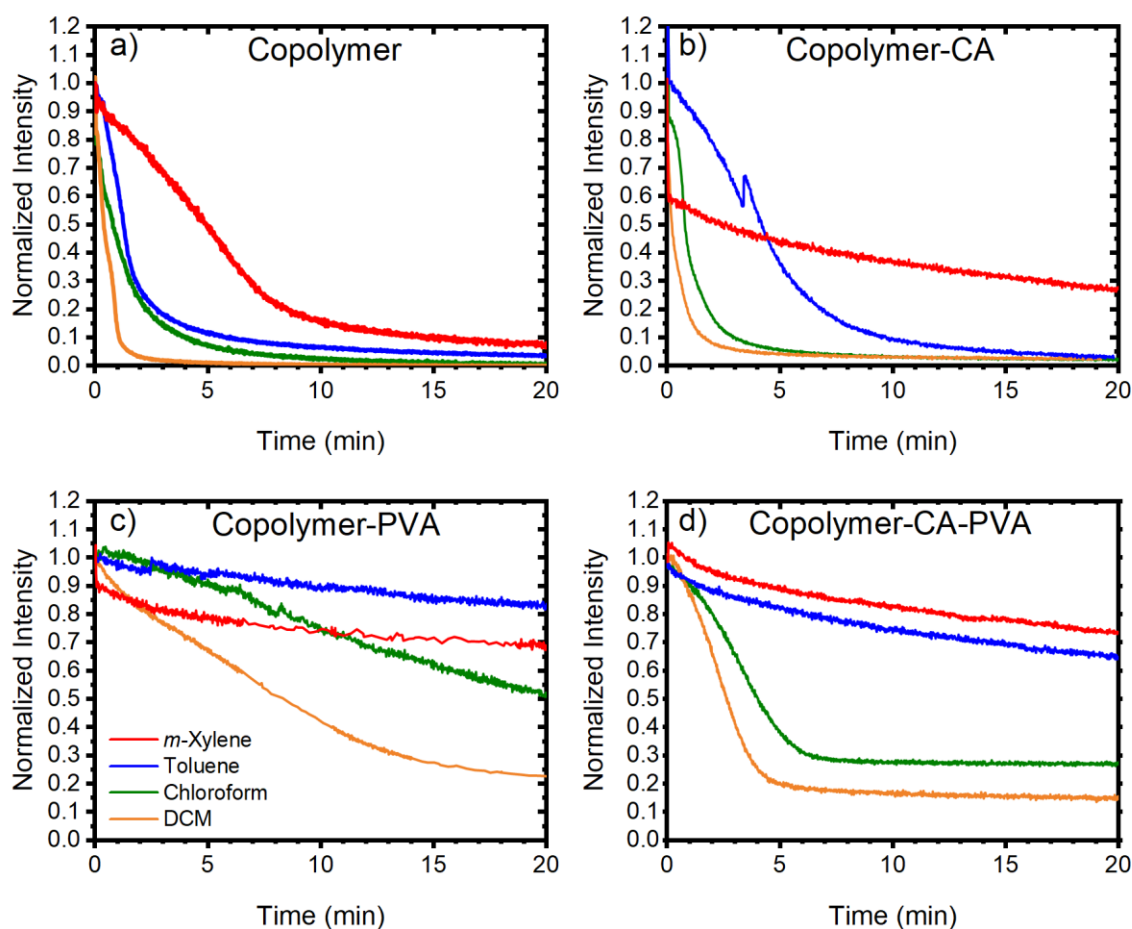
Figure 4.6. Fluorescence intensity quenching as a function of exposure time for: a) CP film, b) CP capped with CA, c) CP capped with PVA and d) CP capped with both CA and PVA on exposure to *m*-xylene (red), toluene (blue), chloroform (green) and DCM (orange).

Further examination of the quenching kinetics in all the investigated systems is expected to reveal more information about the diffusion of the analytes in the films, and hence the fluorescence quenching. First, it is notable that there are different regimes of distinct quenching kinetics during the exposure for several of the film-analyte pairs. For example, for the exposure of the CP film to DCM and chloroform, both chlorinated compounds, causes a fast quenching in the first minute followed by a slower regime. In the case of exposure to toluene, the quenching instead is at first slow, then speeds up after around 36 seconds and then slows down again for exposure longer than 100 s. Unexpectedly, the additional CA film on top of the CP causes an initial increase in the quenching rate on exposure to *m*-xylene with respect to the pristine copolymer, and then, in a clear 2-step mechanism, the quenching slows down to a

steady rate. For both toluene and chloroform the quenching rates decrease, and a sharp increase in intensity occurs after around 4 seconds for both, returns to normal, then occurs again around 200 seconds. As for the DCM, no significant change is noted. Conversely, as shown in Fig. 4.7c, the CP film capped with PVA displays a significant change in the quenching kinetics, not only slowing down for all analytes but also becoming more linear. This might be due to the polar nature of PVA films. Finally, for films composed of three layers, besides slowing the diffusion and quenching, the intensity reached a plateau for the chlorinated analytes chloroform and DCM, allowing their easy optical distinguishment with regards to *m*-xylene and toluene. Clearly, it is evident that for the same analyte the fluorescence quenching kinetics and extent are influenced strongly by the capping layers. The sudden changes in the intensity in the initial part of the exposure for CP and that capped with CA might be attributed to the occurrence of Langmuir diffusion first as a fast mechanism.[29] The following linear portion of the quenching is then assumed to be controlled by the diffusion related to the Flory-Huggins parameter.

While it is not possible to calculate the effective diffusion coefficient from the obtained data since not all systems reach an equilibrium, (see Chapters 2 and 3) the quenching rate $((\Delta I/I_0)/\Delta t)$ was extracted through fitting the linear part of the initial linear decay after the intensity increases or rapid drops, as reported in Fig. 4.7 for all the different film-analyte systems (black squares). It is worth noting that the scales for the rate imply very different quenching kinetics for the systems, with the slowest being the PVA-capped one.
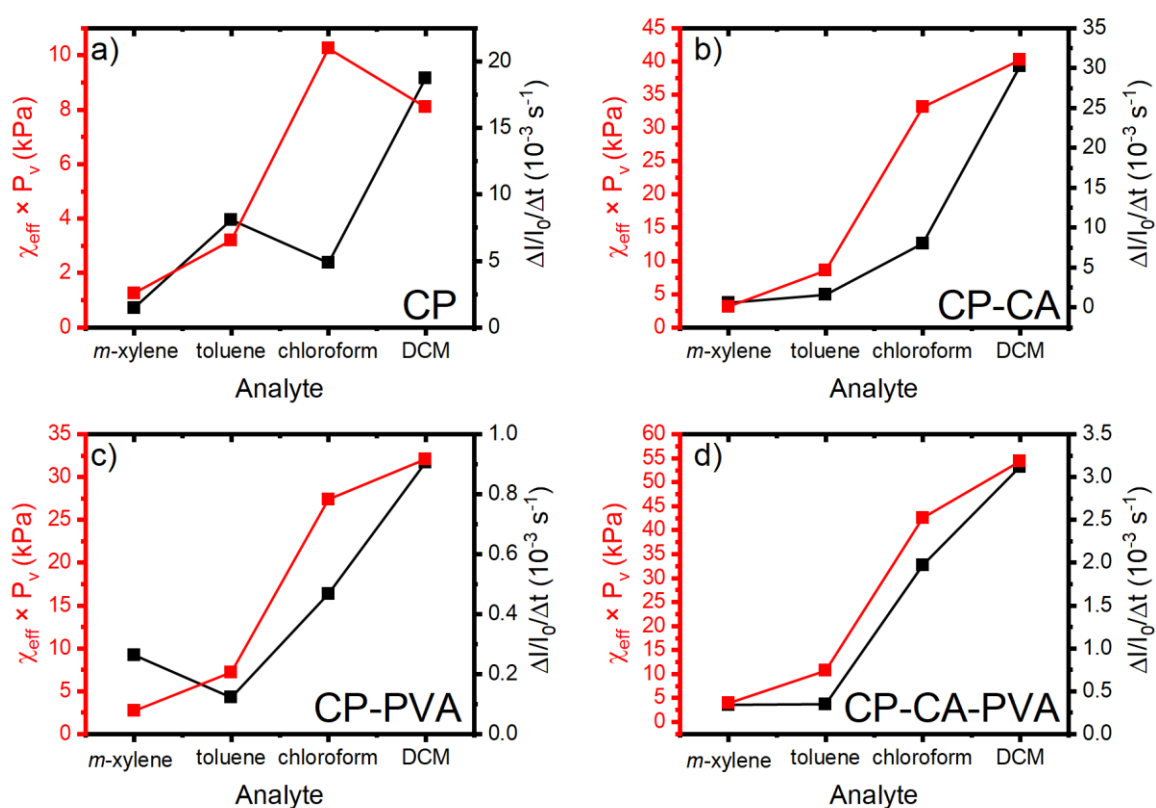
Figure 4.7. Quenching rate (black squares) and the product of the ceff and Pv for the a) CP, b) CP-CA, c) CP-PVA and d) CP-CA-PVA films on exposure to different analytes.

In addition, the effective Flory-Huggins parameter χ_{eff} (which the thickness-averaged χ for the polymers forming the multilayered films) was multiplied by P_v and the value is reported in red (see Chapter 3). While there seems to be a general trend for solvents with higher χ and higher P_v to cause a faster quenching, there are some clear exceptions, above all for CP exposed to chloroform. This might be due to the fact that the thicknesses and the polarity of the systems are not accounted for in the calculations. As discussed earlier, the quenching kinetics appear to be multi-staged and complex, thus needing further assessment and modeling. That can also be related to the presence of the interfaces in the multilayered thin film is expected to change the diffusion behavior, which makes more extensive analysis and modelling of the system. In fact, multiple interfering mechanisms including solvent accumulation at the barriers, diffusion acceleration at the layer interfaces could be at play (see Chapter 2). As such, more refined models are needed to understand the proposed systems that account for the diffusion, the molecular relaxation, solvent redistribution,[21] and the layer interfaces. Moreover, as the deep analysis of these data is still in progress, a possible analysis of the data in the framework of

time-temperature principle within the Williams-Landel-Ferry equation is currently being considered, as suggested in literature.[30]

Furthermore, the initial quenching rate extracted does not take into account the equilibrium quenching as mentioned earlier. To further examine the long-term quenching, I extract the extent of fluorescence quenching for all four films after exposure of 20 minutes to the vapor, reported in Fig. 4.8.
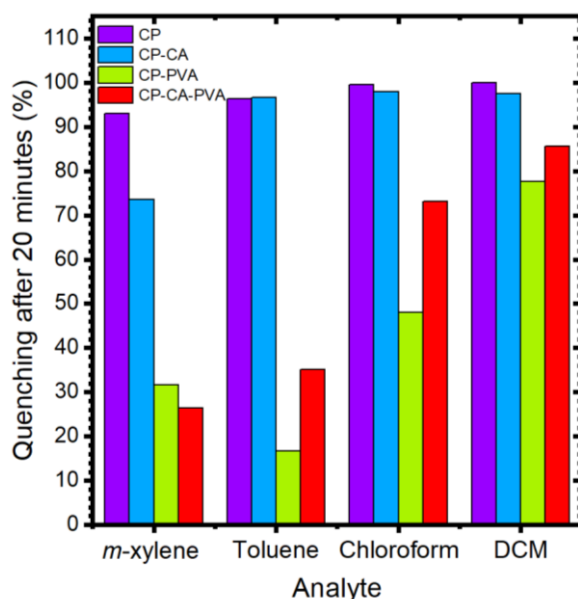
Figure 4.8. Quenching extent for fluorescent films after exposure to different analytes after 20 minutes.

For CP different analytes lead to very similar long-term quenching to less than 10% of the initial signal, which means it is difficult to distinguish the different analytes through intensity observation alone. However, the introduction of the capping layers changes that. For example, using the CA capping layer, the quenching of the *m*-xylene is delayed, which established a mechanism to differentiate between the aromatic hydrocarbons *m*-xylene and toluene. The polar PVA layer on its own instead decreases the quenching for all analytes significantly. Finally, the use of 2 capping layers of different materials provides distinct intensity difference between the chlorinated and aromatic compounds, making the use of multiple barrier layers a viable possibility for future developments in selective sensors.

The inspection of the fluorescence quenching gives an insight of the diffusion-ruled long-time response. However, to provide an insight of the mechanisms affecting the relaxation of the

molecule, including the radiative and non-radiative pathways in the ns time regime time-resolved fluorescence decay measurements are needed. Data for the PL lifetime are being elaborated and are expected to give insight about the photophysics of CPs containing AIEgens, which is not well-understood in the literature. In addition, to disentangle the radiative and non-radiative decays, information about the quantum yield during the exposure is needed (see Chapters 5 and 6). In summary, the preliminary data reported in this chapter demonstrate that a random copolymer of polystyrene and the fluorescent AIEgen JCBF is a promising solid-state vapor sensor. I probe the kinetics of its molecular rotation and the influence of exposure to different volatile organic compounds on it. Most importantly, I demonstrate that simple capping layers of different polymers can be a versatile and simple tool for controlling the specificity of the response of the thin-film sensor without changing the used polymers. While preliminary, the results are promising for both sensing applications as well as investigations of diffusion kinetics.

4. References

(1) Guo, H.; et al. Risk assessment of exposure to volatile organic compounds in different indoor environments. *Environ. Res.* **2004**, *94*, 57-66.

(2) Wang, P.; Zhao, W. Assessment of ambient volatile organic compounds (vocs) near major roads in urban nanjing, china. *Atmos. Res.* **2008**, *89*, 289-297.

(3) Koziel, J. A.; Pawliszyn, J. Air Sampling and Analysis of Volatile Organic Compounds with Solid Phase Microextraction. *J. Air Waste Manage. Assoc.* **2001**, *51*, 173-184.

(4) Demeestere, K.; et al. Sample Preparation for the Analysis of Volatile Organic Compounds in Air and Water Matrices. *J. Chromatogr. A* **2007**, *1153*, 130-144.

(5) Ochiai, N.; et al. Long-Term Measurement of Volatile Organic Compounds in Ambient Air by Canister-based One-Week Sampling Method. *J. Environ. Monit.* **2003**, *5*, 997-1003.

(6) Demchenko, A. P. *Introduction to fluorescence sensing*; Springer Science & Business Media, 2008.

(7) Ueno, T.; Nagano, T. Fluorescent probes for sensing and imaging. *Nat. Methods* **2011**, *8*, 642-645.

(8) Winnik, F. M. Photophysics of preassociated pyrenes in aqueous polymer solutions and in other organized media. *Chem. Rev.* **1993**, *93*, 587-614.

(9) Jenekhe, S. A.; Osaheni, J. A. Excimers and exciplexes of conjugated polymers. *Science* **1994**, *265*, 765-768.

(10) Luo, J.; et al. Aggregation-induced emission of 1-methyl-1,2,3,4,5-pentaphenylsilole. *Chem. Commun.* **2001**, 1740-1741.

(11) Du, X.; et al. Efficient Non-doped Near Infrared Organic Light-Emitting Devices Based on Fluorophores with Aggregation-Induced Emission Enhancement. *Chem. Mater.* **2012**, *24*, 2178-2185.

(12) Mei, J.; et al. Aggregation-Induced Emission: The Whole Is More Brilliant than the Parts. *Adv. Mater.* **2014**, *26*, 5429-5479.

(13) Zhao, Z.; et al. Aggregation-Induced Emission: New Vistas at the Aggregate Level. *Angew. Chem. Int. Ed.* **2020**, *59*, 9888-9907.

(14) Klessinger, M.; Michl, J. *Excited States and Photochemistry of Organic Molecules*; VCH, 1995.

(15) Lee, S.-C.; et al. Fluorescent Molecular Rotors for Viscosity Sensors. *Chem. - Eur. J.* **2018**, *24*, 13706-13718.

(16) Ding, Y.; et al. Which is a better fluorescent sensor: aggregation-induced emission-based nanofibers or thin-coating films? *Mater. Adv.* **2020**, *1*, 574-578.

(17) Campbell, I. A.; Turnbull, G. A. A kinetic model of thin-film fluorescent sensors for strategies to enhance chemical selectivity. *Phys. Chem. Chem. Phys.* **2021**, *23*, 10791-10798.

(18) Ahmad, M.; et al. Highly selective vapochromic fluorescence of polycarbonate films Doped with an ICT-Based solvatochromic probe. *J. Polym. Sci., Part B: Polym. Phys.* **2017**, *55*, 1171-1180.

(19) Förster, T.; Hoffmann, G. Die Viskositätsabhängigkeit der Fluoreszenzquantenausbeuten einiger Farbstoffsysteme. *Z. Phys. Chem.* **1971**, *75*, 63-76.

(20) Haidekker, M. A.; Theodorakis, E. A. Environment-sensitive behavior of fluorescent molecular rotors. *J. Biol. Eng.* **2010**, *4*, 11.

(21) Borelli, M.; et al. Fluorescent polystyrene films for the detection of volatile organic compounds using the twisted intramolecular charge transfer mechanism. *Molecules* **2017**, *22*, 1306.

(22) Lee, J.; et al. A protective layer approach to solvatochromic sensors. *Nat. Commun.* **2013**, *4*, 2461.

(23) Askim, J. R.; et al. Optical sensor arrays for chemical sensing: the optoelectronic nose. *Chem. Soc. Rev.* **2013**, *42*, 8649-8682.

(24) Ullman, A. M.; et al. Hybrid Polymer/Metal–Organic Framework Films for Colorimetric

Water Sensing over a Wide Concentration Range. *ACS Appl. Mater. Interfaces* **2018**, *10*, 24201-24208.

(25) Megahd, H.; et al. Universal Design Rules for Flory–Huggins Polymer Photonic Vapor Sensors. *Adv. Funct. Mater.* **2021**, *31*, 2009626.

(26) Nečas, D.; Klapetek, P. Gwyddion: an open-source software for SPM data analysis. *Open Phys.* **2012**, *10*, 181-188.

(27) Hansen, C. M. *Hansen solubility parameters: a user's handbook*; CRC press, 2002.

(28) Haynes, W. M.; et al. *CRC Handbook of Chemistry and Physics*; CRC Press, 2007.

(29) Chalykh, A. E.; et al. Free Volume and Water Sorption by Cellulose Esters. *Polymers (Basel)* **2021**, *13*.

(30) Cowie, J. M. G.; Arrighi, V. *Polymers: chemistry and physics of modern materials*; CRC press, 2007.

Chapter 5: "Purcell effect" in All-polymer Planar Microcavities
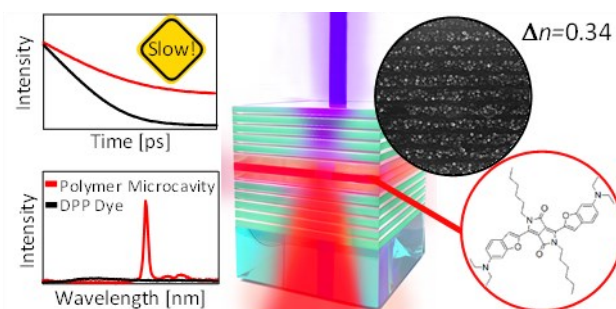
Abstract

Controlling the radiative rate of emitters with macromolecular photonic structures opens the future development of flexible devices with enhanced performances that are easy to scale up. For instance, radiative rate enhancement empowers low-threshold lasers, while rate suppression affects the recombination in photovoltaic and photochemical processes. However, claims of Purcell effect with polymer structures are controversial as the low dielectric contrast typical of suitable polymers is commonly not enough to provide the necessary confinement. Here I show all-polymer planar microcavities with photonic band gaps tuned to the photoluminescence of a diketopyrrolopyrrole-derivative allowing a change in its fluorescence lifetime. Radiative and non-radiative rates were disentangled systematically through measurements of the external quantum efficiencies, comparing the planar microcavities with a series of reference designed to exclude any extrinsic effects. This analysis shows unambiguously dye radiative emission rate variations obtained with macromolecular dielectric mirrors assigned to the Purcell effect. This was possible through exploiting photonic structures made of poly(N-vinylcarbazole) as a high-index material and the perfluorinated Aquivion® as a low-index one, which display the largest dielectric contrast ever obtained in planar polymer cavities. Current limits and requirements to achieve full control of radiative rates with polymer planar microcavities are also addressed.

This chapter is partially reproduced from:

1. Introduction

Interest in the field of polymer photonics has quickly accelerated in the last decades, owing to their unique properties, including easy chemical tailoring, mechanical flexibility and simple fabrication.[1] Devices employing all-polymer planar one-dimensional photonic crystals such as light emitting diodes (LEDs), photovoltaic cells, and sensors[2] are especially appealing as their fabrication is easy to scale up.[3] However, the poor refractive index (n) contrast between transparent polymer materials limits light confinement[3] and hinders the control of spontaneous emission rates, namely the Purcell effect.[4] However, empowering control of emitters radiative rate with polymer photonic crystals promises easy large area fabrication of both flexible low threshold lasers[5] and high-efficiency LEDs[6,7] when the rate is increased, and photovoltaic photocatalytic devices where an increase in exciton lifetime (i.e. a reduction of the radiative rate) leads to a longer diffusion length and higher device performance.[8]

Both radiative rate enhancement and suppression have been well-demonstrated in metallic[9] and inorganic[10] structures. Indeed, the latter have been dominating the photonics playground thanks to their low losses and optimal radiation confinement.[11] Rate control has been achieved employing inorganic optical resonators[12] and microcavities (MCs) of different typologies[13] including planar ones[14], microdisks,[15] micropillars,[16] and photonic crystals.[17] On the other hand, their fabrication requires severe conditions, and it is time and energy consuming. This aspect has hindered their adaptation for flexible devices, integration with organic and hybrid emitters, and large-area production. As such, achieving rate control with polymer structures would be a milestone for efficient solution-processable flexible photonics. Yet, the unambiguous observation of this effect in polymer structures has been disputed within the scientific community. Some claims of Purcell effect observation were made for hybrid silica/polystyrene systems,[18, 19] but possible extrinsic effects such that of changes in refractive index of the effective medium,[20] or chemical effects, including exciton chemical traps, impurities, and local disorder affecting the structure have been debated for these systems.[21-24]

In general, photoluminescence (PL) lifetime (τ_{PL}) variation was reported for polymer synthetic opals,[25] 2D[26] and planar MCs,[27, 28] but radiative rate variations were not investigated. Indeed, τ_{PL} measurements alone cannot disentangle radiative (Γ_R) and non-radiative decay rates (Γ_{NR}) without information on the photoluminescence external quantum efficiency (ϕ, Equation 5.1).[29] Then, the conclusion that any changes in fluorescence lifetime arise from a modification of Γ_R value is valid only when ϕ is taken into account.

$$\phi = \frac{\Gamma_R}{\Gamma_R + \Gamma_{NR}} \qquad (5.1)$$

I unambiguously demonstrate radiative rate suppression within a planar polymer MC fabricated through solution-processing of a perfluorinated polymer, Aquivion® (AQ, n=1.35)[2] and poly(N-vinylcarbazole) (PVK, n=1.69).[3,30] The couple provides the highest dielectric contrast used for polymer planar microcavities (Δn=0.34 in the UV-NIR range) so far.[31] The dye embedded in the cavity is a diketopyrrolopyrrole derivative (DPP), which are some of the most studied organic dyes for electronics and photonics,[32] including in organic light-emitting diodes and solar cells[33] due to their tailorable synthesis and high thermal- and photostability.[34] The same materials were also employed to fabricate a series of references. A systematic assessment of ϕ and emission decays allows to unequivocally demonstrate an increase of radiative lifetime (τ_{rad}) in microcavities opportunely tuned, ruling out any simpler alternative interpretations or extrinsic photophysical processes beside cavity Purcell effects.

2. Results

Cavity Design and Properties

The MCs were grown via spin-coating deposition and are formed by two dielectric mirrors, each consisting of 20 bilayers of AQ and PVK. The cavity between the mirrors contains two layers of cellulose acetate (CA) sandwiching a layer of polystyrene (PS) doped with a DPP derivative[33, 35] (DPP:PS), as sketched in Fig. 5.1a. The same panel shows the chemical structure of the DPP dye, while the normalized PL and absorbance spectra of a thin film of the DPP:PS blend cast on a glass substrate are reported in Fig. 5.1b. In the spectral range of interest, the DPP dye shows three distinct absorption maxima at λ=450, 600 and 655 nm (highest intensity). The steady state PL spectrum of the blend, upon excitation at 534 nm, displays a Stokes shift of 22 nm, as the maximum intensity appears at λ=677 nm with a full width at half maximum (FWHM) of 40 nm. Additionally, the emission shows a broad shoulder at 745 nm.
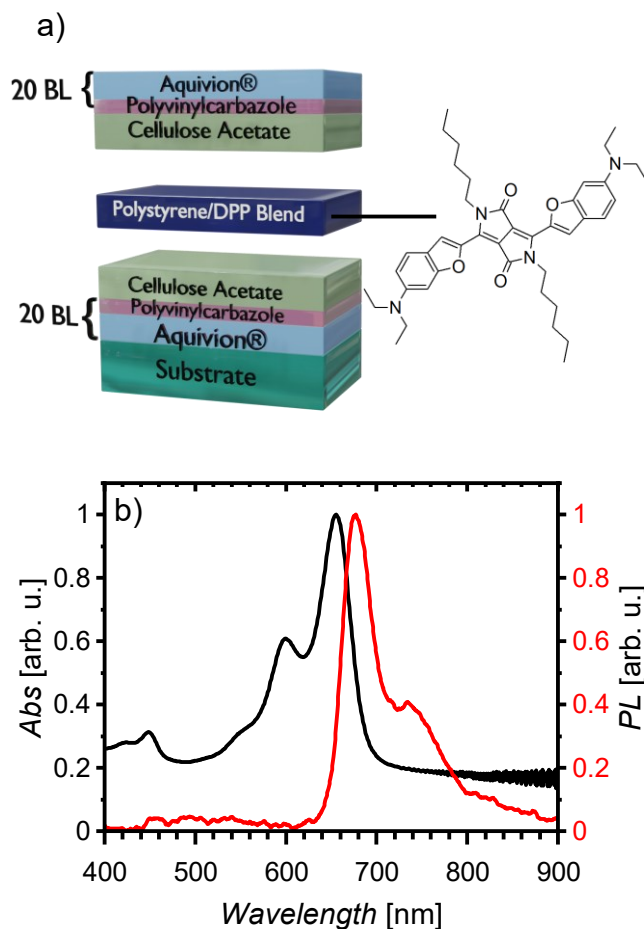
Figure 5.**1.** a), Schematic of the MC structure, including the chemical structure of the DPP dye. b) Normalized absorbance, and PL intensity spectra of a DPP:PS blend thin film.

The microcavity (MC$_{tuned}$) was engineered to tune the mirrors' photonic band gap (PBG) and cavity mode to the PL of the DPP dye by simple control of the spin-coating deposition parameters. Moreover, several reference samples were fabricated to compare the properties of the microcavity with those of the bare dye. In particular, to exclude radiative rate variations due to extrinsic effects including medium chemical effects, polarity of the medium and residual solvent diffusion among layers, waveguiding, as well as out-coupling and light extraction differences.[31] These references were: a DPP:PS pristine blend film, a detuned microcavity (MC$_{detuned}$) with the PBG in the green region of the spectrum where the DPP:PS does not show significant fluorescence, a bilayer CA-DPP:PS (R1), and a five-layer structure (R2) mimicking the central part of the cavity (PVK-CA-DPP:PS-CA-PVK). These references serve to simulate possible defects that could be unintentionally inserted into the microcavity by the growth

process, as well as loss mechanisms such as waveguiding effects and self-absorption, which are known to affect light emission in polymer microcavities.[30]

Figure 5.2a contrasts the reflectance spectra of both the tuned and detuned microcavities. Both structures display the characteristic features of planar MCs: an intense reflectance band corresponding to the PBG of the photonic crystal mirror, with a sharp minimum assigned to the cavity mode and a Fabry–Pérot interference pattern in the background. While the PBG and cavity mode of MC_{tuned} strongly overlap the emission spectrum of the DPP blend, the shifted microcavity provides no spectral overlap, hence any variation in the emission of the dye in this sample cannot be assigned to optical confinement effects provided by the microstructure.

Figure 5.2. a) Reflectance spectra of tuned microcavity (red line) and the detuned one (blue line). b) Experimental (red full line) and simulated (black dotted line) transmittance of tuned microcavity. c) SEM image of th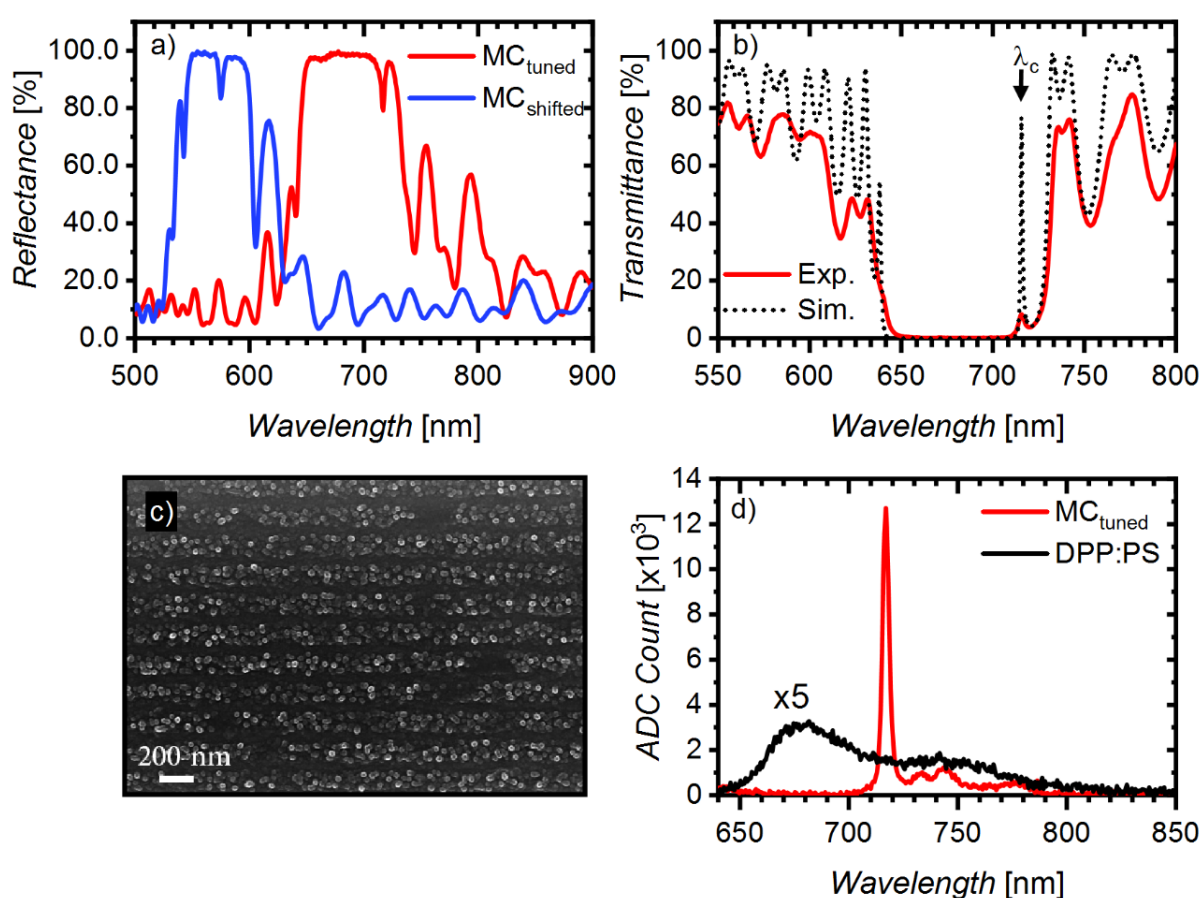e cross-section of a representative DBR forming the dielectric mirror in a tuned microcavity. d) Photoluminescence of DPP:PS film (multiplied by 5, black full line) and tuned microcavity (red full line).

For further characterization of the MC_{tuned}, Fig. 5.2b shows the transmittance spectrum of the microcavity which, corresponding to the reflectance spectrum, shows a wide PBG with a maximum at λ_C=717 nm assigned to the cavity mode. The PBG extends from 635 to 732 nm (FWHM of 250 meV), a larger value compared to other polymer planar microcavities with smaller dielectric contrast.[31, 36] Moreover, due to the photonic-band structure of the MC, the spectral position of the aforementioned features is strongly dependent on the angle of incidence and the polarization state of the incoming light beam,[37] allowing possible tuning of the emitted spectrum by changing the detection angle. It is worth noticing that the sample surface shows some minor spectral inhomogeneities due to small thickness variations across the area.

The optical response of the structure was simulated using the complex refractive index dispersion of all the polymers employed already reported in literature[2, 3, 30, 38] and that measured for the DPP:PS film. Employing transfer matrix method (TMM) modelling,[3] the simulated transmittance reported in Fig. 5.2a (dotted line) is best fitted to the experimental one, retrieving the thicknesses of individual materials (74.5 nm for PVK, 159.5 nm for AQ, 184 for DPP:PS and 78 nm for the CA layers). The positions and widths of the interference fringes, as well as the PBG and λ_c in the experimental measurements are all well-reproduced in the calculation. To obtain initial estimates of the layer thicknesses for simulations, SEM measurements were performed. The SEM micrograph in Fig. 5.2c shows the layering of the DBR after freeze-cracking the microcavity, which caused uneven fracture artefacts in the image. The AQ layers are distinguishable thanks to their spherical aggregates, which have been previously reported in Chapter 3 for the perfluorosulfonic acid ionomer dispersions.[39] From the SEM images, a clear uniformity is observed and the average thickness of the AQ layers is estimated to be 108 ± 8 nm and that of PVK to be 65 ± 6 nm. The freeze-cracking process induces delamination that prevents direct observation of the cavity layers, whose thickness is then estimated through AFM measurements to be 88±33 nm for the CA and 113±67 for the DPP:PS layer. We observe a good agreement within the experimental uncertainty between thickness derived from SEM/AFM for PVK, CA, and DPP:PS layers and those derived from optical simulations, while some discrepancy is observed for AQ layers. However, this is expected as AQ, being a material sensitive to the chemical environment (see Chapter 2),[2] is strongly perturbated by the abrupt change induced by the freeze-cracking process and the subsequent vacuum environment of the SEM chamber.

Figure 5.2d compares the PL spectra for a DPP:PS thin film and MC_{tuned}. Both the DPP:PS layer in the microcavity and in the reference DPP:PS film were cast under identical conditions. Due to the spectral overlap of the dye's PL with the PBG and the very sharp cavity mode (FWHM ~3.5 nm), the local photonic density of states (LPDOS) strongly modulates the fluorescence line-shape.[3, 40] Indeed, the LPDOS is very low at the PBG and is strongly enhanced at the cavity mode, channeling the emission into the latter. At near-normal incidence the enhanced LPDOS at the cavity mode produces a 40-fold intensity enhancement of DPP emission at λ_C=717 nm as compared to the bare emitter film, a record value among polymer microcavities (the highest being ×8.9 to the best of our knowledge).[28] The finesse of MC_{tuned} is quantified through the quality factor ($Q = \lambda_C/\Delta\lambda_C$), that is approximately 205, a relatively high value compared to the highest reported so far for all-polymer microcavities (Q=255).[36] We also notice three additional weak emission peaks at approximately 733, 743 and 775 nm in the cavity PL corresponding to the local minima in the Fabry–Pérot interference pattern (Fig. 5.2a). Unsurprisingly, the PL is strongly suppressed at the PBG wavelengths where the LPDOS is lower.

Moreover, we consider the overall microcavity effect on the PL intensity, where only a part of the dye fluorescence spectrum overlaps the PBG and microcavity mode. Figure 5.3 shows PL intensity as a function of the collection angle for the MC_{tuned} (red) compared to the DPP:PS standalone film (black) and the R2 reference (blue). Panel a displays the spectrally integrated PL signal (over 600-800 nm spectral width), while panel b reports the intensity of the highest signal collected for the microcavity and the references (considering the spectral shift of the PBG mode to shorter wavelengths typical of planar MCs[40]). It is clear that in both cases the intensity of the signal collected for the tuned microcavity is higher than that of the references for all angles in the 0°-50° range. The intensity of the mode is almost constant until around 7 degrees and then decreases steadily for larger collection angles. As for the references, the maximum PL does not vary as strongly for higher collection angles. The fluorescence from MC_{tuned} is highly directional compared to the Lambertian emission of the DPP:PS film.
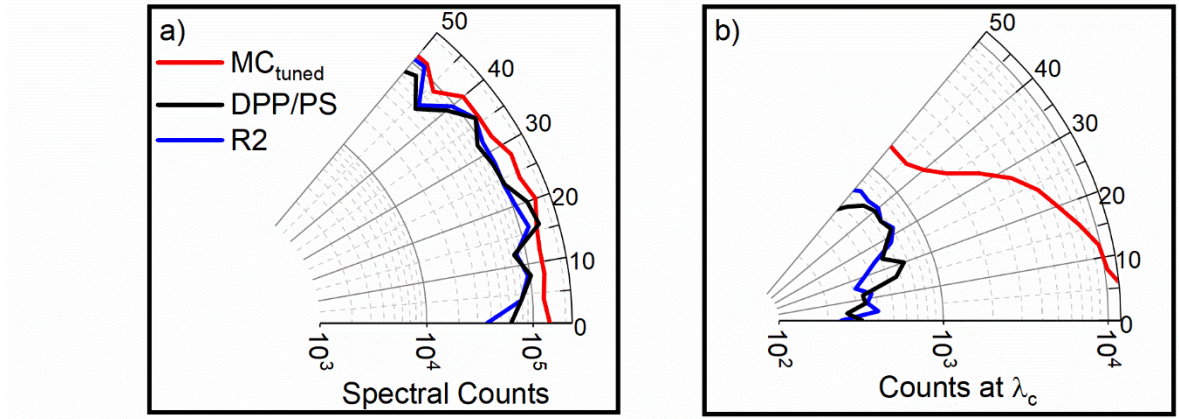
Figure 5.3. Photoluminescence Intensity Characterization. a) Angular resolved spectrally integrated photoluminescence intensity for the reference DPP:PS film (black), R2 (blue) and for the MC$_{tuned}$ (red). b) Intensity at cavity mode wavelength for MC$_{tuned}$ (red), DPP:PS film (black) and R2 (blue).

Then the total emission enhancement factor (G_{tot}^{exp}) according to Equation 5.2[41] can be calculated as ~1.4 with respect to the dye and ~1.3 with respect to R2, indicating an overall enhancement in the PL intensity. This however does not account for the different emission cones and differences in absorbance between the samples, which are better reflected in the quantum yield measurements in the next section.

$$G_{tot}^{exp} = \frac{\iint PL_{cav}((\lambda, \theta)d\lambda\,\mathrm{d}\theta}{\iint PL_{ref}((\lambda, \theta)d\lambda\,\mathrm{d}\theta} \quad (5.2)$$

Cavity Effects and Radiative Rate Modification

Figure 5.4 compares the fluorescence decay upon excitation with a pulsed laser (λ=405 nm) for the standalone DPP:PS film (black squares), MC$_{detuned}$ (blue squares) and MC$_{tuned}$ (red squares) evaluated from PL intensity at $\lambda_{Mctuned}\pm10$ nm. As the reference intensities are lower than the tuned microcavity due to the enhancement effect previously discussed (see Fig. 5.2d), their decay signal has lower signal to noise ratio. Notwithstanding, a strong difference between the lifetimes of MC$_{tuned}$ and the two references can clearly be observed, even without the need for a fitting. Single exponential fitting of the decays (data not shown for R1 and R2) allowed the retrieval of τ_{PL}, which is related to the radiative and non-radiative decays rates ($\frac{1}{\tau_{PL}} = \Gamma_R + \Gamma_{NR} = \frac{1}{\tau_R} + \frac{1}{\tau_{NR}}$). Then, the radiative lifetime for all the samples (τ_{rad}) was calculated as the ratio between best-fitted τ_{PL} and quantum yield ϕ measured for all samples.
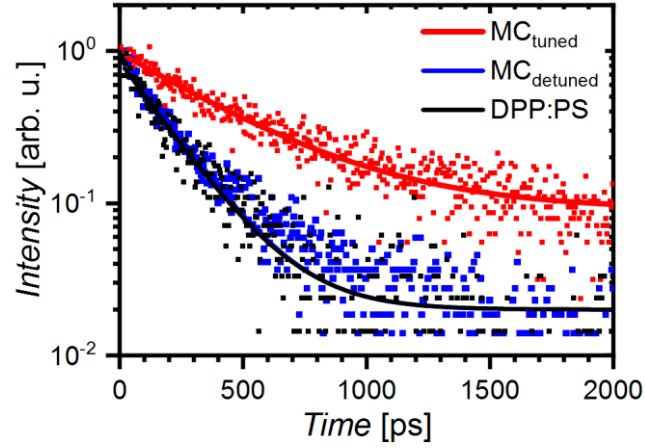
Figure 5.4. Photoluminescence decay (squares) and fitted data (lines) for the tuned microcavity (red) and for two references: DPP:PS film (black), and a detuned microcavity (blue, $MC_{detuned}$) around λ_C.

I would like to stress the role of external quantum efficiency (Equation 5.1) in disentangling the radiative and non-radiative (τ_{NR}) lifetimes and quantifying the Purcell effect. As reported in Equation 5.3, the radiative rate can only be calculated from the quantum efficiency and the overall PL lifetime. Unfortunately, ϕ measurements are rarely reported, making estimations of the actual radiative rate and its variations highly speculative.[42]

$$\tau_R = \frac{\tau_{PL}}{\phi} \qquad (5.3)$$

The fits for the references are almost superimposable as seen in Fig. 5.4. The results of such calculations are summarized in Table 5.1, showing that the two references have similar τ_{PL} (190 ps for the DPP:PS layer and 185 ps for $MC_{detuned}$). Comparable lifetimes are also observed for other references emulating the boundaries of the defect layer (lifetimes in Table 5.1) while its value more than doubles (~ 416 ps) for the tuned microcavity. Regarding ϕ instead, the value for the bare DPP:PS film is ~ 6% which decreases to half for the $MC_{detuned}$ reference (~ 3%) and a sixth for MC_{tuned} (~ 1%). Astonishingly, the microcavity shows a 10-fold increase in radiative lifetime (τ_{rad} ~ 42 ns), as compared to a slight increase for the $MC_{detuned}$ (τ_{rad} =6.2 ns) with respect to the DPP:PS film (τ_{rad} = 3.2 ns). Corresponding changes in the radiative rates are derived ($\boldsymbol{\Gamma}_{rad} = \frac{1}{\tau_{rad}}$) and reported in the same Table.

Table 5.1. Radiative Decays. Photoluminescence lifetime τ_{PL}, quantum yield ϕ, the calculated radiative and non-radiative lifetimes (τ_{rad} and τ_{NR} respectively) and effective refractive index (n_{eff}) for the microcavities and reference films.

Sample	τ_{PL} [ps]	ϕ [%]	τ_{rad} [ns]	τ_{NR} [ps]	Γ_{rad} [ns^{-1}]	Γ_{NR} [ns^{-1}]	n_{eff}
DPP:PS	190 ± 20	6 ± 2	3.2 ± 1.4	202 ± 89	0.32	4.9	1.59
MC$_{detuned}$	185 ± 20	3 ± 1	6.2 ± 2.7	191 ± 84	0.16	5.2	1.49
MC$_{tuned}$	416 ± 20	1 ± 0.5	41.6 ± 22.8	420 ± 230	0.02	2.4	1.47
R1	233 ± 20	6 ± 3	5.8 ± 2.9	248 ± 126	0.17	4.0	1.53
R2	280 ± 20	8 ± 3	3.5 ± 1.3	304 ± 116	0.29	3.2	1.55

From data in Table 5.1, I derive the ratio between the radiative decay rate of the emitter modified by the environment (Γ_{rad}^{mod}) and its decay in vacuum Γ_{rad}, usually called the Purcell factor (P). In our case, P=0.08 ($0.03 \leq P \leq 0.24$ accounting for error) considering the DPP:PS film as a reference and P=0.15 ($0.06 \leq P \leq 0.47$) considering instead the detuned microcavity as a reference. The latter accounting for enhanced self-absorption due to the small Stokes shift and longer photon dwell time in the cavity, out-coupling effects and any variations due to chemical effects or the effective dielectric environment. Notwithstanding the significant error propagating from uncertainty in the quantum yield measurements, the present P values are consistent with a strong radiative rate suppression. If, however, the overall PL rates were considered only, *i.e.* neglecting ϕ as is often found,[29] P would have much larger values (0.44-0.46), falsely indicating a smaller and speculative rate suppression. The PL lifetime and ϕ for all other references in Table 5.1 show very similar values to those discussed earlier. Finally, we notice that the effective refractive index of all our references -also reported in Table 5.1- show a variation below 10%.

3. Discussion

To date, this is the first case where the Purcell effect is unambiguously confirmed in all-polymer planar microcavities. It is then useful to provide a deeper investigation of the phenomena behind it and explain the reasons that prevented its observation so far.

The puzzling results summarized in Table 5.1 concern the simultaneous reduction in ϕ and

increase in τ_{PL} for the tuned microcavity with respect to all references in Table 5.1. Indeed, the decrease of ϕ usually causes a decrease of τ_{PL} due to enhanced non-radiative recombination rates[43] in contrast with our data (Table 5.1) where Γ_{NR} is almost halved. Change in non-radiative rates due to coupling has previously been observed in Fabry–Pérot-resonators.[44] Moreover, the radiative rate is known to be strongly dependent on the effective refractive index surrounding the emitters as demonstrated in planar silicon slot waveguides.[24] The variations in τ_{rad} between the tuned cavity and the references show a remarkable dissimilarity and do not comply with this interpretation as the references have similar effective refractive indices (within 10%) to the MC_{tuned}, making this alternative explanation unsuitable for the radiative rate change observed for our plastic microcavities.

In order to explain the significant extension of the radiative rate for the MC_{tuned}, we must invoke an unusual change in the light-matter interaction - the Purcell-effect - i.e. the modification of the spontaneous emission rate for a quantum system. According to theory, both radiative rate suppression and enhancement should be observable in planar microcavities.[14, 45] Ideally, rate enhancement is achieved when three conditions are satisfied: (i) the electromagnetic field is strongly confined, (ii) the emission intensity is spectrally sharper than the cavity mode and tuned to the region where the LPDOS is maximum and (iii) the emitter is placed at an antinode of the microcavity electric field standing wave, where its intensity is maximum. Conversely, if one or more of these conditions is not satisfied, rate suppression should occur.[46-48]

To discuss the role of these three requirements, it is useful to recall the relevant theoretical framework. According to the Wigner–Weisskopf approximation,[49] the modified emission rate is directly proportional to the LPDOS,[37,50] which is a function of the angular frequency (ω) and of the emitter position (r) in the microcavity, as described by the modified Fermi's golden rule ($\Gamma_{rad}^{mod} = \frac{2\pi}{\hbar^2} LPDOS(\omega, r)$).[40] Then, when LPDOS is minimum at the band gap the radiative rate is suppressed while at the cavity mode (where it is maximum) it can be enhanced. Furthermore, if the emitter is placed at an antinode of the electric field amplitude inside the cavity, the emission is enhanced, and vice versa for the positioning at a node. As DPP is a broad-spectrum emitter, all off-resonance photons are expected to experience suppression due to the value of low density of states outside the cavity mode. This again is assigned to the enhanced dielectric contrast, comparable to that achieved in some inorganic dielectric microcavities, where PL rate enhancement was observed.[45]

Thus far, the achieved result is promising for applications where the suppression of radiative rate and the enhancement of the lifetime is a desired effect, such as light harvesting devices, where the efficiency of the devices is limited by the diffusion length of excitons, and thus by the radiative lifetime.[8] On the other hand, radiative rate enhancement is desired for all light emission applications, most importantly low threshold lasers.

Theoretically, the maximum achievable Purcell factor in a cavity (P_{max}, Equation 5.4)[11] is dictated by the quality factor Q and the effective cavity volume (V_{eff}), representing the electromagnetic field confinement in all the directions.

$$P_{max} = \frac{3}{4\pi^2}\left(\frac{\lambda}{n}\right)^3 \frac{Q}{V_{eff}} \geq \frac{\Gamma_{rad}^{mod}}{\Gamma_{rad}} \tag{5.4}$$

In our case, there is no lateral confinement in the plane of the cavity layer. However, we can estimate the relative confinement along the periodicity direction from the penetration depth (L_{eff}) of the electromagnetic field into the dielectric mirrors (Equation 5.5). The penetration depth depends on the dielectric contrast ($\Delta n = n_H - n_L$), the geometric length of the defect layers (L_{MC}), the optical lengths within the dielectric mirrors (L_{DBR}), the periodicity of the structure (D) and its effective refractive index (n_{eff}).[31]

$$L_{eff} = L_{MC} + 2\,L_{DBR} = L_{MC} + 4D\,\frac{n_{eff}}{|n_H - n_L|} \tag{5.5}$$

In the MC$_{tuned}$ case, L_{eff} is approximately 4.6 μm, much smaller than its overall geometrical length of 9.7 μm. Then, the system shows a stronger confinement with respect to previously investigated all-polymer microcavities, where lower refractive index contrast causes L_{eff} to be comparable or even longer than the photonic structure itself. The data for similar systems in literature and their L_{eff} are reported in Table 5.2.

Table 5.2. Characteristics of one-dimensional all-polymer microcavities reported in literature.

Polymer pairs	Bilayers/mirror	n_{low}	n_{high}	Δn	L_{eff} (μm)	$L_{geometrical}$ (μm)
PVK/PAA[7]	25	1.51	1.68	0.17	7.5	10.0
PVK/PAA[2b]	20	1.51	1.68	0.17	8.8	9.3
PVK/CA[8]	25	1.48	1.66	0.18	7.0	10.0
PS/CA[9]	30	1.46	1.58	0.12	9.3	10.0
PVK/CA[10]	bottom: 20 top: 10	1.48	1.68	0.20	6.2	6.0
PVK/AQ	20	1.35	1.69	0.34	4.6	10.0

PVK = poly(*N*-vinylcarbazole), PAA = poly(acrylic acid), PS=polystyrene, CA= cellulose acetate.

This simple characteristic should explain why radiative rate variations had not been confirmed so far. In fact, Δn= 0.34 represents at least a 50% increase from that of the highest reported in literature for polymer microcavities so far.[28,51] On the other hand, most of the emission of broad emitters is suppressed by the PBG or is leaked outside the cavity mode, hence indicting the need of integration of very narrow emitters (PL full width half maximum smaller than cavity mode width) in the microcavities.

Theoretical and experimental observations indicate the maximum enhancement or suppression for a narrow emitter placed at the antinode of the standing wave in a planar dielectric microcavity is around 30%.[52] Hybrid planar systems using polymer emitters or spacers in dielectric and metallic system report similar enhancement in the overall decay rate, including non-radiative decay.[42,53,54] However, if micropillars or microbeams of micrometer-scale diameter were fabricated from the planar microcavity, the Purcell factor could reach 10.[55] At the state of the art, lateral nanostructuring remains the most reliable approach to radiative rate enhancement.[11]

4. Conclusion

In conclusion, I demonstrated the radiative rate suppression with a 10-fold radiative lifetime increase as well as record PL enhancement in fully solution-processed polymer planar microcavities that could open-up new perspectives for flexible devices. The larger dielectric contrast employed for the microcavity growth allowed observation of unambiguous radiative emission rate variation for the first time, thanks to better confinement within the sample thickness. Nevertheless, smaller mode volume as well as spatial and spectral optimization of fluorophores are still necessary to achieve radiative rate enhancement. The careful synergy of polymer refractive index engineering, advanced dye synthesis and solution-fabricated flexible structures provides novel perspectives to polymer photonics.

5. Materials and Methods

Dye Synthesis. DPP was synthesized following literature procedure.[35]

Microcavity Fabrication. All samples were grown via alternating spin coating of 100 μL of polymer solutions on 25×25 mm^2 glass substrate at 175 rps for the dielectric mirrors and 75 rps for the DPP:PS solution. The mirrors of 20 bilayers were cast by alternating deposition of

Aquivion® D79-25BS water/ethanol dispersion and PVK solution in toluene (40 mg/mL). Spacer layers of CA were cast from solution in diacetone alcohol (30 mg/mL) to minimize any undesired water diffusion from the AQ layers. The emitter layer was obtained by casting a solution of the dye in PS-toluene (DPP: 1mg/mL, PS: 30 mg/mL).

Optical Characterization. Transmittance measurements were performed with a setup consisting of deuterium and tungsten-halogen sources (spectral range 230-2500 nm), an AvaSpec-ULS4096CL-EVO CMOS (spectral range 200-1100 nm, resolution 1.4 nm) spectrometer. Angle resolved spectra have been recorded by a homemade setup of angular resolution ≤ 1°. Steady-state PL measurements were performed by exciting the samples with an Oxxius 405 nm CW laser focused on a 1 mm^2 spot and the fluorescence was collected with the same spectrometer. The collection setup allowed the measurement of transmittance and PL on the same sample spot.

SEM Measurements. SEM measurements were performed using FE-SEM Zeiss SUPRA 40 VP, Carl Zeiss, Oberkochen, Germany at an acceleration voltage of 10 kV. The microcavity sample was frozen in liquid nitrogen and fractured to reveal the cross section on which a thin carbon layer was deposited using a high vacuum evaporator (Polaron 6700, USA).

Time-resolved PL Measurements. TRPL measurements were carried out using a femtosecond tunable Ti:Sapphire laser (Coherent Chameleon Ultra II) laser and a streak camera detection system. Type I phase-matched second harmonic generation was obtained from a β-barium borate crystal, leading to pulses with central wavelengths of 405 nm and a spot diameter of 6-8 μm at the sample. The emission was collected at 30° from normal incidence and analyzed by a spectrograph (Princeton Instruments Acton SP2300) coupled to a streak camera (Hamamatsu C5680), resulting in a spectral resolution around 1 nm and temporal resolution of 20 ps.

Quantum Efficiency. External PL quantum efficiency for microcavities and references were measured as described by the widely utilized method by de Mello et al.[56] using an integrating sphere (Avantes AvaSphere-50) fiber coupled with a 405 nm LDH−P-C-405 laser, and an Avantes AvaSpec-2048 calibrated spectrometer (200-1150 nm resolution). Typical uncertainty in the quantum efficiency measurements for low values (<10%) can be in the range 30-50%.

Refractive Index Measurements. A VASE instrument (J. A. Woollam Co, Lincoln, NE, USA) in the range 250–2500 nm was used for spectroscopic ellipsometry measurements at

different incidence angles from 55° to 75° on films on both fused silica and silicon substrates. Varian Cary 6000i spectrometer in the spectral range of 200–1800 nm was used to measure reflectance and transmittance at normal incidence. Then, the complex refractive index was evaluated using WVASE32® software (J. A. Woollam Co, Version 3.774, Lincoln, NE, USA), adopting oscillator models guaranteeing a Kramers–Kronig consistency.

6. References

(1) Annadhasan, M.; et al. Next-Generation Organic Photonics: The Emergence of Flexible Crystal Optical Waveguides. *Adv. Opt. Mater.* **2020**, *8*, 2000959.

(2) Megahd, H.; et al. Aquivion–Poly(N-vinylcarbazole) Holistic Flory–Huggins Photonic Vapor Sensors. *Adv. Opt. Mater.* **2021**, *9*, 2170017.

(3) Lova, P.; et al. Advances in functional solution processed planar one-dimensional photonic crystals. *Adv. Opt. Mater.* **2018**, *6*, 1800730-1800726.

(4) Purcell, E. M.; et al. Resonance Absorption by Nuclear Magnetic Moments in a Solid. *Phys. Rev.* **1946**, *69*, 37-38.

(5) I. Prieto, J. M. L., L. E. Muñoz-Camúñez, A. G. Taboada, J. Canet-Ferrer, J. M. Ripalda, C. Robles, G. Muñoz-Matutano, J. P. Martínez-Pastor, and P. A. Postigo. Near thresholdless laser operation at room temperature. *Optica* **2015**, *2*, 66-69.

(6) Shambat, G.; et al. Ultrafast direct modulation of a single-mode photonic crystal nanocavity light-emitting diode. *Nat. Commun.* **2011**, *2*, 539.

(7) Cho, H.; et al. Importance of Purcell factor for optimizing structure of organic light-emitting diodes. *Opt. Express* **2019**, *27*, 11057-11068.

(8) Vuong, L. T.; et al. Cavity-controlled radiative recombination of excitons in thin-film solar cells. *Appl. Phys. Lett.* **2009**, *95*, 233106.

(9) Murataj, I.; et al. Hyperbolic Metamaterials via Hierarchical Block Copolymer Nanostructures. *Adv. Opt. Mater.* **2021**, *9*, 2001933.

(10) Gevaux, D. G.; et al. Enhancement and suppression of spontaneous emission by temperature tuning InAs quantum dots to photonic crystal cavities. *Appl. Phys. Lett.* **2006**, *88*, 131101.

(11) Vahala, K. J. Optical microcavities. *Nature* **2003**, *424*, 839-846.

(12) Jacob, Z.; et al. Broadband Purcell effect: Radiative decay engineering with metamaterials. *Appl. Phys. Lett.* **2012**, *100*, 181105.

(13) Megahd, H.; et al. Planar microcavities: Materials and processing for light control. *Opt.*

Mater.: X **2022**, *13*, 100130.

(14) Vredenberg, A. M.; et al. Controlled atomic spontaneous emission from Er3+ in a transparent Si/SiO$_2$ microcavity. *Phys. Rev. Lett.* **1993**, *71*, 517-520.

(15) Xie, Z. G.; et al. Influence of a Single Quantum Dot State on the Characteristics of a Microdisk Laser. *Phys. Rev. Lett.* **2007**, *98*, 117401.

(16) Ding, X.; et al. On-Demand Single Photons with High Extraction Efficiency and Near-Unity Indistinguishability from a Resonantly Driven Quantum Dot in a Micropillar. *Phys. Rev. Lett.* **2016**, *116*, 020401.

(17) Noda, S.; et al. Spontaneous-emission control by photonic crystals and nanocavities. *Nat. Photonics* **2007**, *1*, 449-458.

(18) Rout, D.; et al. Amplified emission and modified spectral features in an opal hetero-structure mediated by passive defect mode localization. *J. Phys. D: Appl. Phys.* **2017**, *51*, 015112.

(19) Petrov, E. P.; et al. Spontaneous Emission of Organic Molecules Embedded in a Photonic Crystal. *Phys. Rev. Lett.* **1998**, *81*, 77-80.

(20) Zhu, Y.; et al. Highly modified spontaneous emissions in YVO4:Eu3+ inverse opal and refractive index sensing application. *Appl. Phys. Lett.* **2012**, *100*, 081104.

(21) Megens, M.; et al. Comment on "Spontaneous Emission of Organic Molecules Embedded in a Photonic Crystal". *Phys. Rev. Lett.* **1999**, *83*, 5401-5401.

(22) Wang, W.; et al. Modified spontaneous emissions of europium complex in weak PMMA opals. *Phys. Chem. Chem. Phys.* **2011**, *13*, 18023-18030.

(23) Petrov, E. P.; et al. Petrov et al. Reply. *Phys. Rev. Lett.* **1999**, *83*, 5402-5402.

(24) Creatore, C.; et al. Modification of erbium radiative lifetime in planar silicon slot waveguides. *Appl. Phys. Lett.* **2009**, *94*, 103112.

(25) Priya; et al. Inhibited spontaneous emission using gaplike resonance in disordered photonic structures. *Phys. Rev. A* **2018**, *98*, 043835.

(26) Gan, X.; et al. Nanophotonic filters and integrated networks in flexible 2D polymer photonic crystals. *Sci. Rep.* **2013**, *3*, 2145.

(27) Lova, P.; et al. Polymeric Planar Microcavities Doped with a Europium Complex. *Crystals* **2020**, *10*, 287.

(28) Athanasiou, M.; et al. Efficient Amplified Spontaneous Emission from Solution-Processed CsPbBr3 Nanocrystal Microcavities under Continuous Wave Excitation. *ACS Photonics* **2021**,

8, 2120-2129.

(29) Pelton, M. Modified spontaneous emission in nanophotonic structures. *Nat. Photonics* **2015**, *9*, 427-435.

(30) Lova, P.; et al. All-polymer photonic microcavities doped with perylene bisimide j-aggregates. *Adv. Opt. Mater.* **2017**, *5*, 1700523.

(31) Lova, P.; et al. Strategies for dielectric contrast enhancement in 1D planar polymeric photonic crystals. *Appl. Sci.* **2020**, *10*, 4122.

(32) Skonieczny, K.; et al. How To Make Nitroaromatic Compounds Glow: Next-Generation Large X-Shaped, Centrosymmetric Diketopyrrolopyrroles. *Angew. Chem. Int. Ed.* **2020**, *59*, 16104-16113.

(33) Grzybowski, M.; Gryko, D. T. Diketopyrrolopyrroles: Synthesis, Reactivity, and Optical Properties. *Adv. Opt. Mater.* **2015**, *3*, 280-320.

(34) Bao, W. W.; et al. Diketopyrrolopyrrole (DPP)-Based Materials and Its Applications: A Review. *Front. Chem.* **2020**, *8*.

(35) Purc, A.; et al. The impact of interplay between electronic and steric effects on the synthesis and the linear and non-linear optical properties of diketopyrrolopyrrole bearing benzofuran moieties. *Org. Chem. Front.* **2017**, *4*, 724-736.

(36) Manfredi, G.; et al. Directional Fluorescence Spectral Narrowing in All-Polymer Microcavities Doped with CdSe/CdS Dot-in-rod Nanocrystals. *ACS Photonics* **2017**, *4*, 1761–1769.

(37) Comoretto, D. *Organic and Hybrid Photonic Crystals*; Springer International Publishing, 2015.

(38) Sultanova, N.; et al. Dispersion Properties of Optical Polymers. *Acta Phys. Pol. A* **2009**, *116*, 585.

(39) da Silva, J. S.; et al. SAXS signature of the lamellar ordering of ionic domains of perfluorinated sulfonic-acid ionomers by electric and magnetic field-assisted casting. *Phys. Chem. Chem. Phys.* **2020**, *22*, 13764-13779.

(40) Barth, M.; et al. Spectral and angular redistribution of photoluminescence near a photonic stop band. *Phys. Rev. B* **2005**, *72*, 085129.

(41) Schubert, E. F.; et al. Highly Efficient Light-Emitting Diodes with Microcavities. *Science* **1994**, *265*, 943-945.

(42) Wang, J.; et al. Purcell effect in an organic-inorganic halide perovskite semiconductor

microcavity system. *Appl. Phys. Lett.* **2016**, *108*, 022103.

(43) Klessinger, M.; Michl, J. *Excited States and Photochemistry of Organic Molecules*; VCH, 1995.

(44) Konrad, A.; et al. Revealing the radiative and non-radiative relaxation rates of the fluorescent dye Atto488 in a λ/2 Fabry–Pérot-resonator by spectral and time resolved measurements. *Nanoscale* **2016**, *8*, 14541-14547.

(45) Goldberg, D.; Menon, V. M. Enhanced amplified spontaneous emission from colloidal quantum dots in all-dielectric monolithic microcavities. *Appl. Phys. Lett.* **2013**, *102*, 081119.

(46) Yamamoto, Y.; et al. Micro-cavity semiconductor lasers with controlled spontaneous emission. *Opt. Quantum Electron.* **1992**, *24*, S215-S243.

(47) Bjork, G. On the spontaneous lifetime change in an ideal planar microcavity-transition from a mode continuum to quantized modes. *IEEE J. Quantum Electron.* **1994**, *30*, 2314-2318.

(48) Björk, G.; et al. Modification of spontaneous emission rate in planar dielectric microcavity structures. *Phys. Rev. A* **1991**, *44*, 669-681.

(49) Scully, M. O.; Zubairy, M. S. *Quantum Optics*; Cambridge University Press, 1997.

(50) Frezza, L.; et al. Directional enhancement of spontaneous emission in polymer flexible microcavities. *J. Phys. Chem. C* **2011**, *115*, 19939 - 19946.

(51) Menon, V. M.; et al. Lasing from InGaP quantum dots in a spin-coated flexible microcavity. *Opt. Express* **2008**, *16*, 19535-19540.

(52) Tanaka, K.; et al. Cavity-Induced Changes of Spontaneous Emission Lifetime in One-Dimensional Semiconductor Microcavities. *Phys. Rev. Lett.* **1995**, *74*, 3380-3383.

(53) Chebykin, A. V.; et al. Strong Purcell effect in anisotropic ϵ-near-zero metamaterials. *Phys. Rev. B* **2015**, *91*, 205126.

(54) Lemmer, U.; et al. Microcavity effects in a spin-coated polymer two-layer system. *Appl. Phys. Lett.* **1995**, *66*, 1301-1303.

(55) Böckler, C.; et al. Electrically driven high-Q quantum dot-micropillar cavities. *Appl. Phys. Lett.* **2008**, *92*, 091107.

(56) de Mello, J. C.; et al. An improved experimental determination of external photoluminescence quantum efficiency. *Adv. Mater.* **1997**, *9*, 230-232.

Chapter 6: Purcell Effect in the Near Infrared Range
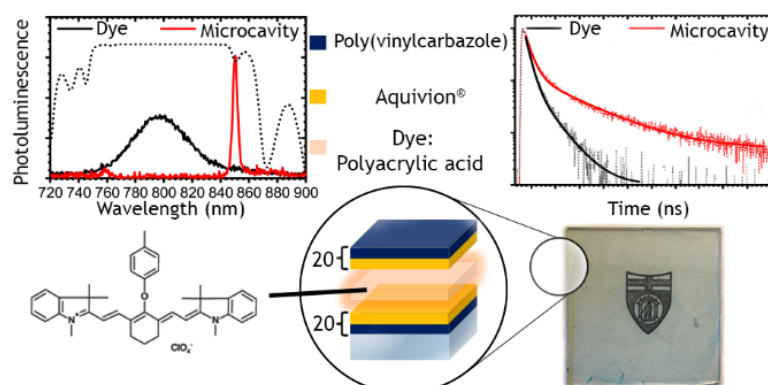
Abstract

The control of radiative decay rate is a crucial issue both for fundamental studies in quantum electrodynamics and for the development of efficient lasers, light emitting devices and photovoltaic cells. In this chapter I investigate the integration of a near-infrared molecular fluorophore in an all-polymer planar microcavity. Subsequently, I report the modulation of the fluorescence decay and radiative rate of the dye used and, in addition, of its fluorescence spectral line-shape and intensity. These effects have been possible through engineering the dielectric contrast of the polymers used to grow the flexible dielectric mirrors thus blazing a trail to innovative opportunities for invisible near-infrared-light communications and wireless technologies.

This chapter is partially reproduced from:

1. Introduction

Optical microcavities of different morphologies have long been a popular means of controlling photoluminescence (PL) and electroluminescence of various emitters.[1] As they confine electromagnetic fields at their resonant frequencies to a small volume, they strongly influence the light-matter interaction for fluorophores inside the cavity. Spontaneous emission rate is, in fact, not an intrinsic property of emitters, but highly influenced by the surrounding electromagnetic medium in what is known as the Purcell effect, first theorized by its namesake in 1946.[2] As such through quantum electrodynamic effects, it is possible to engineer the radiative rate of an emitter placed in an appropriately engineered medium, which allows for higher efficiency optical devices, such as light emitting devices (LEDs)[3,4] or photovoltaics.[5,6]

One of the simplest microcavity architectures to fabricate is the planar variety based on one-dimensional photonic crystals, also known as distributed Bragg reflectors (DBRs) or dielectric mirrors. Due to their facile fabrication and scalability, DBRs have found use in applications ranging from lasers, photovoltaics and sensors to aesthetic applications in architecture and art.[7] These structures consist of a repeating motif of bilayers of dielectric materials with different refractive index that gives rise to constructive or destructive interference due to refraction and reflection at the layer interfaces at distinct wavelengths. These wavelengths depend on the refractive index of the layers as well as their thickness, which accordingly results in controllable reflectance maxima for wavelengths where light cannot propagate into the structure, known as Photonic Bandgaps (PBGs).[8] However, when the periodicity of these structures is interrupted by an anomalous layer, allowed modes are introduced where some wavelengths in the PBG spectral region are permitted to propagate in the structure, [9] termed the microcavity modes (MC).[10] This is similar to microcavities consisting of metallic mirrors, however, dielectric mirrors provide lower losses than their metallic counterparts.[1,11,12]

At both the edges of the PBG and the microcavity mode, the local photonic density of states (LPDOS) is highly increased while at the PBG it is drastically diminished, ideally to zero. The LPDOS describes the number of photonic states available to the system per unit energy,[13] which controls the radiative rate and the PL intensity. The radiative rate (Γ_{rad}) can be interpreted in terms of the LPDOS as described by the modified Fermi's

golden rule (Equation 6.1),[13] where ω is the angular frequency and r is the position of the emitter in the cavity.

$$\Gamma = \frac{2\pi}{\hbar^2} LDOS(\omega, r) \qquad (6.1)$$

Thus, depending on the tuning of the cavity mode with respect to the PL of the emitter and its geometrical positioning, both radiative rate enhancement and suppression can be achieved.[14] As polymers possess unique flexibility and processability, all-polymer microcavities allowing enhancement effects in combination with the recent leaps in polymer-based devices such as organic LEDs and solar cells, would allow efficiency enhancement of these flexible and solution-processed devices.[15-17] The possibility of emission rate control was theorized to be achievable through the use of special polymers or nanocomposites that provide particularly high or low refractive index in dielectric mirrors.[18] While radiative rate control has been routinely achieved in planar microcavities based on inorganic dielectrics, the effect has only recently been confirmed in all-polymer microcavities, partly due to the use of low-index perfluorinated polymers.[19] Perfluorinated sulfonic acid dispersions are promising solution-processable polymers with unique electrical, optical and thermal properties that have found applications in a myriad of fields.[20-23] Thus, I have reported in the previous chapter on the use of microcavities employing the low refractive index perfluorinated polymer Aquivion® (AQ) to achieve not only intensity enhancement of an organic emitter in the visible range, but more importantly its effect on altering the radiative lifetime by virtue of increasing the dielectric contrast between the polymers used in constructing the DBRs forming the dielectric mirrors.[19]

Here, I demonstrate that this effect is also achievable for near infrared (NIR) organic emitters, which is critical due to the importance of the NIR range for communication, sensing, biological imaging and solar cells.[24-28] Even though molecular design,[29] supramolecular assemblies[30-32] and dye blends[33,34] offer an approach to fluorescence kinetics control, using photonic structures offers broad applicability, high effectiveness and a straight-forward experimental method. This offers more flexibility in achieving fluorescence control in solid state devices through simply incorporating the microcavities in the system design without changing the dye used.

While different polymer-based fluorophores were investigated in polymer cavities supporting whispering-gallery modes,[35-37] they require more sophisticated nanolithography or self-assembly fabrication that can be difficult to scale or more prone to disorder. Herein, I report on the modulation of radiative lifetime of 2-[2-[2-(4-methylbenzeneoxy)-3-[(1,3-dihydro-1,3,3-trimethyl-2H-indol-2ylidene)ethylidene]-1-cycloxen-1-yl]-ethenyl]-1,3,3-trimethyl-1H indolium perchlorate, an NIR emitting dye (thereafter referred to simply as "dye") blended with poly(acrylic acid) (PAA) and embedded in an all-polymer microcavity. The use of AQ as a low-index polymer and poly(N-vinylcarbazole) (PVK) as a high-index one in the DBRs results in refractive index contrast of $\Delta n \approx 0.33$ at the spectral range of interest, comparable to that achievable in some inorganic structures.[38] The engineering of the PBG and the MC mode to the PL spectral range of the dye provides an opportunity to observe interesting cavity effects.

2. Results and Discussion

Dye Properties and Microcavity Design

Panel a of Fig. 6.1 reports the PL and absorption spectra of the Dye:PAA blend cast on a glass substrate. The absorption maximum is observed at 777 nm (12870 cm^{-1}) followed by a broader shoulder at about 710 nm (14084 cm^{-1}) probably masking an additional vibronic replica.
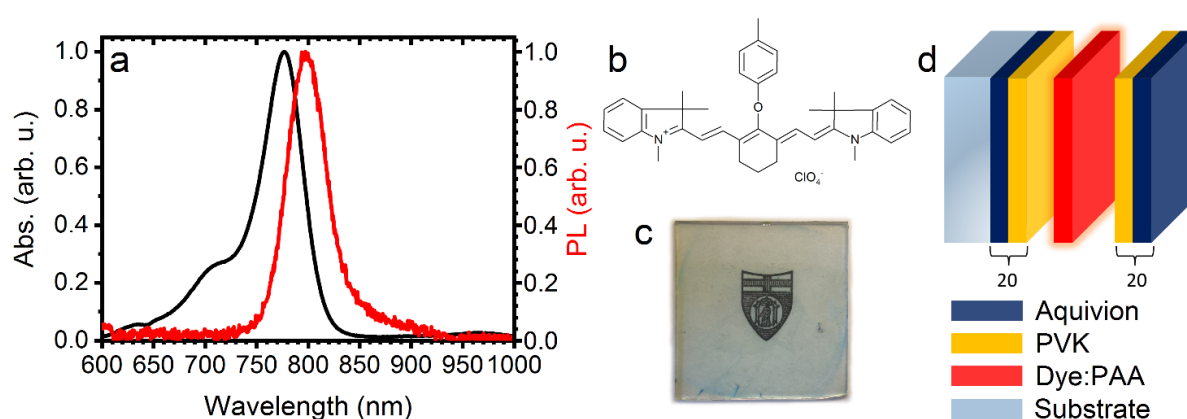

Figure 6.1. a) Normalized absorption (black) and PL (red) of a thin film of the ADS760MP dye dispersed in PAA. b) Chemical structure of the dye. c) Digital photograph of the VIS-transparent, NIR-tuned microcavity cast on a glass substrate. d) Schematic of the microcavity structure.

On excitation using a 405 nm laser, the fluorescence spectrum shows a maximum at 798 nm and is not symmetrical with respect to the absorbance spectrum. Indeed, vibronic features are not detected, indicating a different electron-phonon coupling in the ground and excited electronic states and a small Stokes shift of 21 nm. The chemical structure of the dye is shown in Fig. 6.1b. This dye consists of a polymethine chain linking two terminal heterocycles, each of which is bonded to a nitrogen atom conjugated to the chain. In the present case, the heterocycles are coplanar to the conjugated bonds thanks to the saturated bridges, which prevent ring torsions thus extending the delocalization of electrons. The central conjugated bond of the molecule is also stabilized by a cyclic saturated bridge carrying in the opposite position a phenyl-oxy electron donor group. All these features induce a strong reduction of the HOMO-LUMO transition energy to the NIR.[39,40] A digital photograph in Fig. 6.1c shows the microcavity containing the Dye:PAA blend cast on a glass substrate, where the PBG and MC mode wavelengths are tuned to the emission of the dye. The sample demonstrates high transparency and remarkable lack of colouring, as its first order PBG lies in the infrared range, with a slight tint due to the low-intensity second order PBG in the violet range (see Fig. 6.2a and b). Casting parameters were engineered to produce multiple sample types: one where the PBG overlaps the emission of the dyes (MC_{tuned}), and another where the PBG is instead offset to shorter wavelengths ($MC_{detuned}$) to act as a reference emulating the physicochemical environment, yet without the photon localization effect in the NIR range. The microcavities comprise two identical DBRs formed of 20 bilayers of AQ/PVK pairs, sandwiching a layer of the Dye:PAA blend as schematized in Fig. 6.1d.

Steady-state Optical characterization

The normalized reflectance spectra of MC_{tuned} and the control $MC_{detuned}$ are plotted in Fig. 6.2a, showing the characteristic signatures of 1D planar microcavities.[7,9] The two samples have a comparable bandwidth of 0.21 (MC_{tuned}) and 0.19 ($MC_{detuned}$) eV, in the range 1.45-1.66 eV or 750-870 nm for MC_{tuned} and 2.47-2.66 eV or 462-513 nm for $MC_{detuned}$. The principal microcavity modes are observed at 850 and 475 nm, respectively. The complementary absolute transmittance of MC_{tuned} at normal collection is reported in Fig. 6.2b (solid black line) while the calculated value is shown in grey. Using the refractive index of AQ,[20] PVK,[41] and the Dye:PAA blend as an input for the

transfer matrix method (TMM) calculations,[42] the thicknesses of the polymer layers were retrieved to be approximately 112 and 420 nm for PVK and the Dye:PAA cavity layer, respectively. Due to the affinity of AQ for water, the layers in the lower DBR (which were cast first) have a thickness of around 156 nm, slightly thicker than the 153 nm of the layers in the upper DBR, providing minor asymmetry to the structure. The peak positions and intensities of the cavity modes, both the first and second order PBGs and the interference fringes agree to a great extent. Figure 2c shows the fluorescence spectra collected normal to the surface from the Dye:PAA blend thin film (black), $MC_{detuned}$ (blue) and MC_{tuned} (red) excited by a 405 nm laser.

Clearly, the PL for $MC_{detuned}$ has a similar emission shape to that of the Dye:PAA blend. Contrarily, the spectral overlap between the PBG and the microcavity mode of MC_{tuned} and the emission of the NIR dye completely alters the fluorescence shape and intensity, giving rise to a dramatic spectral redistribution well known in these systems independently of the emitter used.[38,43,44] As expected from the typical LPDOS, the emission from wavelengths that correspond to the PBG are completely suppressed due to the near-zero LPDOS, and the emission is funnelled instead into the wavelengths with higher LPDOS at the cavity mode. Remarkably, due to the relatively wide PBG, approximately all off-resonance PL is suppressed, which was not the case for all-polymer microcavities previously reported.[41, 43-45] Due to the MC_{tuned} mode (~850 nm), the intensity of CW fluorescence is increased 10-fold compared to $MC_{shifted}$ and 15-fold compared to the Dye:PAA blend film. Interestingly, the full width at half maximum (FWHM) of the cavity mode is ~4 nm, making its quality factor around 210, comparable to the highest reported so far in all-polymer microcavities (255)[45] and to inorganic microcavities of similar dielectric contrast.[38]
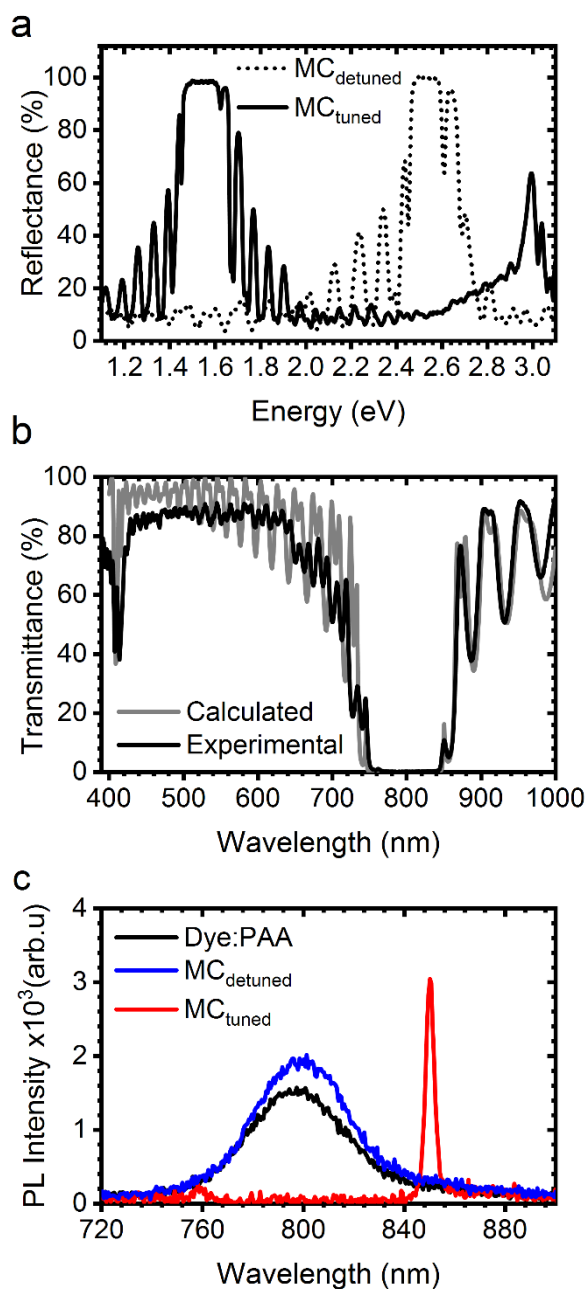
Figure 6.2. a) Reflectance spectra of the tuned microcavity (black solid line) and the detuned one (dashed line). b) Experimental (black) and calculated (grey) transmittance spectra for MC_{tuned}. c) Comparison of the photoluminescence measurements from the pristine Dye:PAA film (black), $MC_{detuned}$, and MC_{tuned}.

Thus far, the efficient leverage of using microcavities for the control of fluorescence spectral characteristics is evident. Most importantly, as mentioned in the introduction, these effects also extend to the exceptional change of the radiative lifetime of the fluorophore embedded in the microcavity.

Radiative Lifetime Effects

Measurements of fluorescence lifetime show that there exists a significant effect of the microcavities on the dynamics of PL from the dye indicating a clear effect on the quantum electrodynamics of the system. Integrated time-resolved fluorescence signals in the spectral range 700-870 nm and their best fit are displayed in Fig. 6.3.

The intrinsic response function (IRF) of the setup is also reported in a solid grey line, showing the limit of the instrument temporal resolution. It is immediately apparent that the decay is different for all three samples, with the fastest being that of the standalone Dye:PAA, and the slowest that of the tuned cavity. As the photophysics of the dye itself is unknow and of little interest to this work, I focus on comparing its behaviour in the thin polymer blend film to the microcavities.
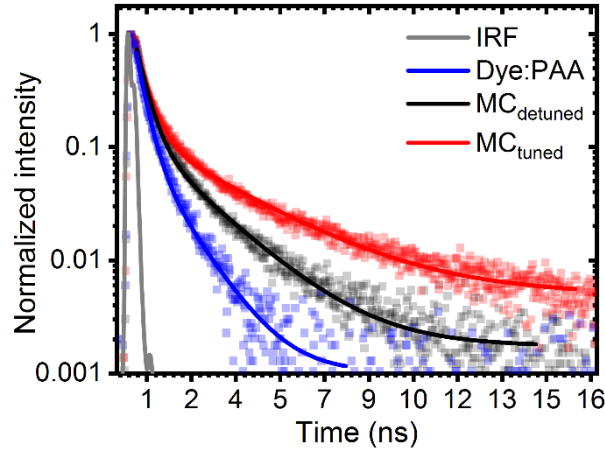
Figure 6.3. Photoluminescence decay (squares) and fitted data (lines) for the Dye:PAA film (blue), the detuned microcavity (black) and the tuned microcavity (red).

To make a preliminary comparison of the radiative (Γ_{rad}) and non-radiative (Γ_{NR}) processes occurring in the three systems being analysed; I first calculate the intensity-averaged fluorescence decay lifetime in Table 6.1. We notice an increase in fluorescence lifetime for both $MC_{detuned}$, and MC_{tuned}.

Even though the PL lifetimes inferred from the measurement show the significant effect on the overall fluorescence lifetime from the tuned microcavity with respect to references, it is not possible to confirm any modulation of the radiative rate without the proper measurement of the external quantum yield, which allows to disentangle

radiative from non-radiative decays ($\phi = \frac{\Gamma_{rad}}{\Gamma_{rad} + \Gamma_{NR}}$).[46] Therefore, ϕ for each sample is reported in Table 6.1 as well.

Table 6.1. Average Photoluminescence lifetime τ_{PL}, quantum yield ϕ and the calculated radiative and non-radiative lifetimes (τ_{rad} and τ_{NR} respectively) and rates (Γ_{rad} and Γ_{NR}) for the Dye:PAA film and microcavities.

Sample	τ_{PL} (ns)	ϕ (%)	τ_{rad} (ns)	τ_{NR} (ns)	Γ_{rad} (ns^{-1})	Γ_{NR} (ns^{-1})
Dye:PAA	0.7 ± 0.2	19 ± 3	3.6 ± 1.7	0.9	0.27	1.2
MC$_{detuned}$	1.2 ± 0.2	8 ± 2	12.4 ± 4.6	1.3	0.08	0.8
MC$_{tuned}$	1.9 ± 0.2	5 ± 2	39.6 ± 18.2	2.0	0.03	0.5

The standalone Dye:PAA film shows a moderately high PL quantum efficiency of 19%. However, this is roughly halved for the detuned microcavity, and quartered for the tuned one. As the quantum yield is calculated for all orientations and angles for a range of wavelengths 700-1100 nm, it is not possible to neither spectrally nor angularly resolve its value to evaluate the radiative rate for different decays. However, using average values, it is possible to estimate the average radiative and non-radiative lifetimes ($\tau_{rad} = \frac{\tau_{PL}}{\phi}, \tau_{NR} = \frac{\tau_{PL}}{1-\phi}$), also reported in Table 6.1. For both the tuned and detuned microcavities, there exists a significant change in both radiative and nonradiative lifetimes. However, that extent of change is smaller in the reference MC$_{detuned}$, indicating that there are some unintended effects that might include, but are not limited to, exciton chemical traps, impurities, local disorder, polarity of the medium and residual solvent diffusion among layers,[18] which are not observed in the Dye:PAA film being related to the microcavity structure and its growth process. For this reason, the effect of electric field confinement in the tuned cavity can be clearly estimated only using MC$_{detuned}$ as a reference. As such, the ratio between the radiative rate of emission ($\Gamma_{rad} = \frac{1}{\tau_{rad}}$) from the tuned and detuned cavities (i.e the Purcell effect) can be quantified as approximately 0.3, indicating a reduction of the radiative rate comparable with values obtained for

inorganic planar one-dimensional MCs.[47,48] On the other hand, the non-radiative decay rate varies to a smaller extent between the two samples.

Electric Field Propagation at Microcavity Mode

To explain the observation of radiative lifetime increase, and thus radiative rate suppression, in the fabricated all-polymer microcavity, the effect of the cavity on the electric field distribution must be evaluated quantitatively. I calculated the electric field propagation through the structure at all the wavelengths of interest by the TMM.[7,49] Fig. 6.4a shows the results of these calculations of the normalized squared modulus of the field in the range 700-900 nm throughout the depth of the structure. The plot shows the relative intensity of the propagating electric field impinging at normal incidence, starting at the surface (i.e. depth=0 μm), highlighting the cavity layer in red. The yellow shades of the contour plot indicate a negligible intensity of the electric field, while the dark blue indicates the maximum values. For the wavelengths in the range of the PBG, the field propagation is exponentially damped throughout the structure until it completely disappears. On the other hand, the field for wavelengths around the cavity mode (850 nm) increase in intensity, reaching their highest value at the defect layer (~5 μm, red). Different behaviour is observed for the interference fringes which oscillate in intensity through the structure of the microcavity. Figure 6.4b reports the electric field intensity at the cavity mode wavelength (850 nm), showing clearly that its maximum value is achieved in the defect layer, highlighted in red. However, it also shows that the defect layer overlaps not only an antinode of the electric field (the peak in Fig. 6.4b, red area), but also two nodes (the side minima in Fig. 6.4b, red area).The relationship between the ratio of radiative rate in a microcavity (Γ_C) relative to that in a homogeneous medium (Γ_0), the microcavity wavelength (λ_C), the refractive index in the cavity n, the quality factor Q, the effective volume V_{eff}, the placement relating to the electric field intensity (E), the spectral overlap between the cavity mode wavelength and the emitted wavelength (for a monochromatic emitter (λ_x) as well as a leaky mode factor f is outlined in a modified form of the Purcell factor (Equation 6.2).[10]

$$\frac{\Gamma_{Mc}}{\Gamma_0} = \frac{3}{4\pi^2} \left(\frac{\lambda_C}{n} \right)^3 \frac{Q}{V_{eff}} \times \frac{|E(r)|^2}{|E_0|^2} \times \left(\frac{\Delta\lambda_C^2}{\Delta\lambda_C^2 + 4(\lambda_C - \lambda_x)^2} \right) + f \qquad (6.2)$$

Clearly, there is a significant radiative rate inhibition mechanism occurring as most fluorescence from the dye overlaps the PBG wavelength, causing an inhibition effect. Ideally, the use of a narrow emitter and thinner cavity layer would allow more finer control on the effect and observing only radiative rate enhancement or inhibition, depending on the spectral and positional overlap.
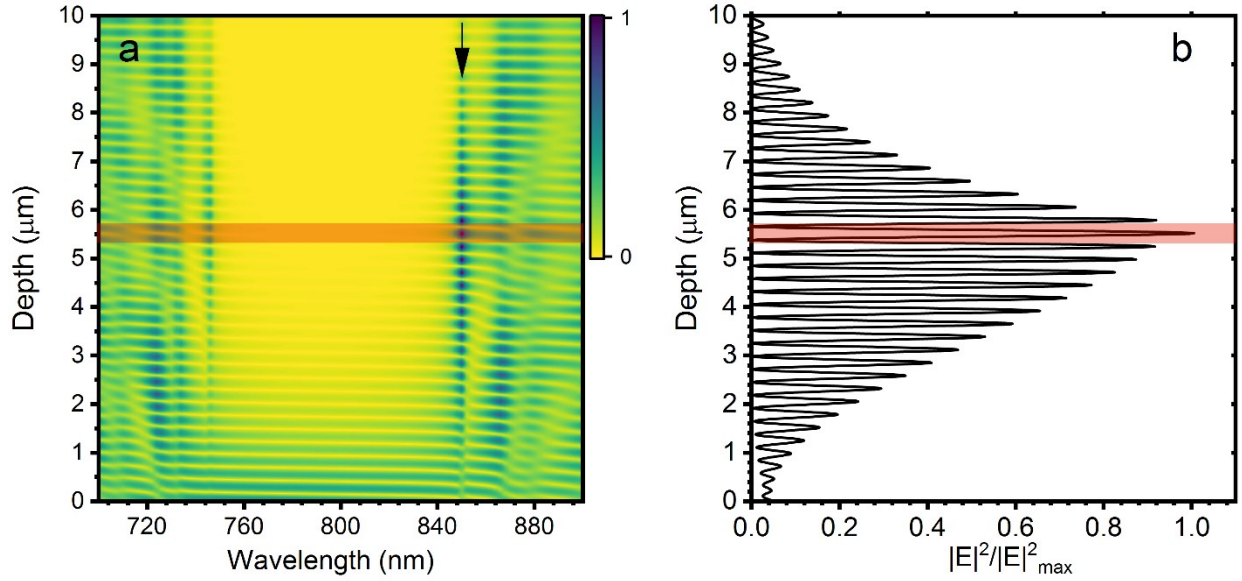

Figure 6.4. a) Relative value of the square modulus of the electric field propagation in MC_{tuned} at different wavelengths and positions along the cavity depth. b) Normalized value of the square modulus of the electric field at 850 nm as a function of the depth of MC_{tuned}.

To explain why strong radiative rate variation effects were hardly reported before in literature, I compare the microcavity structure used in this investigation using PVK/AQ as building blocks of the DBRs with previously studied polymer pairs. These are polystyrene (PS)/cellulose acetate (CA) (PS/CA, (Δn=0.109),[50] PVK/CA (Δn=0.212)[44] and PVK/PAA (Δn=0.197) with PS and PVK being the higher index polymers.[43] TMM calculations were performed for microcavities of identical cavity mode wavelengths and overall structures, whose calculated transmittance spectra are reported in Fig. 6.5a. The low dielectric contrast between the PS and CA results in a planar microcavity with a PBG that fails to reflect 100% of the incident light, with a transmittance of about 2%). For PVK/CA and PVK/PAA based microcavities with a comparable refractive index thickness difference, the transmittance of the PBG is zero with a wider band than that

for PS/CA, but less narrow than that of PVK/AQ. Hypothetically, using a pair of higher refractive index such as PVK/Hyflon, would result in even wider PBGs and greater confinement, however the processability of Hyflon is much lower than that here observed for AQ.[8,9]
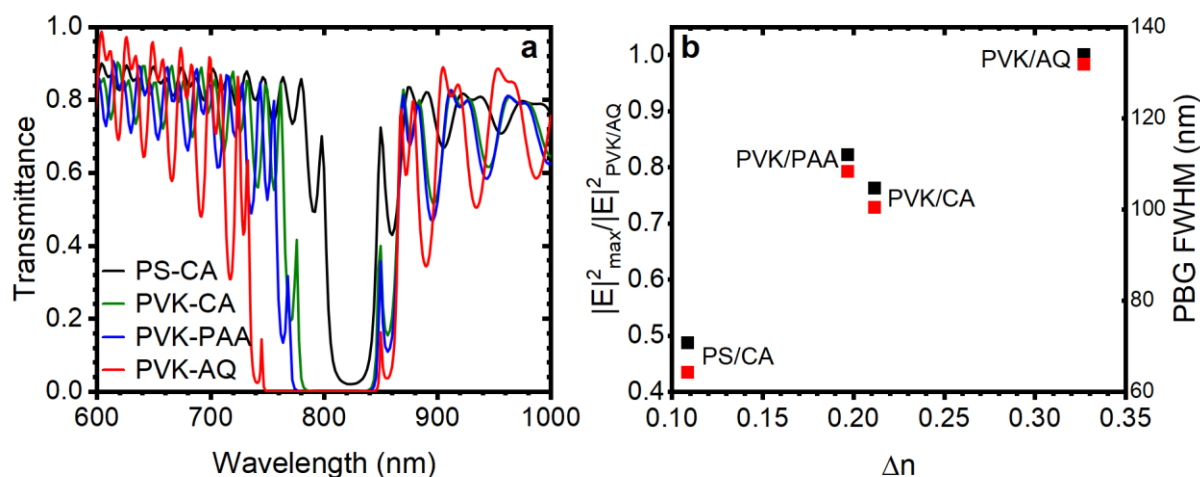

Figure 6.5. a) Simulated transmittance for microcavities using different polymer pairs for the DBRs, b) Normalized value of the square modulus of the electric field at the microcavity mode wavelength (black squares) with respect to that of PVK/AQ pairs, and FWHM of the PBG (red squares) for different polymer pairs forming theoretical dielectric mirrors.

The ratio between the maximum square modulus of the electric field at the cavity mode in different microcavities and that in the investigated PVK/AQ microcavity (black) are plotted as a function of the dielectric contrast in the DBR in Fig. 6.5b. An almost linear relationship between the extent of electric field enhancement as a function of the dielectric contrast between the polymers used to form the DBR is noted. It thus solidifies the extreme importance between engineering the dielectric contrast between mutually processable polymers and the extent of confinement that the microcavities can achieve. A similar linear trend is noticed for the FWHM of the PBG (red squares), where polymer pairs of higher refractive index contrast reflect a wider PBG at normal incidence. The PVK/AQ pairing shows the highest refractive index contrast and consequently the widest PBG, which ideally must be broader than the fluorescence spectrum. This is essential for suppressing as much of the off-resonance fluorescence as possible, especially in the case of polychromatic fluorescent dyes like organic emitters to funnel the majority of emitted light within the cavity mode. Correspondingly, it is of high

importance to further develop polymers, blends, and hybrid systems[51, 52] pushing the limits of refractive index of traditional polymers for more advanced photonic applications.

3. Materials and Methods

Microcavity Fabrication. All samples were fabricated through sequential spin coating deposition of 100 μL of polymer solutions at 170-190 rps on glass substrates. Aquiviona® D79-25BS was provided by Solvay Specialty Polymers and used as a water/ethanol dispersion of different ratios depending on the desired thickness. PVK (Acros Organics) was used as a solution in toluene (Sigma Aldrich, anhydrous 99.8%) at a concentration of 40 mg/mL. The NIR emitter dye (ADS760MP) was acquired from American Dye Source, Inc. and used as a blend (1 mg/mL) in PAA (Aldrich)/ethanol solution (188 mg/mL), referred to as Dye:PAA. Spinning velocity and AQ dispersion concentrations were engineered to tune the position of the bandgap as required. I prepared two sets of microcavities: one tuned on the dye fluorescence (MC$_{tuned}$) and the other fully detuned form the fluorescence (MC$_{detuned}$) to be used as a reference for dye emission without cavity effects.

Optical Characterization. Normal-incidence reflectance measurements were recorded through a customized optical fiber-based setup consisting of deuterium and tungsten-halogen sources (spectral range 230-2500 nm) using reflectance from a UV-enhanced aluminum mirror or a protected silver mirror as a reference (Thorlabs). The reflected signal was collected using an AvaSpec-ULS4096CL-EVO (CMOS) (spectral range 200-1100 nm, resolution 1.4 nm) spectrometer. Angle-resolved transmittance and PL spectra were recorded using a homemade setup of angular resolution ≤ 1° employing the same spectrometer. Steady-state PL measurements were performed by exciting the samples with an Oxxius 405 nm CW laser focused on a 1 mm^2 spot, and the signal was collected with a parabolic mirror and then detected with the aforementioned spectrometer. The collection setup allowed the measurement of transmittance and PL at the same spot.

Time-resolved PL measurements. PL decay was recorded using a PicoQuant Time-Correlated Single-Photon Counting system (Time Harp 260 PICO board with a temporal resolution of 150 ps, a PMA Hybrid 40 detector, and a 405 nm LDH-P-C-405 laser (PicoQuant, Berlin, Germany) with a PDL 800B driver with a 5–80 MHz repetition rate as the excitation source). The PL signal was filtered through a premium long-pass filter, with a cut-on wavelength of 700 nm (Thorlabs, FELH0700) to exclude any possible interference from the

PL of the polymers used in the DBR at shorter wavelengths.

Quantum Yield Measurements. External PL quantum yield for microcavities and references were determined through the method described by de Mello et al.[53] An integrating sphere (Avantes AvaSphere-50) was used, with a 405 nm LDH−P-C-405 laser as an excitation source and the signal was collected with the same spectrometer used for steady-state optical characterization.

4. Conclusions

In conclusion, in this chapter I have shown the possible effects of light confinement in a suitably engineered dielectric microcavity for controlling the radiative rate in the NIR spectral range. Through simply changing the casting parameters I was able to engineer fully solution-processed planar microcavities both tuned to the emission of the embedded dye and a reference to account for any unintended effects. Despite providing only one-dimensional confinement, the properly tuned microcavity enhanced the fluorescence of the near infrared dye by more than 10-fold. More importantly, I demonstrate that the combination between the high-dielectric contrast and defect layer positioning can influence the radiative and non-radiative rates of a fluorophore in an aptly designed microcavity compared to both the stand-alone dye and a reference simulating the chemical and dielectric environment. Additional developments in the field are possible upon increasing the dielectric contrast of the polymer DBRs, using sharper emitters as well as further reducing the cavity width thus demonstrating polymer chemistry as a tool to develop quantum electrodynamics.

5. References

(1) Vahala, K. J. Optical microcavities. *Nature* **2003**, *424*, 839-846.

(2) Purcell, E. M.; et al. Resonance Absorption by Nuclear Magnetic Moments in a Solid. *Phys. Rev.* **1946**, *69*, 37-38.

(3) Shambat, G.; et al. Ultrafast direct modulation of a single-mode photonic crystal nanocavity light-emitting diode. *Nat. Commun.* **2011**, *2*, 539.

(4) Cho, H.; et al. Importance of Purcell factor for optimizing structure of organic light-emitting diodes. *Opt. Express* **2019**, *27*, 11057-11068.

(5) Vuong, L. T.; et al. Cavity-controlled radiative recombination of excitons in thin-film solar cells. *Appl. Phys. Lett.* **2009**, *95*, 233106.

(6) Sgrignuoli, F.; et al. Purcell effect and luminescent downshifting in silicon nanocrystals coated back-contact solar cells. *Sol. Energy Mat. Sol. Cells* **2015**, *132*, 267-274.

(7) Lova, P.; et al. Advances in functional solution processed planar 1d photonic crystals. *Adv. Opt. Mater.* **2018**, *6*, 1800730.

(8) Saleh, B. E.; Teich, M. C. *Fundamentals of Photonics*; John Wiley & Sons, 2019.

(9) Megahd, H.; et al. Planar microcavities: Materials and processing for light control. *Opt. Mater.: X* **2022**, *13*, 100130.

(10) Kavokin, A.; et al. *Microcavities*; Oxford University Press, 2017.

(11) Khurgin, J. B. How to deal with the loss in plasmonics and metamaterials. *Nat. Nanotechnol.* **2015**, *10*, 2-6.

(12) Lanfranchi, A.; et al. Multilayer Polymer Photonic Aegises Against Near-Infrared Solar Irradiation Heating. *ACS Appl. Mater. Interfaces* **2022**, *14*, 14550-14560.

(13) Barth, M.; et al. Spectral and angular redistribution of photoluminescence near a photonic stop band. *Phys. Rev. B* **2005**, *72*, 085129.

(14) Lodahl, P.; et al. Controlling the dynamics of spontaneous emission from quantum dots by photonic crystals. *Nature* **2004**, *430*, 654-657.

(15) Athanasiou, M.; et al. Efficient Amplified Spontaneous Emission from Solution-Processed CsPbBr3 Nanocrystal Microcavities under Continuous Wave Excitation. *ACS Photonics* **2021**, *8*, 2120-2129.

(16) Puthiya Purayil, N.; et al. All-Optical Diode Action through Enhanced Nonlinear Response from Polymeric Photonic Crystal Microcavity. *ACS Appl. Electron. Mater.* **2022**, *4*, 138-148.

(17) Vijisha, M. V.; et al. Impressive nonlinear optical responses of a cationic porphyrin derivative in a flexible all-polymer Bragg stack on optical Tamm mode coupling. *J. Mater. Chem. C* **2020**, *8*, 12689-12697.

(18) Lova, P.; et al. Strategies for dielectric contrast enhancement in 1D planar polymeric photonic crystals. *Appl. Sci.* **2020**, *10*, 4122.

(19) Megahd, H.; et al. All-Polymer Microcavities for Fluorescence Radiative Rate Modification of a Diketopyrrolopyrrole Derivative. *ACS Omega* **2022**, *7*, 15499-15506.

(20) Megahd, H.; et al. Aquivion–Poly(*N*-vinylcarbazole) Holistic Flory–Huggins Photonic

Vapor Sensors. *Adv. Opt. Mater.* **2021**, *9*, 2170017.

(21) Skulimowska, A.; et al. Proton exchange membrane water electrolysis with short-side-chain Aquivion® membrane and IrO2 anode catalyst. *Int. J. Hydrog. Energy* **2014**, *39*, 6307-6316.

(22) Lin, J.; et al. Charge dynamics and bending actuation in Aquivion membrane swelled with ionic liquids. *Polymer* **2011**, *52*, 540-546.

(23) D'Urso, C.; et al. Towards fuel cell membranes with improved lifetime: Aquivion® Perfluorosulfonic Acid membranes containing immobilized radical scavengers. *J. Power Sources* **2014**, *272*, 753-758.

(24) Dou, L.; et al. Low-Bandgap Near-IR Conjugated Polymers/Molecules for Organic Electronics. *Chem. Rev.* **2015**, *115*, 12633-12665.

(25) Alessandro, M.; et al. Visible light communication with efficient far-red/near-infrared polymer light-emitting diodes. *Light: Advanced Manufacturing 9*, 708-718.

(26) McDonald, S. A.; et al. Solution-processed PbS quantum dot infrared photodetectors and photovoltaics. *Nat. Mater.* **2005**, *4*, 138-142.

(27) Hong, G.; et al. Near-infrared fluorophores for biomedical imaging. *Nat. Biomed. Eng* **2017**, *1*, 0010.

(28) Hao, S.; et al. Enhancing dye-sensitized solar cell efficiency through broadband near-infrared upconverting nanoparticles. *Nanoscale* **2017**, *9*, 6711-6715.

(29) Shimizu, S.; et al. Rational Molecular Design towards Vis/NIR Absorption and Fluorescence by using Pyrrolopyrrole aza-BODIPY and its Highly Conjugated Structures for Organic Photovoltaics. *Chem. - Eur. J.* **2015**, *21*, 2893-2904.

(30) Chen, X.-M.; et al. Light-fueled transient supramolecular assemblies in water as fluorescence modulators. *Nat. Commun.* **2021**, *12*, 4993.

(31) Chen, X.-M.; et al. An Efficient Near-Infrared Emissive Artificial Supramolecular Light-Harvesting System for Imaging in the Golgi Apparatus. *Angew. Chem. Int. Ed.* **2020**, *59*, 10493-10497.

(32) Yu, Z.; et al. An Artificial Light-Harvesting System with Controllable Efficiency Enabled by an Annulene-Based Anisotropic Fluid. *Angew. Chem. Int. Ed.* **2022**, *61*, e202200466.

(33) Minotto, A.; et al. Efficient Near-Infrared Electroluminescence at 840 nm with "Metal-Free" Small-Molecule:Polymer Blends. *Adv. Mater.* **2018**, *30*, 1706584.

(34) Ishchenko, A. A. Photonics and molecular design of dye-doped polymers for modern light-

sensitive materials. *Pure Appl. Chem.* **2008**, *80*, 1525-1538.

(35) Kobayashi, T.; Hogan, R. Near-infrared polymer semiconductor laser. *Appl. Phys. Lett.* **2010**, *97*, 143303.

(36) Wang, X.; et al. Near-infrared lasing from small-molecule organic hemispheres. *J. Am. Chem. Soc.* **2015**, *137*, 9289-9295.

(37) Kushida, S.; et al. Low-Threshold Whispering Gallery Mode Lasing from Self-Assembled Microspheres of Single-Sort Conjugated Polymers. *Adv. Opt. Mater.* **2017**, *5*, 1700123.

(38) Goldberg, D.; Menon, V. M. Enhanced amplified spontaneous emission from colloidal quantum dots in all-dielectric monolithic microcavities. *Appl. Phys. Lett.* **2013**, *102*, 081119.

(39) Mishra, A.; et al. Cyanines during the 1990s: A Review. *Chem. Rev.* **2000**, *100*, 1973-2012.

(40) Lee, J.; et al. Fully conjugated ladder polymers. *Chem. Sci.* **2017**, *8*, 2503-2521.

(41) Lova, P.; et al. All-polymer photonic microcavities doped with perylene bisimide j-aggregates. *Adv. Opt. Mater.* **2017**, *5*, 1700523.

(42) Nevou, L. 2021.

https://github.com/LaurentNevou/Light_WaveTransmission1D_dispersion (accessed January 22, 2021).

(43) Lova, P.; et al. Polymeric Planar Microcavities Doped with a Europium Complex. *Crystals* **2020**, *10*, 287.

(44) Menon, V. M.; et al. Lasing from InGaP quantum dots in a spin-coated flexible microcavity. *Opt. Express* **2008**, *16*, 19535-19540.

(45) Manfredi, G.; et al. Directional Fluorescence Spectral Narrowing in All-Polymer Microcavities Doped with CdSe/CdS Dot-in-rod Nanocrystals. *ACS Photonics* **2017**, *4*, 1761–1769.

(46) Pelton, M. Modified spontaneous emission in nanophotonic structures. *Nat. Photonics* **2015**, *9*, 427-435.

(47) Tanaka, K.; et al. Cavity-Induced Changes of Spontaneous Emission Lifetime in One-Dimensional Semiconductor Microcavities. *Phys. Rev. Lett.* **1995**, *74*, 3380-3383.

(48) Vredenberg, A. M.; et al. Controlled atomic spontaneous emission from Er3+ in a transparent Si/SiO$_2$ microcavity. *Phys. Rev. Lett.* **1993**, *71*, 517-520.

(49) Skorobogatiy, M.; Yang, J. *Fundamentals of Photonic Crystal Guiding*; Cambridge University Press, 2008.

(50) Canazza, G.; et al. Lasing from all-polymer microcavities. *Laser Phys. Lett.* **2014**, *11*, 035804.

(51) Tavella, C.; et al. 2,5-Diisopropenylthiophene by Suzuki–Miyaura cross-coupling reaction and its exploitation in inverse vulcanization: a case study. *RSC Adv.* **2022**, *12*, 8924-8935.

(52) Kleine, T. S.; et al. One Dimensional Photonic Crystals Using Ultrahigh Refractive Index Chalcogenide Hybrid Inorganic/Organic Polymers. *ACS Macro Lett.* **2018**, *7*, 875-880.

(53) de Mello, J. C.; et al. An improved experimental determination of external photoluminescence quantum efficiency. *Adv. Mater.* **1997**, *9*, 230-232.

Chapter 7: Conclusion and Outlook

In this thesis, I have put forward the work performed for the purpose of developing new polymer-based photonic structures, including multilayered films, DBRs and optical microcavities.

Vapor sensing as a possible application for polymer multilayers was addressed in Chapters 2, 3 and 4. While I investigated general guidelines for the design of swelling-based optical-readout sensors, there is still a great prospect for the development for this typology of sensors. For example, I have shown that a sensor designed to include multiple functional groups can have a specific response correlated to strong analyte interactions. While visual readout is possible, for structurally similar analytes the use of spectrophotometers is essential for resolving the various responses, and then achieving label-free molecular recognition. Hence, advancements in the integration of optical measurements with software-assisted or device-assisted readout gives a more versatile and portable usability.[1, 2] Furthermore, this category of sensors can adopt the multivariate analysis developed for colorimetric and fluorometric sensor arrays.[2] As such, the combination of reflection maxima shifts, intensities' changes, and their kinetics, and probably fluorescence decay can be more accurately associated with specific compounds or mixtures.

On the other hand, sensors meant for direct interpretation by untrained personnel need to be straightforward to use. Hence, the response of the sensor should be specific, selective and unambiguous. One example of this is applications for smart packaging, where a sensor integrated in plastic packaging can indicate if food is fit for consumption. Following the more fundamental understanding of the phenomena explored in this thesis, a project for alimentary sensors was launched. Using the guidelines set in Chapter 2 and building on the concepts of polymer-analyte interactions in Chapters 3 and 4, amine-sensitive structures for food packaging were developed. When meats in a closed package start decomposing, various biogenic amines are released.[3] The structures, composed of poly(*N*-vinylcarbazole) and poly(acrylic acid) are sensitive to amines, thanks to the interaction between the latter and amines, leading to its significant swelling on exposure. However, the reversible action allows the tampering or false reading of the food packaging. As established in Chapters 3 and 4, the strength of interaction between the polymer and the analyte is of paramount importance for the design of the sensor. Hence, functionalizing one of the polymer components to react specifically with an analyte

would give a binding reaction that creates strong and irreversible optical response. As expected, that is indeed the result when functionalizing polyacrylic acid to react with isopropylamine as a prototype analyte giving a specific and permanent readout as seen in Fig. 7.1.
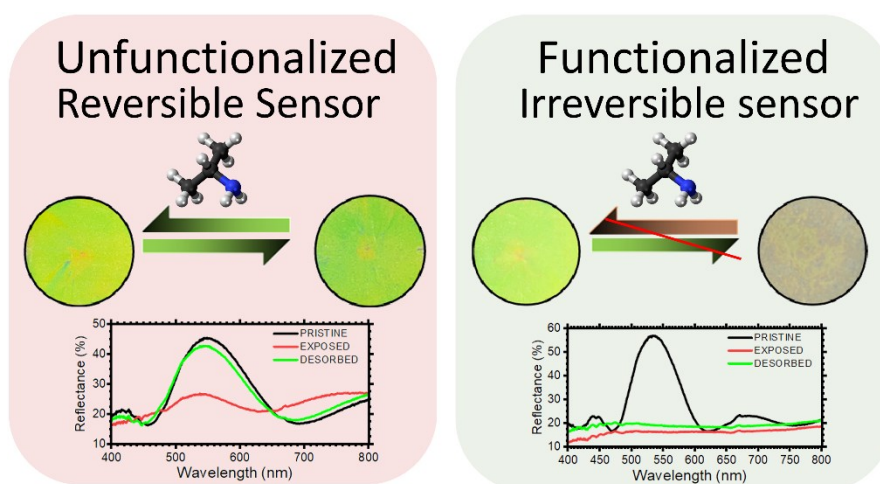

Figure 7.1. Concept for irreversible sensor for amine detection in food packaging.

In addition, the developments in fluorescent sensors, DBR sensors and microcavities independently reached give rise to the possibility of developing sensing structures combining all three elements. These structures would combine fluorescence readout from the fluorescent sensors, the enhancement in microcavities as well as the added selectivity from the polymers in the DBRs.

In Chapters 5 and 6, I continued the discourse about the effect of external factors on the fluorescence properties of fluorophores. In this case, beyond chemical environments the objective was to modify the radiative decay rate by inserting the fluorophore in a suitable engineered nanostructure, also based on DBRs. Thus, I reported the observation of the Purcell effect and alteration in the radiative lifetime in all-polymer microcavities. This effect was observed for the first time in all-polymer planar microcavities due to the high refractive index contrast between the polymers utilized for fabricating the structures. Further developments of solution-processable high-index polymers such as hyperbranched polymers, highly conjugated polymers or ones containing atoms of high molar refraction, is of utmost importance.[4] Highly porous low-index polymers or perfluorinated polymers with low polarizability will also be advantageous for such structures.[5] In addition, leveraging the high-index of some inorganic

compounds can be done for solution-processed hybrid structures using sol-gel processes. Simple sol-gel reactions between metal alkoxides and polyacrylic acid matrices, lead to stable polymer-inorganic hybrid materials that can be spin-coated. Low processing temperatures allow the alternation between inorganic and polymer films without causing the degradation of the latter.[6] Figure 7.2 shows a schematic of the sol-gel process, starting with a sol of metal-alkoxide precursor and polyacrylic acid in an acid-catalyzed hydrolyzation in butanol (Fig. 7.2a). Then upon spin-coating of the sol, a xerogel is formed through condensation reactions (panels b and c). After thermal annealing, hybrid PAA/metal oxide films are formed. Alteration between titania-PAA films as a high-index materials and polymers provide an alleviated refractive index contrast that can be impactful in the field.[4, 7]
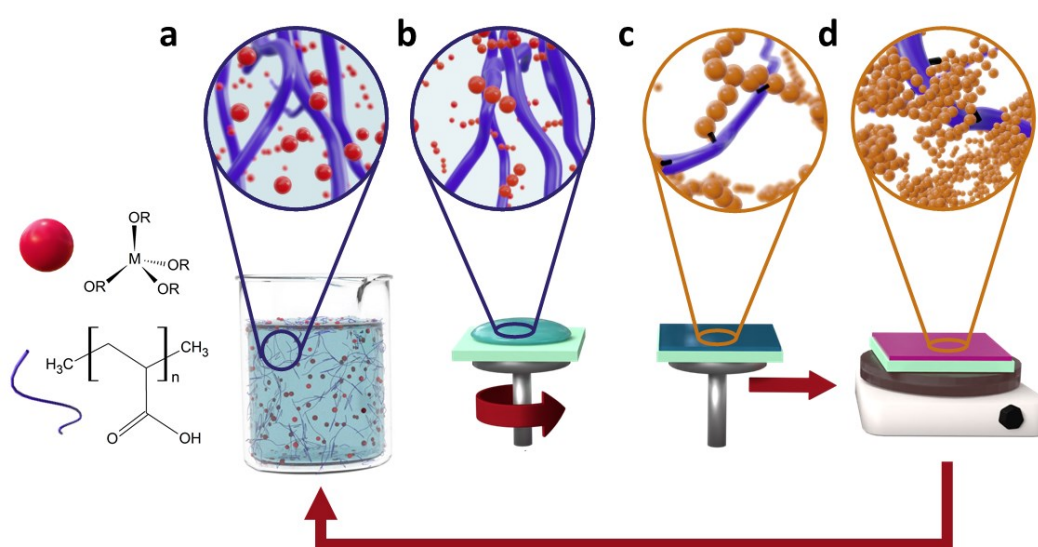

Figure 7.2. Schematic of the low-temperature sol-gel deposition process developed for the Ti-Hy thin films and multi-layered structures including a) formation of sol; b) deposition via dynamic spin-coating; c) formation and drying of film; and d) thermal annealing of the hybrid structure. [adapted from 6].

Besides the needed expansion concerning the materials used for fabricating dielectric mirrors in microcavities, the active materials are also of utmost importance. As demonstrated in this work, organic fluorophores are effective due to their easy blending with polymer matrices, high exciton binding energies and high oscillator strengths.[8] Nonetheless, they usually have a broad emission spectrum which can be detrimental to the control of the microcavity effects. Seeing that the enhancement of the density of states occurs at the cavity mode, the spectral width of the cavity mode needs to be wider than that of the fluorophore fluorescence to maximize

confinement. Multiple narrow-emitters such as quantum dots,[9] perovskites[10] and organic aggregates[11] have been increasingly studied in the last decades. Hence, embedding them in flexible light-confining structures is a compelling future research direction.

Finally, while planar microcavities have the scalability that makes them suitable for implementation for large-scale devices easily, the extent of their confinement is limited to one dimension. In fact, for highly confining inorganic microcavities, the extent of radiative lifetime change is capped at around 30%.[12] On the other hand, micro and nanopatterning of planar structures is one of the most common strategies for increasing the confinement effects in inorganic planar microcavities.[13, 14] Etching micropillars of different configurations has been widely studied, as the dielectric contrast between the high-index inorganic materials and the surrounding air leads to reflection at the lateral interface, and thus three-dimensional confinement. Figure 7.3 schematizes some micropillar designs and geometries reported in literature to further improve confinement.[7] Purcell factors larger than 30 can be reached for micropillars of diameters between 2-5 mm[15] which is an order of magnitude larger than for un-patterned planar structures.[12]
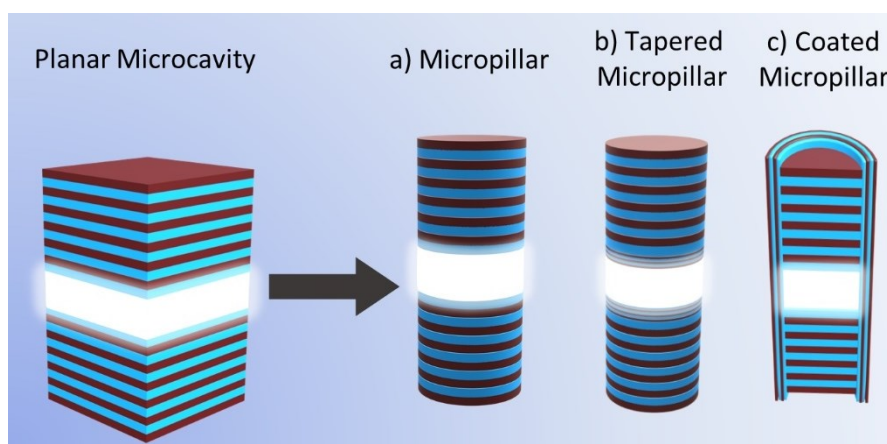

Figure 7.3. Different micropillar configurations: a) Simple micropillar, b) Tapered micropillar,[16] c) Coated micropillar.[17]

Introducing smoother transitions between the DBRs and the cavity layer through insertion of additional DBR structures of smaller periodicities[18, 19] can increase the quality factor of the structure.[16, 20] Needless to say, while reflectance of DBRs is commonly larger than 99%, the reflectance of the etched cavity sidewall is much smaller and approaches, for instance, 31% for GaAs-based micropillars, and much lower values for materials with lower dielectric contrast with air, including polymers.[17] However, coating the pillars with metals, or even radial DBRs

increases the reflectivity and confinement.[21] All these design choices can be translated to all-polymer MC for increased performance in the future.

In conclusion, the results reported inspire future developments in the field of polymer planar photonic crystals as they provide interesting and potentially scalable solutions for different technological problems such as disposable sensors, efficient light sources, and photovoltaic devices.

References

(1) Khanal, B.; et al. Machine-Learning-Assisted Analysis of Colorimetric Assays on Paper Analytical Devices. *ACS Omega* **2021**, *6*, 33837-33845.

(2) Askim, J. R.; et al. Optical sensor arrays for chemical sensing: the optoelectronic nose. *Chem. Soc. Rev.* **2013**, *42*, 8649-8682.

(3) Vinci, G.; Antonelli, M. L. Biogenic amines: quality index of freshness in red and white meat. *Food Control* **2002**, *13*, 519-524.

(4) Lova, P.; et al. Strategies for dielectric contrast enhancement in 1D planar polymeric photonic crystals. *Appl. Sci.* **2020**, *10*, 4122.

(5) Groh, W.; Zimmermann, A. What is the lowest refractive index of an organic polymer? *Macromolecules* **1991**, *24*, 6660-6663.

(6) Bertucci, S.; et al. Mild Sol–Gel Conditions and High Dielectric Contrast: A Facile Processing toward Large-Scale Hybrid Photonic Crystals for Sensing and Photocatalysis. *ACS Appl. Mater. Interfaces* **2022**.

(7) Megahd, H.; et al. Planar microcavities: Materials and processing for light control. *Opt. Mater.: X* **2022**, *13*, 100130.

(8) Hertzog, M.; et al. Strong light–matter interactions: a new direction within chemistry. *Chem. Soc. Rev.* **2019**, *48*, 937-961.

(9) Yuan, F.; et al. Engineering triangular carbon quantum dots with unprecedented narrow bandwidth emission for multicolored LEDs. *Nat. Commun.* **2018**, *9*, 2249.

(10) Smith, M. D.; et al. Tuning the Luminescence of Layered Halide Perovskites. *Chem. Rev.* **2019**, *119*, 3104-3139.

(11) Bricks, J. L.; et al. Fluorescent J-aggregates of cyanine dyes: basic research and applications review. *Methods Appl. Fluoresc.* **2018**, *6*, 012001.

(12) Tanaka, K.; et al. Cavity-Induced Changes of Spontaneous Emission Lifetime in One-

Dimensional Semiconductor Microcavities. *Phys. Rev. Lett.* **1995**, *74*, 3380-3383.

(13) Gerard, J.; Gayral, B. Strong Purcell effect for InAs quantum boxes in three-dimensional solid-state microcavities. *J. Lightwave Technol.* **1999**, *17*, 2089-2095.

(14) Rivera, T.; et al. Optical losses in plasma-etched AlGaAs microresonators using reflection spectroscopy. *Appl. Phys. Lett.* **1999**, *74*, 911-913.

(15) Barnes, W. L.; et al. Solid-state single photon sources: light collection strategies. *Eur. Phys. J. D* **2002**, *18*, 197-210.

(16) Zhang, Y.; Lončar, M. Submicrometer diameter micropillar cavities with high quality factor and ultrasmall mode volume. *Opt. Lett.* **2009**, *34*, 902-904.

(17) Jakubczyk, T.; et al. Inhibition and Enhancement of the Spontaneous Emission of Quantum Dots in Micropillar Cavities with Radial-Distributed Bragg Reflectors. *ACS Nano* **2014**, *8*, 9970-9978.

(18) Song, H.-Z.; et al. Micropillar Cavity Design for 1.55-μm Quantum-Dot Single-Photon Sources. *J. Electron. Sci. Technol.* **2019**, *17*, 221-230.

(19) Song, H.-Z.; et al. High quality-factor Si/SiO2-InP hybrid micropillar cavities with submicrometer diameter for 1.55-μm telecommunication band. *Opt. Express* **2015**, *23*, 16264-16272.

(20) Lermer, M.; et al. Bloch-Wave Engineering of Quantum Dot Micropillars for Cavity Quantum Electrodynamics Experiments. *Phys. Rev. Lett.* **2012**, *108*, 057402.

(21) Bayer, M.; et al. Inhibition and Enhancement of the Spontaneous Emission of Quantum Dots in Structured Microresonators. *Phys. Rev. Lett.* **2001**, *86*, 3168-3171

Appendix A: List of Publications

1. <u>Megahd, H.</u>; Villarreal Brito, M.; Lanfranchi, A.; Stagnaro, P.; Lova, P.; Comoretto, D. Control of Near-infrared Dye Fluorescence Lifetime in All-Polymer Microcavities, *Materials Chemistry Frontiers* **2022**, *6*, 2413–2421.

2. <u>Megahd, H.</u>; Lova, P.; Sardar, S.; D'Andrea, C.; Lanfranchi, A.; Koszarna, B.; Patrini, M.; Gryko, D.; Comoretto, D. All-Polymer Microcavities for the Fluorescence Radiative Rate Modification of a Diketopyrrolopyrrole Derivative, *ACS Omega* **2022**, *7*, 15499–15506.

3. <u>Megahd, H.</u>; Comoretto, D.; Lova, P. Planar microcavities: Materials and processing for light control, *Optical Materials: X* **2022**, *13*, 100130.

4. <u>Megahd, H.</u>; Oldani, C.; Radice, S.; Lanfranchi, A.; Patrini, M.; Lova, P.; Comoretto, D. Aquivion-Poly(*N*-vinylcarbazole) Holistic Flory-Huggins Photonic Vapor Sensors, *Advanced Optical Materials* **2021**, *9*, 2002006.

5. <u>Megahd, H.</u>; Lova, P.; Comoretto, D. Universal Design Rules for Flory–Huggins Polymer Photonic Vapor Sensors, *Advanced Functional Materials* **2021**, *31*, 2009626.

Complementary to this thesis

1. Bertucci, S.; <u>Megahd, H.</u>; Dodero, A.; Fiorito, S.; Di Stasio, F.; Patrini, M.; Comoretto, D.; Lova, P. Mild Sol–Gel Conditions and High Dielectric Contrast: A Facile Processing toward Large-Scale Hybrid Photonic Crystals for Sensing and Photocatalysis, *ACS Applied Materials & Interfaces* **2022**, *14*, 19806–19817.

2. Lanfranchi, A.; <u>Megahd, H.</u>; Lova, P.; Comoretto, D. Multilayer Polymer Photonic Aegises Against Near-Infrared Solar Irradiation Heating, *ACS Applied Materials & Interfaces* **2022**, *14*, 14550-14560.

3. Lova, P.; <u>Megahd, H.</u>; Stagnaro, P.; Alloisio, M.; Patrini, M.; Comoretto, D. Strategies for dielectric contrast enhancement in 1D planar polymeric photonic crystals, *Applied Science* **2020**, *10*, 12, 4122.

4. Lova, P.; <u>Megahd, H.</u>; Comoretto, D. Thin polymer films: simple optical determination of molecular diffusion coefficients, *ACS Applied Polymer Materials* **2020**, *2*, 563-568.

In Preparation

1. Megahd, H.; Lova, P.; Pucci, A.; Comoretto, D. Fluorescent Multi-layered Films for Label-Free Detection of Volatile Organic Compounds.

2. Escher, E.; Megahd, H.; Tavella, C.; Comoretto, D.; Lova, P. Controlling the reversibility of polymer colorimetric sensors for smart packaging.

3. Escher, E.; Martorelli, F.; Magnasco, L.; Poggi, A.; Comoretto, D.; Lova, P. The recovery of waste cigarette butts and plastic packaging waste for photonic applications.

Appendix B: Communications

Personal Conference Communications

1. Megahd, H.; Lova, P.; Comoretto, D. Polymer Photonic Crystal Chemical Sensors, *Convegno Nazionale Dell'Associazione Italiana di Scienza e Tecnologia Delle Macromolecole* **2022,** Trento, IT (Oral)

2. Megahd, H.; Slimani, S.; Peddis, D; Lova, P.; Comoretto D. Magnetic Nanocomposite Polymer Photonics, *European Polymer Congress* **2022**, Prague, CZ (Oral)

3. Megahd, H.; Bertucci, S.; Comoretto, D.; Lova, P. Hybrid Polymer-Inorganic Photonic Crystal Sensors, *MACROGIOVANI Workshop for Young Researchers on Macromolecular Science* **2021**, Genova, IT (Oral)

4. Megahd, H.; Lova, P.; Pucci A.; Comoretto D. Fluorescent Multi-layered Films for Label-Free Detection of Volatile Organic Compounds*, META* **2021**, Online (Oral)

5. Megahd, H.; Lova, P.; Comoretto D. All-Polymer Microcavities for Photoluminescence Control, *Nanolito Summer School* **2021**, Salamanca, ES (Poster)

6. Megahd, H.; Lova, P.; Comoretto D. Commodity Polymers as Sensors, *EPF Summer School* **2021**, Online (Poster)

7. Megahd, H.; Lova, P.; Pucci, A.; Comoretto, D. Polymer Fluorescent Films for Label-Free Detection of Organic Vapors, *ACS Spring Meeting, Macromolecular Chemistry: The Second Century* **2021**, Online (Oral)

8. Megahd, H.; Lova,P.; Comoretto, D. Fluorescent Multi-layered Films for Label-Free Detection of Volatile Organic Compounds. *Macrogiovani - Digital Edition* **2020**, Online (Oral, Best Presentation Award)

9. Meghad, H.; Lova, P.; Comoretto, D. Optical Sensing and Determination of Molecular Diffusion Coefficient in Polymer Multilayered Photonic Crystals, *International Workshop on Polymeric Materials* **2019**, Setif, DZ (Oral)

Other Communications

1. Bertucci, S; <u>Megahd, H.</u>; Dodero, A.; Fiorito, S.; Patrini, M.; Di Stasio, F.; Comoretto, D.; Lova, P. Solution Processed Inorganic Oxides: High Performing Hybrid Materials for Photonics, *NanoGe Spring Meeting* **2022**, online conference, March 7-11, 2022. (by Simone Bertucci)

2. Magnasco, M.; <u>Megahd, H.</u>; Escher, A.; Lanfranchi, A.; Lova, P.; Comoretto, D. Polymeric Planar Microcavities for Sensing, *EUPOC* **2022** Bertinoro, IT (by Laura Magnasco)

3. Lanfranchi, A.; <u>Megahd, H.</u>; Lova, P.; Comoretto, D. All-Polymer Photonic Aegises for Thermal Management, *European Polymer Conference on "Block Copolymers: Building Blocks for Nanotechnology* **2022**, Bertinoro, IT (by Andrea Lanfranchi)

4. Lanfranchi, A.; <u>Megahd, H.</u>; Lova, P.; Comoretto, D. Multilayer Polymer Photonic Aegises for Thermal Shielding, *Macrogiovani* **2022**, Florence, IT (by Andrea Lanfranchi)

5. <u>Megahd, H.</u>; Lova, P.; Sardar, S.; D'Andrea, C.; Lanfranchi, A.; Koszarna, B.; Patrini, M.; Gryko, D.; Comoretto, D. Towards efficient and sustainable light sources: radiative rate engineering by polymer planar microcavities, *European Polymer Congress* **2022**, Prague, CZ (by Davide Comoretto)

6. Bertucci, S; <u>Megahd, H.</u>; Dodero, A.; Fiorito, S.; Patrini, M.; Di Stasio, F.; Comoretto, D.; Lova, P. High dielectric contrast hybrid polymer-inorganic planar photonic crystals, *European Polymer Congress* **2022**, Prague, CZ (by Paola Lova)

7. Lanfranchi, A.; <u>Megahd, H.</u>; Lova, P.; Comoretto, D. Polymer Photonic Crystals for Passive Thermal Management, *European Polymer Congress* **2022**, Prague, CZ (by Andrea Lanfranchi)

8. Bertucci, S.; <u>Megahd, H.</u>; Dodero, A.; Fiorito, S.; Di Stasio, F.; Patrini, M.; Comoretto, D.; Lova, P.; Solution processed inorganic semiconductors: high performing hybrid materials for photonics, *ICOOPMA-EuroDIM* **2022**, Ghent, BE (by Simone Bertucci)

9. Lanfranchi, A.; <u>Megahd, H.</u>; Lova, P.; Comoretto, D. All-Polymer Multilayer Photonic Aegises Against Near-Infrared Irradiation Heating, *XIV Convegno*

Nazionale dell'Associazione Italiana di Scienza e Tecnologia Delle Macromolecole **2022**, Trento, IT (by Andrea Lanfranchi)

10. Bertucci, S.; Escher, A.; <u>Megahd, H.</u>; Peragallo, M.; Patrini; M.; Comoretto, D.; Lova**,** P. Porous hybrid polymer-inorganic photonic crystals for sensing and photocatalysis, *XIV Convegno Nazionale dell'Associazione Italiana di Scienza e Tecnologia Delle Macromolecole* **2022**, Trento, IT (by Paola Lova)

In the News

- "Egide fotoniche", Unige.life, 20-4-2022 (https://life.unige.it/egide-fotoniche)
- "Università di Genova: il gruppo di ricerca Rely-photonics fa un ulteriore passo avanti nello sviluppo di sensori colorimetrici per il monitoraggio ambientale", La Voce di Genova, 20-4-2021 (https://www.lavocedigenova.it/2021/04/02/leggi-notizia/argomenti/attualita-4/articolo/universita-di-genova-il-gruppo-di-ricerca-rely-photonics-fa-un-ulteriore-passo-avanti-nello-svilup.html)
- "Inquinamento: da Unige nuovi sensori per il monitoraggio ambientale che si ispirano alle farfalle", Genova Today, 2-4-2021 (https://www.genovatoday.it/attualita/universita-genova-sensori-farfalle.html)
- "L'Università di Genova ha sviluppato sensori sensibilissimi all'inquinamento", Liguria Notizie, 2-4-2021 (https://liguria.bizjournal.it/2021/04/luniversita-di-genova-ha-sviluppato-sensori-sensibilissimi-allinquinamento/)
- "UniGe, passo avanti nello sviluppo di sensori colorimetrici", Liguria Notizie, 2-4-2021 (https://www.ligurianotizie.it/unige-passo-avanti-nello-sviluppo-di-sensori-colorimetrici/2021/04/02/436022/)
- "Si ispirano alle farfalle i sensori per scovare gli inquinanti", Unige.life, 30-3-2021 (https://life.unige.it/sensori-monitoraggio-ambientale).
- "Cibo ancora fresco? La risposta dalla pellicola "parlante" ideate dal Dipartimento di Chimica e Chimica industrial dell'Università di Genova", La voce di Genova, 4-2-2020 (https://www.lavocedigenova.it/2020/02/04/leggi-notizia/argomenti/innovazione/articolo/cibo-ancora-fresco-la-risposta-dalla-pellicola-parlante-ideata-dal-dipartimento-di-chimica-dellu.html).
- "Inventata la pellicola magica per alimenti. Cambia colore rivelando freschezza e

qualità", Il Secolo XIX, 31-1-2020

(https://chimica.unige.it/sites/chimica.unige.it/files/pagine/Il%20Secolo%20XIX_31-01-2020.pdf).